AN ALBEDO MAP AND FROST MODEL OF PLUTO

by
Eliot Fisher Young
A.B., Amherst College (1984)
S.M., Massachusetts Institute of Technology (1987)
S.M., Massachusetts Institute of Technology, (1990)

SUBMITTED IN PARTIAL FULFILLMENT
OF THE REQUIREMENTS FOR THE DEGREE OF

DOCTOR OF PHILOSOPHY
IN EARTH, ATMOSPHERIC AND PLANETARY SCIENCES

at the

MASSACHUSETTS INSTITUTE OF TECHNOLOGY
September 1992

Signature of the Author _____
Department of Earth, Atmospheric and Planetary Sciences
September 16, 1992

Certified by _____
Professor Richard P. Binzel
Thesis Supervisor
Atmospheric and Planetary Sciences

Accepted by _____
Professor Thomas Jordan
Chairman, Department Graduate Committee

Acknowledgments

This thesis has been a collaborative effort. My committee members brought their various backgrounds to bear on the problems of mapping Pluto and modeling volatile transport from its surface, and I asked them a lot of questions.

I want to thank Jim Elliot for a careful reading of my thesis, Tim Dowling for suggesting a spherical harmonic map in the first place, and Alan Stern for an intensive tutorial on icy satellites. I am particularly grateful to Rick Binzel for sharing his mutual event data set in the first place. I cannot list all of the things I've learned from my committee, but they will recognize the discussions we've had in these pages.

Other unwitting collaborators:

- John Spencer explained his Triton model to me.
- Marc Buie discussed his mapping procedure.
- Andy Ingersoll explained Io's supersonic winds.
- Dale Cruikshank explained the spectral features showing N_2 and CO on Pluto.
- After several discussions, Tony Dobrovolskis finally convinced me that the mutual event season happening at perihelion is a coincidence.

I owe the largest debt to my sister, Leslie Young. Nearly every idea in here has benefited from her input. I also learned linear and nonlinear least squares fitting from her, the bread and butter of this thesis. Her atmospheric modeling [Elliot and L. Young, 1992] based on the 1988 stellar occultation by Pluto is crucial to the volatile transport model of Chapters IV and V.

I am glad that my fiancée is a former editor. Thank you, Diane.

Thanks, Mom and Dad.

Table of Contents

An Albedo Map and Frost Model of Pluto
by
Eliot Fisher Young
Submitted in partial fulfillment of the requirements for the Degree of
Doctor of Philosophy in Earth, Atmospheric and Planetary Science
at the Massachusetts Institute of Technology, May 1992.

Thesis Supervisor: Dr. Richard P. Binzel, Associate Professor of Planetary Science.

Abstract

The once-per-century set of occultations of Pluto by its satellite Charon enable the construction of an albedo map of Pluto's sub-Charon hemisphere, which in turn provides a basis for models of volatile transport on Pluto. Photometric observations of the Pluto-Charon mutual events were obtained at the University of Texas McDonald Observatory from 1985 through 1990. We use three least squares models to find the surface albedo distributions that best match the observed lightcurves. All of the least squares fits use a singular value decomposition (SVD) implementation. The three models produce similar albedo maps.

Features of the maps include a large, very bright region over the south pole, a dark band over the mid-southern latitudes, a bright band over the mid-northern latitudes. The average normal reflectance of the higher northern latitudes is about the same as Pluto's global average of 0.5. We do not find compelling evidence of a bright cap over the north polar region.

We model Pluto's atmosphere and albedo for the period from 1990 to 2040. Pluto's surface temperature drops by about six degrees during this period, resulting in over 97% of its current atmosphere condensing onto the surface. As Pluto's atmosphere thins, the winds arising from sublimation-driven pressure gradients increase beyond Mach 1. Our model predicts that the crossover to supersonic winds occurs around 2070. Our current frost migration model is valid only for the subsonic regime, but a supersonic frost transport model may help to explain the polar asymmetry of Pluto's albedo distribution. In the short term, the bulk of the new frost is deposited on the south pole. The change in albedo distribution is sensitive to the manner in which new frost reflectances are modeled, but the sheer volume of material (over 40 g/cm^2) deposited mandates the formation a bright cap on the south pole. The north pole may develop a smaller polar cap during this period.

I. Introduction

Pluto is the only major planet that has yet to be visited by spacecraft. Our knowledge of other planets is sufficient to place them in the provinces of geophysicists and atmospheric dynamicists, whereas Pluto's radius and mass were only recently determined to better than a factor of two. This situation should change soon. A recently completed set of transits and occultations between Pluto and its satellite Charon promises to make the next few years a golden age for the study of Pluto. This thesis uses lightcurves from these occultations to build a surface reflectance map of Pluto and makes 50 year projections for Pluto's surface temperature, pressure, albedo and column abundance.

A. The Pluto-Charon System

When Charon was discovered in 1978 [Christy and Harrington, 1978], its orbital plane around Pluto was nearly parallel to the line of sight from the Earth. Pluto's rotation rate had been known since 1954 from the periodicity of rotation lightcurves [Walker and Hardie, 1954]. While looking at astrometry plates, James Christy noticed an irregularity on Pluto [Figure 1] that moved with a period of 6.38 days, the same as Pluto's rotation period. The "bump" might have been a bright spot on Pluto's surface or a satellite. In early 1985 the first transits were observed [Binzel et al., 1985], as Charon grazed across Pluto's north polar region. During the next six years a transit of Pluto by Charon and an occultation of Charon by Pluto (collectively referred to as "mutual events") occurred nearly every Pluto day, equivalent to 6.38 Earth days. As shown in Figure 2, the path of Charon's transits migrated from Pluto's northern hemisphere to its southern one over this six year period . (We define "north" as the direction of Pluto's spin angular momentum vector.) We obtained mutual events lightcurves spanning this entire period. These provide coverage of the entire Charon-facing hemisphere of Pluto. Since Pluto's and Charon's orbits are mutually synchronous, Charon's transits always cover the same hemisphere of Pluto, which we refer to as "Pluto's sub-Charon hemisphere."

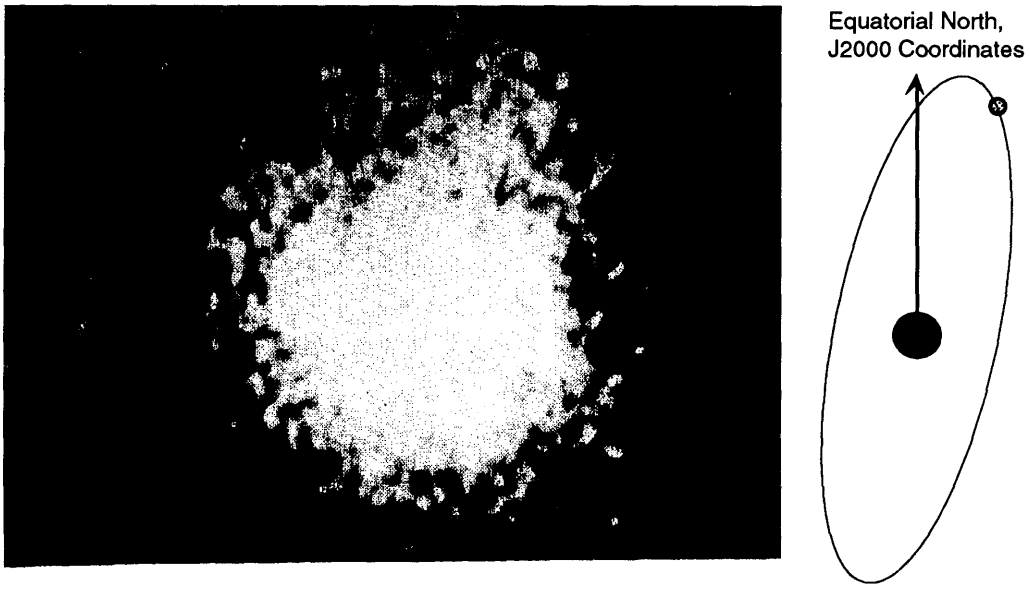

Figure 1. Photographic plate of Pluto and Charon circa 1978. This is one of the plates which led to the discovery of Charon by James Christy of the United States Naval Observatory (USNO). On the right side is a schematic of the system's orientation. Adapted from "The New Solar System," [Beatty and Chaikin, 1990].

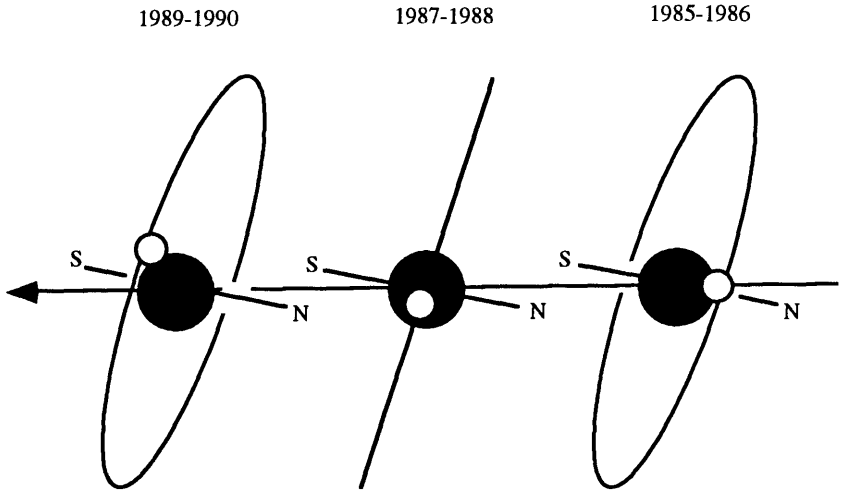

Figure 2. Charon's path across Pluto migrates from north to south over the six year period of the mutual events.

The angular separation between Pluto and Charon is only 0.9 arcseconds when Charon is at elongation. The pair can be resolved by a few exceptional groundbased systems or by the Hubble Space Telescope (HST). The currently accepted value for the

Pluto-Charon separation is 19640 ± 320 km, from speckle interferometry [Beletic et al, 1989]. Tholen and Buie [1989] have used the timing of the mutual events to complete a nonlinear least squares fit for Charon's orbital elements and Pluto's and Charon's diameters, using Beletic's semimajor axis to scale the linear dimensions.

Table 1. Orbital and physical parameters for Charon and Pluto [Tholen and Buie, 1989].

Semimajor axis	19,640	±	320	km
Eccentricity	0.00009	±	0.00038	
Inclination	98.3	±	1.3	deg
Ascending node[a]	222.37	±	0.07	deg
Argument of periapses[a]	290	±	180	deg
Mean Anomaly[b]	259.90	±	0.15	deg
Epoch	JD 2,446,600.5	=	1986, June 19	
Period	6.387230	±	0.000021	days
Pluto radius	1142	±	9	km
Charon radius	596	±	17	km

[a] Referred to the mean equator and equinox of 1950.0.
[b] Measured from the ascending node.

Tholen and Buie have upgraded some of Charon's orbital elements in this table since the work on our maps was completed. In particular, the inclination was increased to 98.8°, and Pluto's and Charon's radii were changed to 1150 ± 7 and 593 ± 10 km respectively. Bear in mind that the quoted error for Pluto's radius, "1150 ± 7 km," is *only* the internal error generated from the least squares fit. The mutual event determination of both Pluto's and Charon's radii are scaled by Charon's semimajor axis, which to this date remains the most uncertain of Charon's orbital parameters. These changes in the inclination and the radii are minor compared to the discrepancy between the planetary radii of Tholen and Buie and the radii based on the 1988 stellar occultation [Elliot et al. 1989]. The stellar occultation estimates for Pluto's radius are generally *50 km larger* than the mutual event estimates. Part of the discrepancy arises from the question of whether the mutual events' first and last contacts refer to the solid surface of Pluto or to an optically thick layer of the atmosphere. Recent HST imaging of the Pluto-Charon separation, which seems to indicate a semimajor axis *smaller* than 19640 km, are also in conflict with the occultation results [Tholen and Buie, 1991]. Another possible source for the radii discrepancies is the way Pluto and Charon were modeled in the mutual events. The treatment of Tholen and Buie modeled Pluto and Charon as uniformly bright disks [Buie et al., 1992]. If Pluto and Charon are significantly limb-darkened, then the

mutual event solutions would tend to underestimate their radii. We have run nonlinear fits in which Pluto and Charon are modeled as limb-darkened disks, solving for Pluto's and Charon's radii to semimajor axis ratios (R_p/a and R_c/a) as well as a Minnaert limb parameter for both objects. This fit is based on four "superior" events (Pluto in front) and six inferior ones. Both superior and inferior events must be used in order to separate radii from the Minnaert limb coefficients. Pluto occults Charon with its entire physical radius, but may have a smaller apparent radius due to limb effects when it is transited by Charon.

We normalize all ten lightcurves by their pre-event baseline points. We ignore the possibility that the sub-event and anti-event hemispheres of Pluto and Charon have different geometric albedos, and the fact that the pre- and post-event baselines should be fit by a slope, not a constant flux. Ideally the relative B-magnitudes of Pluto and Charon would be determined from their respective rotational lightcurves, and someday they will be. In the meantime we assume that Pluto and Charon's magnitudes are constant duing both the superior and inferior events. The penalty for these assumptions is the high χ^2 per degree of freedom, which is nearly 20 (ideally it should be about one), and the large formal errors generated from the fit. Nevertheless, despite the large formal errors for R_p/a and R_c/a, the major portion of the error in the estimates of the radii are due to the uncertainty in the semimajor axis.

Table 2. Nonlinear Fit for Pluto's and Charon's Radii and Minnaert Limb Parameters - a Preliminary Solution

Pluto radius/semimajor axis	R_p/a =	0.0606 ± 0.00022
Charon radius/semimajor axis	R_c/a =	0.0327 ± 0.00019
Pluto Minnaert parameter	k_p =	0.51 ± 0.02
Charon Minnaert parameter	k_c =	0.56 ± 0.02
Chi Square/degree of freedom	20	

Table 3. Covariance Matrix

R_p	R_c	k_p	k_c
2.39674×10^{-9}	1.09602×10^{-10}	1.22581×10^{-7}	9.26265×10^{-8}
1.09602×10^{-10}	1.79196×10^{-9}	-1.09742×10^{-8}	4.24156×10^{-9}
1.22581×10^{-7}	-1.09742×10^{-8}	2.44027×10^{-5}	2.25612×10^{-5}
9.26265×10^{-8}	4.24156×10^{-9}	2.25612×10^{-5}	2.25408×10^{-5}

Table 4. Normalized Covariance Matrix

R_p	R_c	k_p	k_c
1.0	0.05093	0.50309	0.39343
	1.0	-0.05891	0.01494
		1.0	0.96169
			1.0

The internal errors from the least squares fit (i.e., the diagonal elements of the covariance matrix (Table 3)) are only 1/3 to 1/4 of the error due to the uncertainty in the semimajor axis measurement. When these uncertainties are propagated into the radii estimates, we get (recall that a = 19640 ± 320 km [Beletic et al., 1988]):

$\sigma^2(R_p) = (19640 \times 0.00022)^2 + (0.0607 \times 320)^2 = (4.32)^2$ km + $(19.42)^2$ km = $(19.9)^2$ km

and

$\sigma^2(R_c) = (19640 \times 0.00019)^2 + (0.0327 \times 320)^2 = (3.73)^2$ km + $(10.46)^2$ km = $(11.1)^2$ km.

So R_p = 1190.7 ± 19.9 km and R_c = 642.2 ± 11.1 km.

The value of 1190 ± 20 km is consistent with the extrapolated estimates for Pluto's radius based on the 1988 stellar occultation [e.g. 1206 ± 11 km, [Elliot and L.Young, 1992]), and the value of 642 ± 11 km, while larger than any previous estimates, is consistent with the lower limit of 601.5 km associated with the Charon occultation recorded by Walker [Elliot and L.Young, 1991]. The limb parameters are not highly correlated with the radii to semimajor axis ratios, but are highly correlated with each other. The limb parameters are close to 0.5, indicating no limb effect for Pluto and only slight limb darkening for Charon. It is a little surprising that the Minnaert parameters turn out to be so close to the non-limb darkened (uniform disk) case, yet the radii from the fit are 40 km larger than those of Tholen and Buie given a semimajor axis of 19640 km. The difference between our radii and those of Tholen and Buie seem to be data, not model driven. Until we resolve the differences between the two data sets, we will stick with the parameters of Tholen and Buie as listed in Table 1.

As a sensitivity test of the radii we generated two normal reflectance maps, shown here in a side by side comparison.

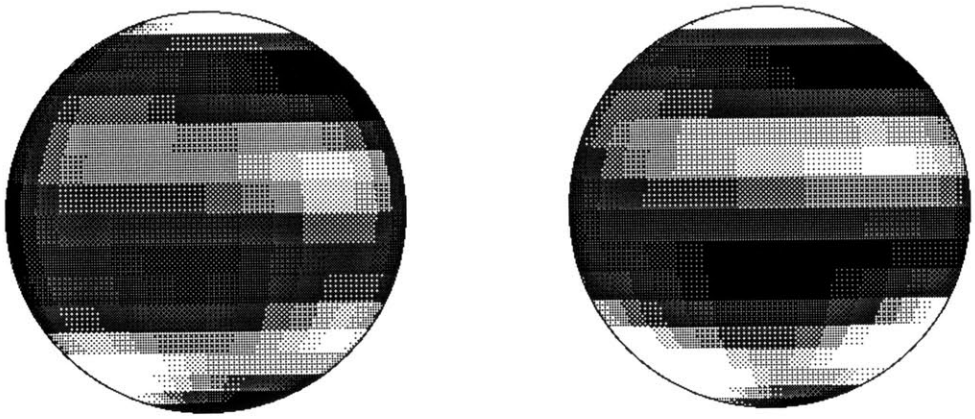

Figure 3. Side by side comparison of spherical harmonic maps generated from the usual parameters (R_p = 1142 km, R_c = 596 km) (Right) and the parameters from the preliminary nonlinear least squares model incorporating Minnaert limb darkening (left).

Both maps in Figure 3 are the results of identical inversion processes. The maps primarily show differences in the longitudinal placement of features. The map on the left also shows a dark band on the western limb, indicating that the model Pluto was uncovered when the lightcurve was in the flat baseline phase. This would require the exposed part of the western limb to be dark, since it must not be a contributor to the lightcurve.

The dark western limb makes the model based on the larger radii less plausible. Until we improve the nonlinear fit parameters, we will continue to use the mutual event parameters of Tholen and Buie [1988].

B. The Utility of the Mutual Event Lightcurves

During an occultation of Pluto by its satellite, the total brightness of the system will decrease, depending on the brightness of the regions of Pluto that are obscured by Charon and its shadow. Six mutual event lightcurves (inferior) are shown in Figure 4. These lightcurves are the data set on which the albedo maps derived here are based.

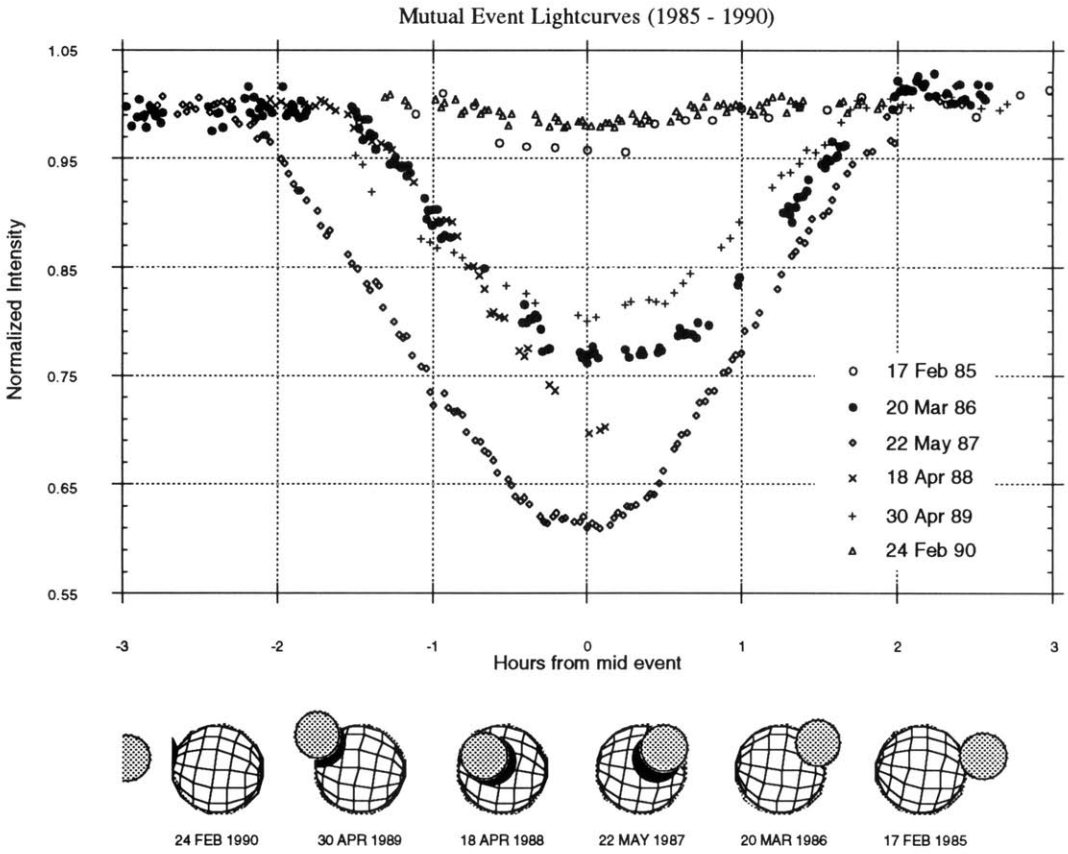

Figure 4. Six lightcurves of occultations of Pluto by Charon. These lightcurves were measured at approximately yearly intervals from 1985 through 1990. All six lightcurves are courtesy of Richard Binzel.

Figure 4 shows that a central event lasts a little over four hours from first to last contact, and the depth of the event could be as low as 60% of the baseline flux. Charon's orbital elements enable us to project Charon's position over Pluto's surface for every observation in the six lightcurve set. The decrease in brightness for that observation tells us how bright the covered region on Pluto must be. With enough observations we can piece together a mosaic of the entire sub-Charon hemisphere of Pluto. This mapping procedure is the topic of Chapters II and III.

We assume that Charon's contribution to the lightcurve is a constant for every observation. Separate lightcurve photometry of Pluto and Charon is barely possible from the HST. Resolved images of Pluto and Charon in the 2.2 micron band have yielded magnitudes for opposite hemispheres of Charon (a rather sparse lightcurve, but useful

for the mutual event geometry), but a similar analysis in the B or V bands has not been completed as of this writing [Bosh et al., 1992]. Charon rotates only 12° during an event, so roughly 2% of Charon's disk disappears off the east limb as another 2% rises over the west.

Because a Pluto's albedo is likely to be closely related to recent condensation or sublimation of frost, an albedo map of Pluto provides an opportunity to determine large scale, seasonal climatology on Pluto. Volatile transport models have already been developed for other icy satellites, notably Triton [Spencer and Moore, 1992] and Io [Ingersoll et al, 1985]. We believe that Pluto, like Triton, has a global atmosphere, the temperature and surface pressure of which are governed by the transport of volatiles over the surface. Some of the bulk atmospheric parameters can be taken from the analysis of the 1988 stellar occultation [Elliot and L.Young, 1992]. This occultation yields surface temperature, pressure and column abundances given the identification of N_2 as the primary volatile in Pluto's atmosphere [Owen et al., 1992] [Cruikshank, 1992]. The Triton model, Plutonian atmospheric predictions, and results of the volatile transport model are the subjects of Chapters IV and V.

II. The Pluto Mapping Problem

To make an albedo map of Pluto from mutual event lightcurves, one keeps track of how the Pluto-Charon system brightness changes as parts of Pluto are covered or uncovered. The change in brightness tells us the relative brightness of the covered parts. The challenge is to reconcile all of the covered parts, which generally have banana-like or semi-circular shapes, into a single reflectance map of Pluto's surface. This chapter outlines issues in the lightcurve inversion problem for the Pluto-Charon system by taking a chronological survey of work in this area. We begin with two maps that were constructed without mutual event data.

A. Rotation Lightcurves: The Two-Spot Model [Marcialis, 1988] and The SHELF Model [Buie and Tholen, 1988]

Rotation-based maps are poorly constrained in latitude. If the axis of rotation is not perpendicular to the observer's line of sight, then much of the rotating body may never come into view, and the lightcurve may show almost no variation with rotation. Even if the axis of rotation is perpendicular to the line of sight (as is currently the case with Pluto), the rotation lightcurves do not produce a unique surface map, as Wild [1989] points out. For example, the following two albedo distributions both could be solutions to the same rotation lightcurve.

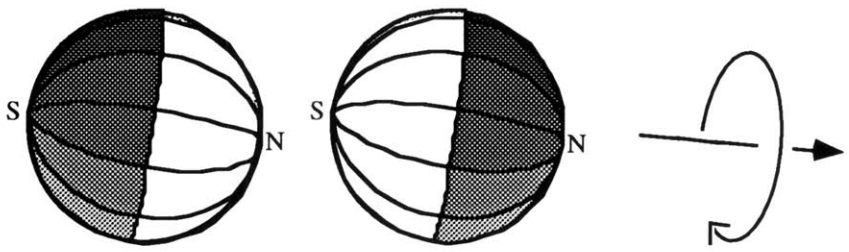

Figure 5. These two different albedo maps produce identical rotational lightcurves if viewed from a sub-equatorial point of view.

One can obtain better resolution in latitude if rotation lightcurves from different viewpoints are available. In Pluto's case, the lightcurve of Walker and Hardie [1954] provides a significantly different orientation [Figure 6].

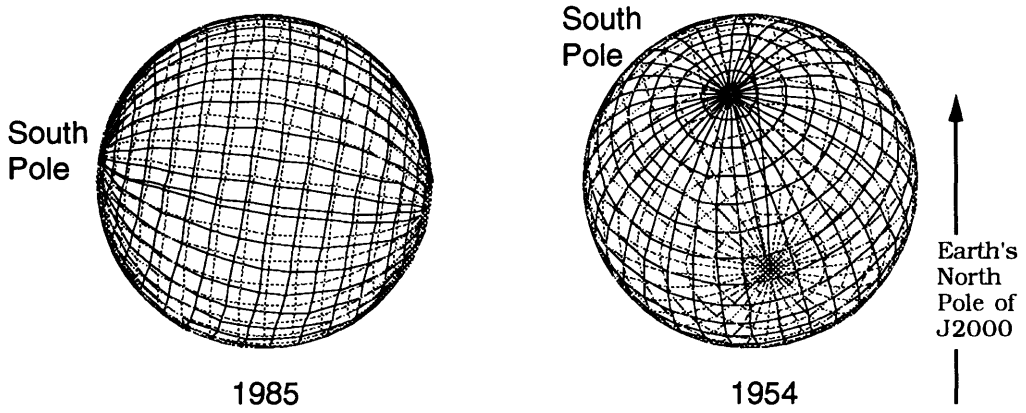

Figure 6. Pluto's orientation as viewed from the Earth in 1954 offers a more polar view than the current orientation.

If one were making a map from a 1985 and a 1954 lightcurve, one could get latitudinally resolved information about each pixel from the different pixel projections in the two cases. The "arctic circles" would still only be resolved in longitude, but the area of these regions could be reduced by including more recent (e.g., 1964) lightcurves in the data set. A latitudinally resolved albedo map *can* be determined from noise-free rotation lightcurves [Drish and Wild, 1991]. The problems arise when trying to invert noisy lightcurves. Because pixel albedos are determined from small differences in their projected contributions to Pluto's overall albedo, adjacent pixels are highly correlated, and noise between consecutive points in a lightcurve wreaks havoc on the pixel solutions. In theory one can generate maps with good resolution in latitude, but in practice these maps will have banana-shaped features running parallel to lines of longitude and non-unique solutions due to the high degree of correlation between adjacent pixels. To lessen the correlation between pixels, one needs lightcurves in which pixels are alternately completely visible (not just projected slivers) and then completely covered. The transits by Charon are the best source of this type of lightcurve.

The use of 20 and 30 year old lightcurves implicitly assumes that Pluto's albedo distribution has remained constant over that period. In Chapters IV and V we calculate resurfacing rates for most of Pluto in excess of $\pm$ 1 g/cm^2 per decade, easily enough to change Pluto's albedo. Buie et al. [1992] have noted that the contributions to his model's χ^2 from each rotation lightcurve data point is six times that of each mutual event lightcurve point.

In the Two-Spot Model the size, location, and albedo of two spots on Pluto's surface are free parameters in a least squares fit. The advantage of a spot model is that it structures the problem so that there is a chance that the free parameters can be found

from the available data set. The disadvantage is that Pluto's surface, in reality, may not have large spot-shaped features. Nevertheless, in the face of limited data, the spot model approach is a viable way to solve an underdetermined problem. The Two-Spot Model uses four parameters to describe the spots: two spot radii, a single latitude for both spot centers, and a longitude offset between the two spots. These parameters are called *R1*, *R2*, *LAT*, and *DLON* respectively. Another parameter, *ALBFAC*, defined as 1 - (spotted albedo / unspotted albedo), describes the albedo of the spots (a single parameter) relative to the background. Finally several polar cap models are tried, loosely constrained by the secular dimming and increase in rotational variation of Pluto's lightcurve since 1954. The polar caps and the two spots are determined independently from secular dimming effects and from rotational lightcurves. Marcialis' adopted model is shown in Table 5.

Table 5. Adopted parameters for the Two-Spot Model, adapted from Marcialis [1988].

R1	46	deg	*from rotational lightcurves*
R2	28	deg	
LAT	-23	deg	
DLON	-134	deg	
ALBFAC	0.9		
N. Pole Limit	59	deg	*from secular dimming*
S. Pole Limit	-69	deg	

Marcialis points out that the polar boundaries are poorly constrained in his model fit. It is important to note the large size of the north pole relative to the south. The model from Table 5 sports a north pole with approximately 175% the area of the south pole. Interestingly enough, the SHELF Model [Buie and Tholen] supports this same asymmetry, in contrast to the mutual event maps that would follow. Perhaps there was an expectation that a large frost cap would have developed on the north pole because it was in perpetual shadow during the approach to perihelion .

The SHELF Model [Buie and Tholen, 1988] is also a four spot model (the Two-Spot Model has four spots counting the poles), but has a larger number of free parameters. Each spot is assigned an independent radius, central latitude and longitude, a single scattering albedo, and an average particle phase function (evaluated at a scattering angle of 180°). The single scattering albedos and phase functions of Charon and Pluto's background constitute four more parameters, for a total of 24. The south polar spot is locked directly over the south pole, reducing the number of free parameters by 2. Pluto's

overall intensity is computed using the Hapke bidirectional reflectance equation, which is Eq. (16) from Hapke, 1981.

$$r(\mu_0, \mu, g) = \frac{w}{4\pi} \frac{\mu_0}{\mu_0 + \mu} \{[1 + B(g)]P(g) + H(\mu_0) H(\mu) - 1\} \quad (1)$$

where r = ratio of bidirectionally reflected to incident flux,

w = single scattering albedo

g = phase angle (angle between the incident ray and the ray to the observer)

μ = cos(emitted ray)

μ_0 = cos(incident ray)

P = phase function

H = approximation to Chandrasekhar's H-function, of the form

$$H(\mu) = \frac{1 + 2\mu}{1 + 2\mu\sqrt{1 - w}} \quad (2)$$

and B(g) = the backscattering function,

$$B(g) = B_0\left[1 - \frac{\tan|g|}{2h}(3 - e^{-h/\tan|g|})(1 - e^{-h/\tan|g|})\right] \quad (3)$$

where the B_0 parameter describes the opposition effect.

$$B_0 \approx e^{-w^2/2} \quad (4)$$

and h is a packing parameter.

This expression for the intensity is a nonlinear function of w and P(0). Buie and Tholen use a simplex algorithm to search for the minimum χ^2 [Press et al, 1988]. In my experience the simplex algorithm is suitable for systems with a small number (e.g., three or four) of parameters but not for larger systems, since it is very slow and often stops prematurely. Nevertheless, Buie and Tholen, starting from three different arrangements of spots on the planet's surface (called MIN, MAX, and SHELF) find two local χ^2 minima. Two of the initial spot distributions, MIN and SHELF, converged to the same solution. Although no mutual event lightcurves were included in the data set, they were used to choose qualitatively between the simplex method's two local minima. The SHELF model was judged a better fit to mutual event data than the MAX model.

Table 6. Spot Model Parameters for SHELF, adapted from Buie and Tholen [1988].

	Radius (km)	w	P(0)		
Pluto[a]	*1162.0*	0.776	2.1		
Charon[b]	*620.7*	0.863	1.		
Spot	Latitude	Longitude	Radius	w	P(0)
#1	-1.9	110.1	30.6	0.406	0.4
#2	-23.0	195.2	14.8	0.971	2.9
#3	81.4	195.6	59.4	0.999	2.2
#4	*South Pole*		44.2	1.000	1.5

[a] These are the unspotted properties of Pluto.
[b] These are the global properties of Charon.

The radii of 1162 km and 620 km are based on a semimajor axis for Charon of 19800 km. (The following paper in the same issue of *Icarus* is by Beletic et al. [1988], in which the authors (Tholen and Buie) revise the speckle value for Charon's semimajor axis to be 19640 ±320 km.) The SHELF Model is shown in Figure 7.

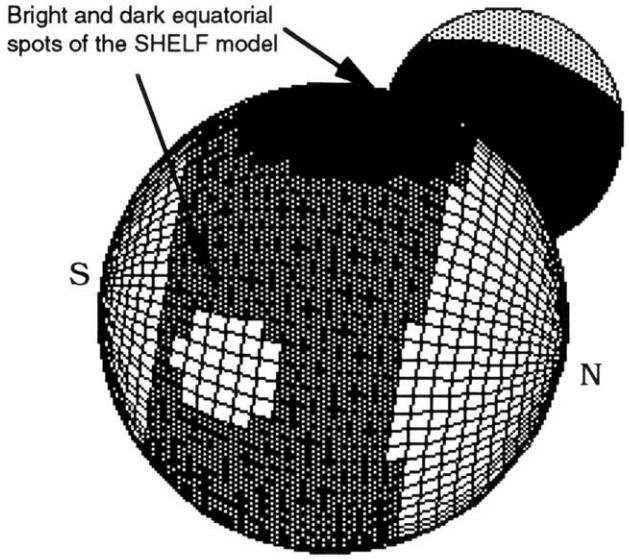

Figure 7. The SHELF model, Jan 23, 1988 (with Charon emerging from eclipse), adapted from Figure 9 from Buie and Tholen [1988]. Up in this figure is Equatorial north of J2000.

Summarizing the results of the Two-Spot Model and the SHELF Model, we find:

- The polar regions are very bright. Both models fit Pluto with polar caps that have geometric albedos of one.
- Both models find that the north polar is much larger than the south polar cap. In the next section we will see that this finding is at odds with the results of the mutual event maps.

B. Mutual Event Models:
The Eleven Panel Map [Young 1990],
The ESO Map[Burwitz et al, 1991], **and**
The Maximum Entropy Map [Buie et al, 1992]

The three maps discussed in this section use mutual event lightcurves to provide resolution in latitude for the sub-Charon hemisphere of Pluto. One of them, the Maximum Entropy Map, also uses mutual events ('superior' events, meaning that Pluto occulted Charon) to get better resolution of Charon's sub-Pluto hemisphere. The other maps are only concerned with Charon during the six hour duration of an event, so they assume a constant magnitude for Pluto's satellite.

The Eleven Panel Map was the first to detect Pluto's surprisingly bright south pole. Previous maps indicated that Pluto's south pole is smaller and darker than the north polar region.

The Eleven Panel Map divides the sub-Charon hemisphere of Pluto into four bands of latitude. Each of these is divided two or more times in longitude. The normal reflectance of each panel is a free parameter, for a grand total of eleven free parameters. Once the relative brightness of each panel is found, all of the parameters are scaled such that the total area-averaged normal reflectance is equal to 0.49. Pluto's observed sub-Charon geometric albedo is 0.49 [Mulholland and Binzel, 1984], and the normal reflectance is equal to the geometric albedo given a Minnaert limb parameter of 0.5. We used a linear least squares fitting algorithm to solve for a surface albedo distribution. This gives the model an advantage in speed and convenience, but necessitates leaving out nonlinear physical processes, such as Hapke surface scattering. Minnaert limb-darkening can be incorporated in a linear model and has been included in the Eleven Panel Map.

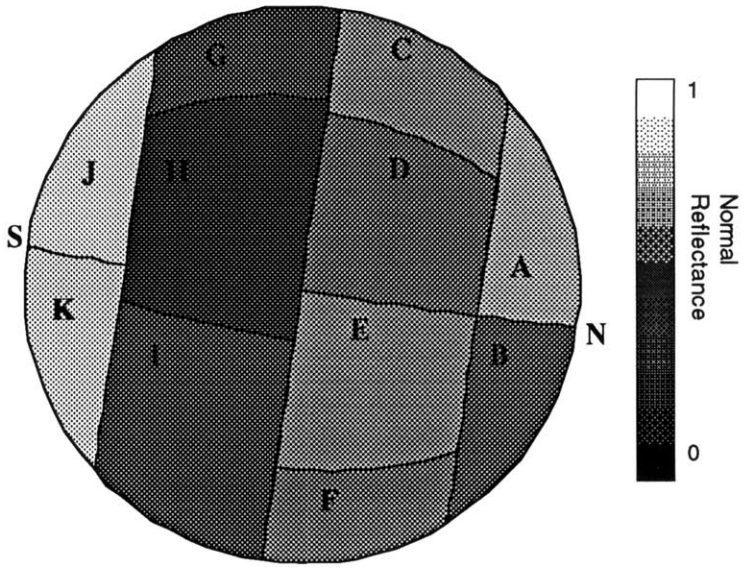

Figure 8. The least squares solution to the eleven panel map. Gray scales illustrate the normal reflectances for each panel: white = 1, black = 0.

Table 7. The Eleven Panel Map [Young, 1990] [Young and Binzel, 1990]

Panel	Normal Reflectances	Panel	Normal Reflectances
A	0.69 ±0.041	G	0.33 ±0.030
B	0.43 ±0.045	H	0.25 ±0.023
C	0.57 ±0.023	I	0.37 ±0.027
D	0.50 ±0.022	J	0.87 ±0.034
E	0.58 ±0.022	K	0.81 ±0.043
F	0.53 ±0.028		

It is worth mentioning why our maps are in terms of normal reflectances, as opposed to geometric albedos or bidirectional reflectances. Geometric albedo is a quantity defined for an entire sphere; namely, the ratio of light reflected by a planet relative to that reflected by an isotropic, perfectly reflecting disk of the same apparent size. We could talk about "local geometric albedos," but that would stretch the definition of geometric albedo. Bidirectional reflectance *is* locally defined [see Equation 1], but has values that are nonintuitive. For example, regions of Pluto that have normal reflectances of 0.8 - 0.9 may have bidirectional reflectances in the neighborhood of 0.15. The lower values are due to the definition of bidirectional reflectance. We use the normal reflectance instead.

The overall normal reflectance is easily related to the geometric albedo [Veverka et al., 1986, p. 377]:

$$r_n = (0.5 + k)\, p \tag{5}$$

where r_n is the normal reflectance,
k is the Minnaert limb-darkening parameter [see Equation 7], and
p is the planet's geometric albedo.

The quoted errors in Table 7 are the formal errors of the least squares problem. Specifically, the error in the i^{th} parameter is

$$\sigma_i = \sqrt{\frac{\chi^2}{n - m} \mathrm{Cov}[i, i]} \tag{6}$$

where n is the number of observations,
m is the number of parameters,
χ^2 is the sum of the squared weighted residuals, and
Cov[i, i] is the i^{th} diagonal element of the covariance matrix.

The Minnaert limb parameter, k, relates the intensity from the limb of a planet to the intensity at the center of the disk.

$$I = I_0 \cos^{2k-1}(\theta) \tag{7}$$

where I_0 is the intensity of the center of the planet's disk,
k is the Minnaert parameter, and
θ is the angle between the surface normal at the disk's center and the normal anywhere else on the planet.

We estimate the limb parameter by trying a range of values from k = 0 to k = 1.5 and plotting χ^2 as a function of k.

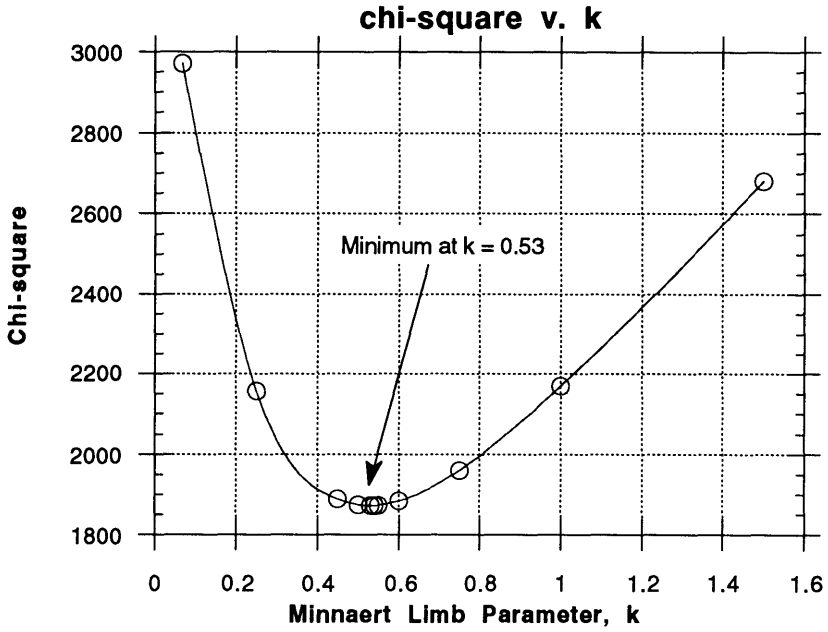

Figure 9. χ^2 as a function of k, the Minnaert limb parameter. A value of k = 0.5 indicates no limb-darkening effect. The minimum at k = 0.53 indicates only a slight amount of limb-darkening.

It should be no surprise that the best fit limb parameter is close to 0.5, since Tholen and Buie [1989] assumed non limb-darkened disks in their model. On the other hand, our preliminary nonlinear fit (which allowed for possible limb-darkening) found a limb coefficient of only 0.51 ± 0.022 for Pluto [Table 2]. In general one expects bright objects like Pluto or Europa to be strongly limb-darkened (for Europa k is about 0.70 [Veverka et al., 1986]), while the moon is not limb-darkened (k = 0.5). If Pluto does possess a haze layer, one might expect Pluto to be limb-brightened, because the projected optical thickness of the haze is greatest at the limbs, and the haze might be more effective at reflecting light at the limb. The optical properties of the lower atmosphere are unknown at this time, so the limb coefficient cannot be interpreted as if it is solely due to Pluto's surface.

The optical thickness of a possible haze layer brings up the question of whether the variation in the mutual event lightcurves is due surface features of atmospheric phenomena. The column abundances of methane, N_2 and CO are so low that we certainly see through them to the surface, unless there are aerosols suspended in the lower atmosphere [Cruikshank et al., 1989]. A limb coefficient of less than 0.5 (indicating

limb brightening) would have been evidence for an optically significant haze layer. The best evidence that we actually see surface features as opposed to, say, clouds is the long-term repetition in Pluto's rotational lightcurves.

The brightest region of the Eleven Panel Map is the south pole, panels J and K. The darkest region is the adjacent band, panels G, H, and I. The north pole, panels A and B, have an average brightness that is about the same as Pluto's global albedo of 0.5. The Eleven Panel Map's north and south pole albedos *contradict the results from the Two-Spot Model and the SHELF Model* . The other mutual event maps also contradict the rotation-based maps.

The European Southern Observatory Map is written up in the December 1991 issue of the *ESO Messenger* [Burwitz et al, 1991]. The ESO Map is a finite element map, like the Eleven Panel Map, except that it has 17 surface elements and has been smoothed. The authors remark on the surprising polar albedos of their map:

> Our albedo map reveals that areas of high contrast must coexist on the Charon-facing hemisphere of Pluto. The highest contrast found was that between the two polar caps. While the south polar region appears to be the brightest area on the planet, we found that the north polar region has the lowest albedo [Burwitz et al, 1991].

The latest map by Buie et al. [1992] uses a maximum entropy method to solve for pixel albedos on Pluto's surface. The maximum entropy method (MEM) is similar to a least squares technique in that both seek to minimize a merit function of some kind, usually the weighted sum of squared residuals. The difference is that the MEM tries to maximize a quantity called the entropy under the constraint that χ^2 is less than or equal to a target value, C_{aim}. Optimally C_{aim} should be unity, but it is not always possible to reach arbitrarily low values of C_{aim}.

> One maximizes S subject to the constraint $C < C_{aim}$. If the unconstrained maximum of S satisfies this constraint, then this will be the maximum entropy solution – the data are too noisy for any information to be extracted. Otherwise the solution will lie on the boundary $C = C_{aim}$ and we have an optimization problem with an equality constraint to solve. [Skilling and Bryan, 1980].

The entropy, S, is defined as the negative of the information content of a probability distribution.

$$S = -\sum p_i \log\left(\frac{p_i}{m}\right) \qquad (8)$$

where p_i is the i^{th} parameter, normalized to the range from 0 to 1, and m_i is some kind of initial estimate.

The MEM is used to solve the general problem of determining free parameters from

data sets that do not completely constrain the solution. Of the infinite number of solutions that would fit the data equally well, the MEM finds the one for which the information entropy is a maximum. Why is this particular solution a good choice?

Consider the Kangaroo Problem:
Suppose we know two things about kangaroos:

- One third of kangaroos have blue eyes.
- One third of kangaroos are left handed.

Now, what is the most reasonable probability that a kangaroo will be both left-handed and have blue eyes? We build a 2 x 2 sample space of the problem.

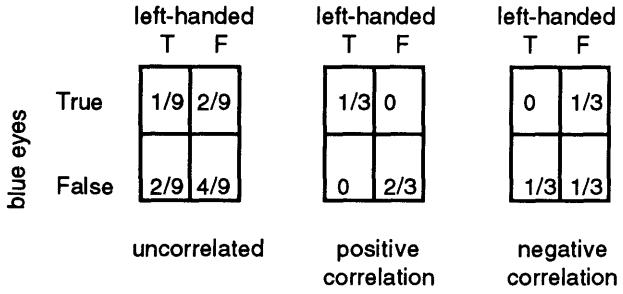

Figure 10. Sample space for the Kangaroo Problem.

There are many possible sample spaces that fit our knowledge of the kangaroo situation, but these three cases cover the extremes. In the absence of any information (e.g., are the genes for left-handedness and eye color on the same chromosome), the best choice for the sample space is the uncorrelated case. Now suppose we try to find the best set of probabilities not by inspection, but maximizing the entropy. *Only when we maximize the entropy do we get the uncorrelated result* . The entropy in Figure 10 is 1.27, 0.63, and 1.01 for the uncorrelated, positively correlated, and negatively correlated cases respectively. The entropy of the uncorrelated case is the highest. A solution in which some parameters are correlated represents an application of knowledge where none is justified by the data.

We can pose the albedo reconstruction problem as follows: divide Pluto's surface into a grid of surface elements, and let the albedo of each element be a free parameter. With any reasonably ambitious grid (e.g., 20 x 40), the solution will be underdetermined since there is not enough information to pin down the albedo of every pixel. We may know the sum of two adjacent pixels, but not know the distribution between them. There are an infinite number of solutions, but we want the one in which the pixel values are uncorrelated.

Buie et al. cast Eq. (8) in terms of the image value at each surface element.

$$S = \sum_{j=1}^{N} I_j - D_j - I_j \cdot \ln\left(\frac{I_j}{D_j}\right) \qquad (9)$$

where I_j is the image value of the j^{th} surface element,
D_j is the associated default value, and
N is the number of surface elements in the model.

The black art in the maximum entropy algorithm is in picking an expression for the default value, D_j, since it defines the entropy and will shape the solution in regions of poor data constraints. Often D_j is defined as the average image value based on the entire image [Skilling and Bryan, 1984]. Buie et al. use a more local definition of D_j; they define it as the average of a pixel and its eight neighbors. I suspect that this helps the MEM find a solution with sharper features. Notice that the MEM solution given C_{aim} and a definition of D_j is unique, but, since D_j can be defined different ways, there is not a unique "MEM solution" to a problem.

The results of Buie et al. confirm the results of the Eleven Panel Map and the ESO Map. They also find a bright south polar region and do not find a bright north polar region. "...a south polar cap is evident in the map of Pluto. The north polar region is brighter than the equatorial regions but is not as bright as the south pole [Buie et al. 1992]." We compare our maps to the MEM map in section **F** of Chapter III.

III. Recent Least Squares Solutions

This chapter describes three separate linear least squares models of Pluto's surface albedo [Young and Binzel, 1992]. Each model introduces some structure into the solution, so comparisons from a set of solutions help us recognize features that may be artifacts of one particular model. This is the motivation for using three distinct models, which are

- The Spherical Harmonic Model,
- The Polynomial Model, and
- The Finite Element Model.

In all three of the models the free parameters appear as linear terms. The advantage of linear models is speed; a least squares fitting routine will find a solution in a single iteration. A clear explanation of the linear least squares problem is given in section 14.3 of *Numerical Recipes* (either C or Fortran versions) [Press et al. 1988].

The three models all have a similar form, representing Pluto's apparent intensity as:

$$I(t) = \sum_{i=1}^{N} \left(\sum_{\text{all } \theta,\, \phi} p_i \, X_i(\theta,\phi;t) \right) \tag{10}$$

where I(t) = Pluto's intensity at time t,
N = number of parameters in the model,
p_i = the i^{th} parameter, and
X_i = the i^{th} basis function.

The basis functions are functions of latitude and longitude as well as functions of time, since they incorporate the temporal effects of Pluto's rotation and the coverage by Charon and its shadow. For example, consider a set of spherical harmonics. The basis function $X_i(\theta,\phi;t)$ is identical to the i^{th} spherical harmonic, $Y_{LM}(\theta,\phi)$, except that each point on Pluto is attenuated by a projection factor, and points that are hidden by Charon or its shadow or behind the limb of the planet at time t are simply zero. Charon's coverage and the projected area of a patch on Pluto's surface are clearly time dependent phenomena; thus X_i is a function of t, even though the i^{th} spherical harmonic is not. A comparison of Eq. (10) and Eq. (14) shows that the basis functions $X_i(\theta,\phi;t)$ are really the product of some function that is defined on a sphere (like $Y_{LM}(\theta,\phi)$) and the exposed, projected area of the surface element at θ,ϕ at time *t* (otherwise known as $g(\theta,\phi;t)$). Each basis function is evaluated on a 100 x 100 grid covering Pluto's sub-

Charon hemisphere. Because Pluto rotates 12°- 15° during an event, we extend the grid slightly beyond the sub-Charon hemisphere, from 97.5°W to 97.5°E. Although Charon never transits longitudes beyond ±90°, those longitudes of Pluto are visible during an event. The extent in latitude is from 90°S to 90°N.

The total model contribution is the linear combination of all the basis functions evaluated at all of the grid elements with each grid element's projected area scaling the function's value. The projected area of an infinitesimal grid element is

$$da = (\hat{n}\cdot\hat{p})r^2 \cos\theta \, d\theta \, d\phi \tag{11}$$

where θ = latitude,

ϕ = longitude,

r = planetary radius,

$d\theta$, $d\phi$ = pixel's extent in latitude and longitude,

$\hat{n}$ = the normal vector from the planet's surface at θ, ϕ, and

$\hat{p}$ = unit vector defining the projection plane.

The normal vector's components are

$n_x = \cos\theta\cos\phi$,

$n_y = \cos\theta\sin\phi$,

$n_z = \sin\theta$.

It is important that the normal to the projection plane, $\hat{p}$, be in the same coordinate system as the surface normal vector $\hat{n}$ (generally Pluto's local coordinate system). The vector $\hat{p}$ points from Pluto to the Earth.

What is the process of finding the least squares solution? We start with a *merit function* as the measure of the quality of the fit, defined to be the weighted sum of squared residuals, χ^2.

$$\chi^2 = \sum_{i=1}^{n} \left[\frac{y_i - I_i}{\sigma_i}\right]^2 \tag{12}$$

where n = number of data points,

y_i = the observed intensity for the i^{th} timestep,

σ_i = the error in y_i, the i^{th} observation, and

I_i = the model intensity for the i^{th} timestep.

Minimizing χ^2 is done in the usual way; first by taking the derivatives of χ^2 with respect to the parameters and setting them equal to zero (these are called the *normal*

equations) and then finding the parameter values that solve the normal equations. This last step amounts to solving the matrix equation

$$[\alpha]\,\bar{a} = \bar{\beta} \tag{13}$$

where $[\alpha]$ = the *design matrix*,

$\bar{a}$ = vector of least squares solutions for the n parameter values (i.e., the answers), and

$\bar{\beta}$ = vector of weighted observations.

We solve for the parameters by inverting the matrix $[\alpha]$ in Eq. (13). If two of the parameters are closely correlated, or if the data set provides no means of distinguishing the contribution of one parameter from another, then the matrix $[\alpha]$ will be nearly singular, resulting in nonsense or a non-unique solution when we try to invert it. We deal with this likely possibility by using singular value decomposition (SVD) to invert the matrix $[\alpha]$. When a matrix is singular, an infinite number of vectors $\bar{a}$ will satisfy Eq. (13), since the contribution from one row of $[\alpha]$ is zero, regardless of the vector $\bar{\beta}$. The SVD is robust in this situation, and returns the solution that distributes power most evenly among the correlated parameters. An advantage of least squares techniques, including the SVD implementation, is that they produce a correlation matrix that can identify correlated parameters. This ability turns out to be critical in selecting free parameters for the three models.

A. The Spherical Harmonic Map

The spherical harmonic model represents Pluto as a linear combination of terms from a truncated spherical harmonic series.

$$X_i(\theta,\phi;t) = g(\theta,\phi;t)\, Y_{LM}(\theta,\phi) = g(\theta,\phi;t) \sqrt{\frac{2L+1}{4\pi}\frac{(L-M)!}{(L+M)!}}\, P_L^M(\cos\theta)\, e^{iM\phi} \tag{14}$$

where θ = colatitude, ϕ = longitude,

$g(\theta, \phi;t)$ = the *exposed, projected* area of a surface area element at θ, ϕ at time t.

$Y_{LM}(\theta,\phi)$ = the spherical harmonic of order L, M,

and $P_L^M(\cos\theta)$ is the associated Legendre polynomial.

These terms are complex when $M > 0$, so the real and imaginary parts are effectively different basis functions. Alternatively, one could use an imaginary parameter set, in which case the imaginary part of each complex parameter is a free parameter in its own right. We do not require that both the real and imaginary parts of a spherical harmonic term be included in the fit. The free parameters are the amplitudes of the various spherical harmonic terms (the p_i's in Eq. (10)). Our goal is to find the set of p_i's that,

when multiplied by their respective spherical harmonic terms, yield a model of Pluto that best duplicates the observed occultation lightcurves.

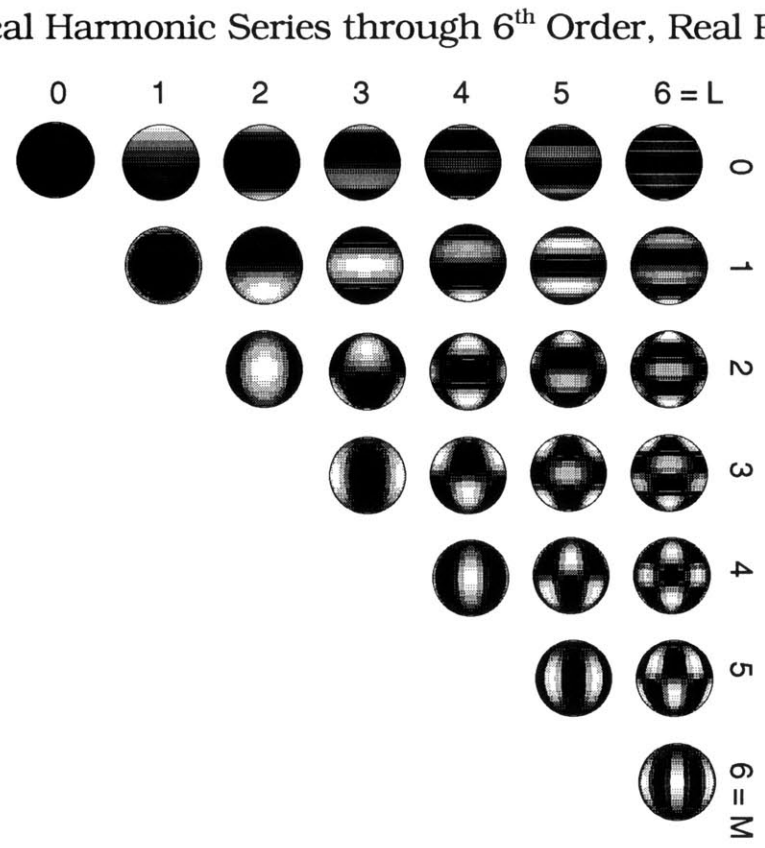

Figure 11. Real (even) part of the spherical harmonic series though the sixth order.

Spherical Harmonic Series through 6th Order, Imaginary Part

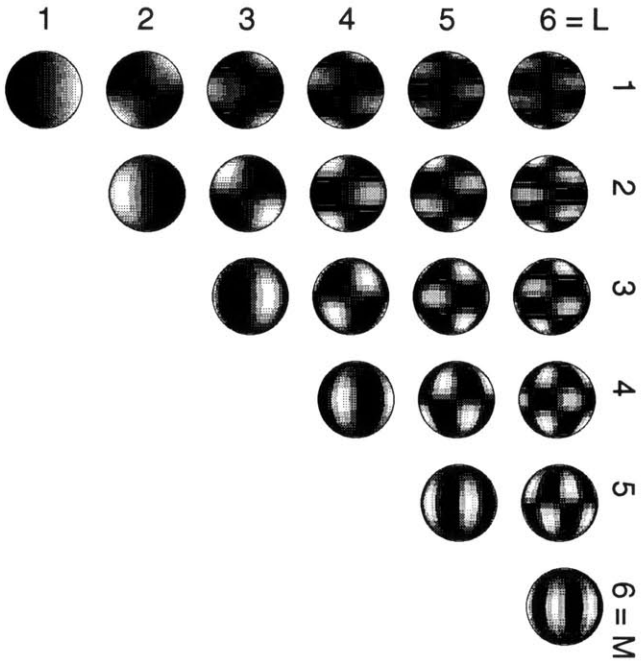

Figure 12. Imaginary (odd) part of the spherical harmonic series through the sixth order.

The question of which parameters to include in the model proved a difficult one. In many models based on series expansions, there is a clear point at which one can truncate higher order terms. This is not the case in the spherical harmonic decomposition. The normalized correlation matrix shows that there are *families* of highly correlated parameters, where the members of each family look similar. For example, Figure 11 shows that the (2,0), (3,1) and (4,0) even terms are members of the same family; all three functions are basically spheres with symmetrical north-south polar caps. Although these three functions should be orthogonal, the data set's coverage of Pluto's sphere is restricted to one hemisphere, and that hemisphere is resolved into only six bands. This limited coverage results in an inability to distinguish similar terms from each other. Our solution is to discard all but the lowest order member of each family. These families are shown in Table 8, which lists pairs of parameters with cross correlation coefficients with magnitudes larger than 0.95.

In the next section we will use polynomials of latitude and longitude as a basis set instead of spherical harmonics. The polynomial set is not orthogonal on a sphere even with complete coverage. Our solution is to check the relative sizes (condition number) of

the singular values from the SVD. The finite element and spherical harmonic set may also contain linear dependencies due to the uneven coverage by Charon's transits, so the SVD is essential in all of the least squares fits.

Table 8. Correlated parameters in the spherical harmonic solution.

High Order Term	Low Order Term	Correlation Coefficient
Y(6,6) odd	Y(5,5) odd	0.99
Y(6,6) odd	Y(4,4) odd	0.96
Y(6,5) odd	Y(5,4) odd	0.98
Y(6,4) odd	Y(5,3) odd	0.97
Y(6,3) odd	Y(5,2) odd	0.99
Y(6,3) odd	Y(4,1) odd	0.98
Y(6,2) odd	Y(5,1) odd	0.97
Y(5,5) odd	Y(4,4) odd	0.99
Y(5,4) odd	Y(4,3) odd	0.99
Y(5,4) odd	Y(3,2) odd	0.97
Y(5,4) odd	Y(2,1) odd	0.97
Y(5,3) odd	Y(5,1) odd	-0.96
Y(5,3) odd	Y(4,2) odd	0.98
Y(5,3) odd	Y(3,1) odd	0.96
Y(5,2) odd	Y(4,1) odd	0.99
Y(5,1) odd	Y(4,2) odd	-0.97
Y(5,1) odd	Y(3,1) odd	-0.96
Y(4,4) odd	Y(3,3) odd	0.96
Y(4,3) odd	Y(3,2) odd	1.00
Y(4,3) odd	Y(2,1) odd	1.00
Y(4,2) odd	Y(3,1) odd	0.99
Y(3,2) odd	Y(2,1) odd	1.00
Y(2,2) odd	Y(1,1) odd	0.98
Y(6,6) even	Y(5,5) even	0.99
Y(6,6) even	Y(4,4) even	0.97
Y(6,6) even	Y(3,3) even	0.96
Y(6,5) even	Y(5,4) even	0.99
Y(6,5) even	Y(4,3) even	0.96
Y(6,4) even	Y(5,3) even	0.95
Y(6,2) even	Y(5,1) even	0.98
Y(6,1) even	Y(5,2) even	-0.96
Y(6,1) even	Y(5,0) even	0.98
Y(5,5) even	Y(4,4) even	1.00
Y(5,5) even	Y(3,3) even	0.99
Y(5,4) even	Y(4,3) even	0.99
Y(5,4) even	Y(3,2) even	0.97
Y(5,2) even	Y(5,0) even	-0.98
Y(5,2) even	Y(4,1) even	0.97
Y(5,1) even	Y(4,0) even	0.98
Y(5,0) even	Y(4,1) even	-0.98
Y(4,4) even	Y(3,3) even	1.00
Y(4,3) even	Y(3,2) even	0.98
Y(4,1) even	Y(3,0) even	0.97
Y(2,1) even	Y(1,0) even	0.99
Y(1,1) even	Y(0,0) even	1.00

Table 9 shows the least squares solution for the spherical harmonic case. None of the 16 parameters has a singular value near zero. (More importantly, none of the

parameters has a condition number close to the computer's resolution. The condition number is the ratio of a singular value to the largest singular value.)

Table 9. Parameter list for the spherical harmonic solution.

Parameter	value	error	singular value
Y(0,0) (even)	3.858	± 0.11	1.16e+03
Y(1,0) (even)	-0.07	± 0.02	1.75e+02
Y(2,0) (even)	1.278	± 0.15	1.06e+02
Y(2,2) (even)	0.266	± 0.40	7.00e+01
Y(3,0) (even)	0.599	± 0.08	5.51e+01
Y(3,2) (even)	0.983	± 0.06	4.70e+01
Y(3,3) (even)	0.617	± 0.32	3.38e+01
Y(4,2) (even)	-0.72	± 0.15	2.99e+01
Y(5,0) (even)	2.605	± 0.14	2.11e+01
Y(5,1) (even)	-0.71	± 0.26	1.48e+01
Y(6,0) (even)	0.470	± 0.32	1.24e+01
Y(1,1) (odd)	-0.04	± 0.02	1.08e+01
Y(2,1) (odd)	0.038	± 0.08	7.77e+00
Y(3,1) (odd)	-0.58	± 0.07	2.53e+00
Y(4,1) (odd)	0.467	± 0.18	3.04e+00
Y(6,1) (odd)	1.220	± 0.24	4.78e+00

The χ^2 per degree of freedom is 1.82 for the spherical harmonic model.

We pause momentarily to explain how the errors are determined for each point on the surface. The error *of each parameter* is estimated from the formal error of the least squares fit.

$$\sigma_i = \sqrt{\frac{\chi^2}{n - N} \mathrm{Cov}[i, i]} \tag{15}$$

where σ_i = the error in the i^{th} parameter,

n = number of observations,

N = number of parameters,

χ^2 = chi square, the sum of weighted, squared residuals, and

Cov[i, i] = the i^{th} diagonal element of the covariance matrix.

The errors at any point on the surface are calculated by propagating the parameter errors. If the albedo, $s(\theta, \phi)$, at any point is given by

$$s(\theta, \phi) = p_1 X(\theta, \phi)_1 + p_2 X(\theta, \phi)_2 + ...+p_N X(\theta, \phi)_N, \quad (16)$$

then the albedo's variance at that point is

$$\sigma^2(\theta, \phi) = \left(X(\theta, \phi)_1\right)^2 \sigma^2(p_1) + \left(X(\theta, \phi)_2\right)^2 \sigma^2(p_2) + ... + \left(X(\theta, \phi)_N\right)^2 \sigma^2(p_N) + \text{cross correlation terms} \quad (17)$$

where p_i = the i^{th} parameter,

$X(\theta, \phi)_i$ = the i^{th} basis function evaluated at lat. = θ, long. = ϕ,

and each cross correlation term (there are $(N - 1)^2/2$ altogether) is of the form

$$\text{cross corr. error} = 2\rho \frac{\partial s}{\partial p_i} \frac{\partial s}{\partial p_j} \sigma(p_i) \sigma(p_j), \quad (18)$$

where ρ = the (i,,j) element of the normalized covariance matrix.

The solution maps (Figures 15, 16 and 17) show that the errors near the limb are much larger than the errors for the rest of the planet. The solutions are problematic near the limb because of the geometry of the events. The east and west limbs are visible only for the first and last parts of an event; they rotate out of and into view as the event progresses. The extreme east and west longitudes (from 97.5° to 90° E and from 90° to 97.5° W) are never occulted by Charon, but must be included in the model because they are visible during the early and late stages of an event. Furthermore the north and south limbs are only occulted roughly half the time, since the 1985-86 events hide the north pole and the 1989-90 events hide south pole. Since the limb regions are marginal contributors to the overall lightcurve, the least squares solution can be absurdly high or low in those areas without affecting the total χ^2 very much. A partial solution to this problem is to include as many early (1985-86) events and late (1989-90) events as possible. In the meantime, we have to be skeptical of the albedo solutions found for the limb regions. It may also be the case that there is an optically thick layer that obscures more of the planet near the limb.

B. The Polynomial Map

The polynomial model has as its basis function polynomials of latitude and longitude.

$$X_i(\theta,\phi;t) = g(\theta,\phi;t)\, P_{a,b}(\theta,\phi) = g(\theta,\phi;t)\, \theta^a \phi^b \quad (19)$$

where θ = latitude, ϕ = longitude, a and b are integers, and

$g(\theta, \phi; t)$ = the *exposed, projected* area of a surface area element at θ, ϕ at time t.

The free parameters are amplitudes of the polynomial functions (the p_i's in Eq. (10)). The set of polynomial functions are illustrated in Figure 13.

Polynomials of Latitude and Longitude through 8th Order

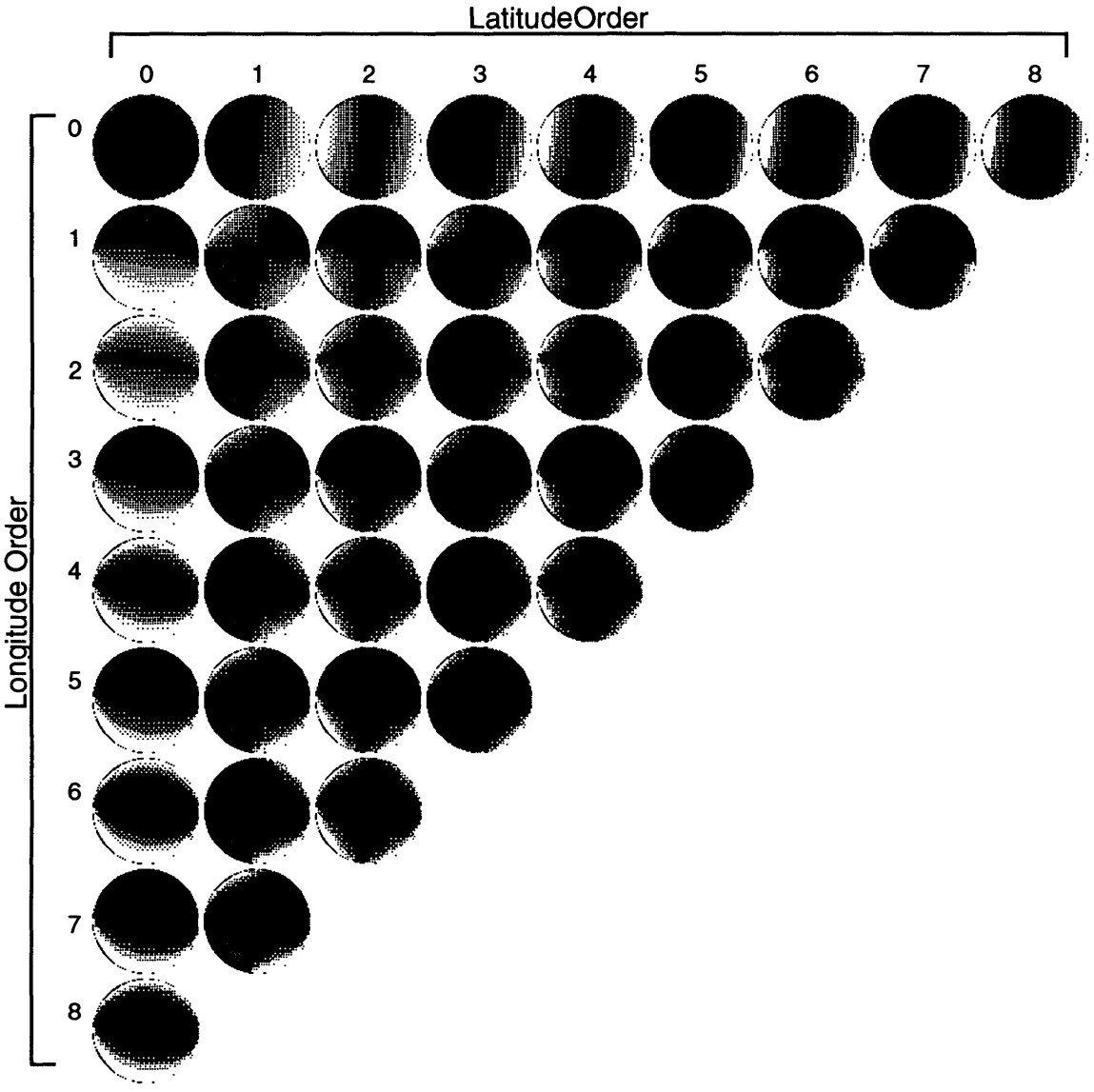

Figure 13.

Although Figure 13 shows polynomials through 8th order, we only included terms up

through sixth order in the actual polynomial model. Given only six transits by Charon, any higher order terms would over-fit the data. We observed singular values that were zero or very small when we included 7th and 8th order terms, indicating that the additional terms were not improving the model's ability to fit the data.

In contrast to the spherical harmonic model, the sixth order polynomial model only has 2 pairs of terms (out of 28) with cross correlations of 0.95 or higher, as opposed to the spherical harmonic case, which has over 30 pairs (out of 49 total). The amplitudes of even the most highly correlated terms are of reasonable size in the polynomial case, whereas in the spherical harmonic case there often are delicately balanced amplitudes one hundred times larger than the rest of the set. The two correlated parameters are shown in Table 10, and the least squares solution for the polynomial model is shown in Table 11. As before, we keep only the lowest order parameter in each cluster of correlated parameters.

Table 10. Correlated Parameters in the 6th Order Polynomial Solution.

High Order Term	Low Order Term	Correlation Coefficient
Lat^0 * Lon^6	Lat^0 * Lon^4	-0.97
Lat^3 * Lon^1	Lat^5 * Lon^1	-0.95

Table 11. Parameter list for the polynomial solution.

Parameter	value	error	singular value
Lat^0 * Lon^0:	0.920	0.04	5.03e+03
Lat^0 * Lon^1:	0.207	0.09	9.96e+02
Lat^1 * Lon^0:	3.887	0.21	6.50e+02
Lat^0 * Lon^2:	0.191	0.20	1.77e+02
Lat^1 * Lon^1:	-0.431	0.27	1.50e+02
Lat^2 * Lon^0:	-1.906	0.67	1.35e+02
Lat^0 * Lon^3:	0.098	0.19	9.37e+01
Lat^1 * Lon^2:	-0.212	0.30	7.43e+01
Lat^2 * Lon^1:	-0.677	0.61	5.09e+01
Lat^3 * Lon^0:	-12.24	0.81	3.84e+01
Lat^0 * Lon^4:	-0.213	0.14	3.30e+01
Lat^1 * Lon^3:	-0.057	0.39	2.52e+01
Lat^2 * Lon^2:	0.949	0.55	1.41e+01
Lat^3 * Lon^1:	0.380	0.37	1.09e+01
Lat^4 * Lon^0:	3.902	1.52	8.55e+00
Lat^0 * Lon^5:	-0.059	0.10	7.08e+00
Lat^1 * Lon^4:	-1.327	0.28	5.44e+00
Lat^2 * Lon^3:	-0.317	0.43	4.91e+00
Lat^3 * Lon^2:	1.734	0.31	4.41e+00
Lat^4 * Lon^1:	0.494	0.39	3.38e+00
Lat^5 * Lon^0:	6.748	0.48	6.56e-01
Lat^1 * Lon^5:	0.290	0.21	1.11e+00
Lat^2 * Lon^4:	1.116	0.35	1.63e+00
Lat^3 * Lon^3:	-0.126	0.49	2.03e+00
Lat^4 * Lon^2:	-1.789	0.34	2.61e+00
Lat^6 * Lon^0:	-1.408	0.73	2.49e+00

The χ^2 per degree of freedom is 1.53 for the sixth order polynomial model.

C. The Finite Element Map

The Finite Element Model [Young 1990] [Young and Binzel, 1991] divides Pluto into contiguous panels of latitude and longitude. The brightness of each panel is a free parameter in the least squares fit.

$$X_i(\theta,\phi;t) = g(\theta,\phi;t)\, P_i(\theta,\phi) \qquad (20)$$

where θ = latitude, ϕ = longitude, and

$P_i(\theta,\phi)$ is the *brightness of the i^{th} panel*, the panel that encloses the coordinates (θ,ϕ).

We divide Pluto into a 6 x 6 grid, or 36 free parameters. The 36 panel finite element solution is shown in Figure 14 and Table 12.

Mercator projection of the 36 Panel Finite Element Map

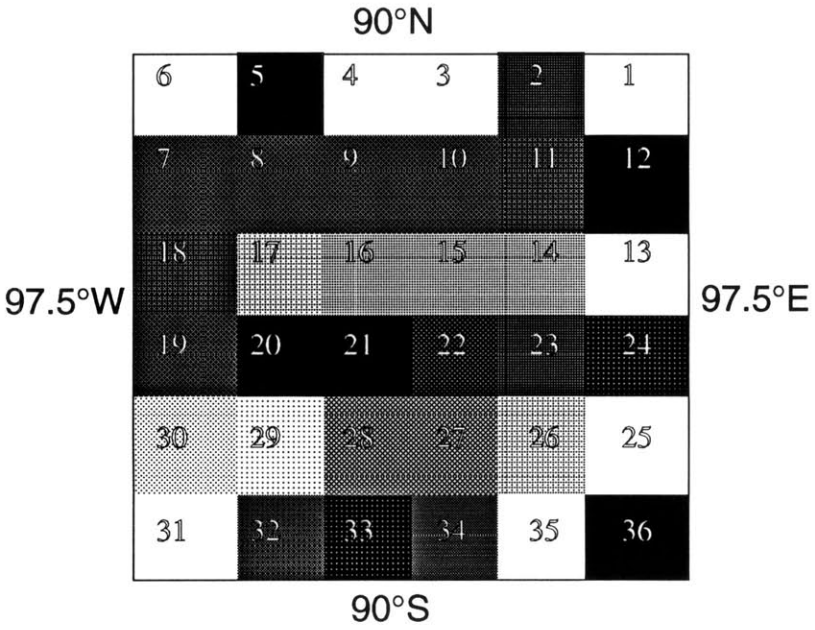

Figure 14. The Finite Element Model solution. Panel indices refer to Table 12.

Table 12. Parameter list for the 36 panel finite element solution.

Parameter	value	error	singular value
1	7.187	2.90	8.09e+02
2	0.573	1.67	1.16e+02
3	2.134	1.38	1.08e+02
4	4.558	1.34	5.89e+01
5	-2.048	1.91	4.78e+01
6	5.968	2.79	3.99e+01
7	0.754	0.38	3.38e+01
8	0.818	0.15	2.66e+01
9	0.796	0.13	2.30e+01
10	0.732	0.19	2.14e+01
11	0.688	0.16	2.02e+01
12	-0.579	0.51	1.48e+01
13	2.163	0.29	1.28e+01
14	1.456	0.13	1.18e+01
15	1.485	0.12	1.03e+01
16	1.459	0.08	9.84e+00
17	1.539	0.10	9.39e+00
18	0.679	0.21	8.28e+00
19	0.733	0.23	6.20e+00
20	0.024	0.13	6.26e+00
21	-0.020	0.08	4.68e+00
22	0.255	0.11	4.09e+00
23	0.574	0.18	3.38e+00
24	0.148	0.44	2.84e+00
25	3.656	0.33	2.60e+00
26	1.612	0.15	1.96e+00
27	1.179	0.12	1.90e+00
28	1.266	0.13	1.36e+00
29	1.818	0.27	1.29e+00
30	1.647	0.80	1.06e+00
31	16.18	3.51	3.05e-01
32	0.842	1.34	7.99e-01
33	0.210	0.96	6.13e-01
34	0.955	1.09	6.71e-01
35	4.111	1.56	4.78e-01
36	-18.31	3.33	4.89e-01

The χ^2 per degree of freedom is 2.01 for the finite element model with 36 free parameters.

All of the maps, particularly the finite element map, demonstrate the effects of noise in the lightcurves: bright and dark regions adjacent to each other with large swings in albedo. The small elements near the polar regions are especially sensitive to noise. We

smooth the maps by convolving them with an adaptive Gaussian-shaped filter, described in Appendix B. The width of the Gaussian depends on the formal error of the pixel being smoothed, so regions with higher errors are smoothed more heavily. For example, the finite element map contains two adjacent panels, #35 and #36, with out-of-bounds reflectances of 4.1 and -18.3 respectively. Neither of these panels affects the smoothed map very much, however, because their projected areas are extremely small and their associated errors are high.

The spherical harmonic, polynomial and finite element maps are shown in Figures 15, 16, and 17. Each figure shows both the original and smoothed versions of the map, as well as a contour map of the formal errors associated with the original map.

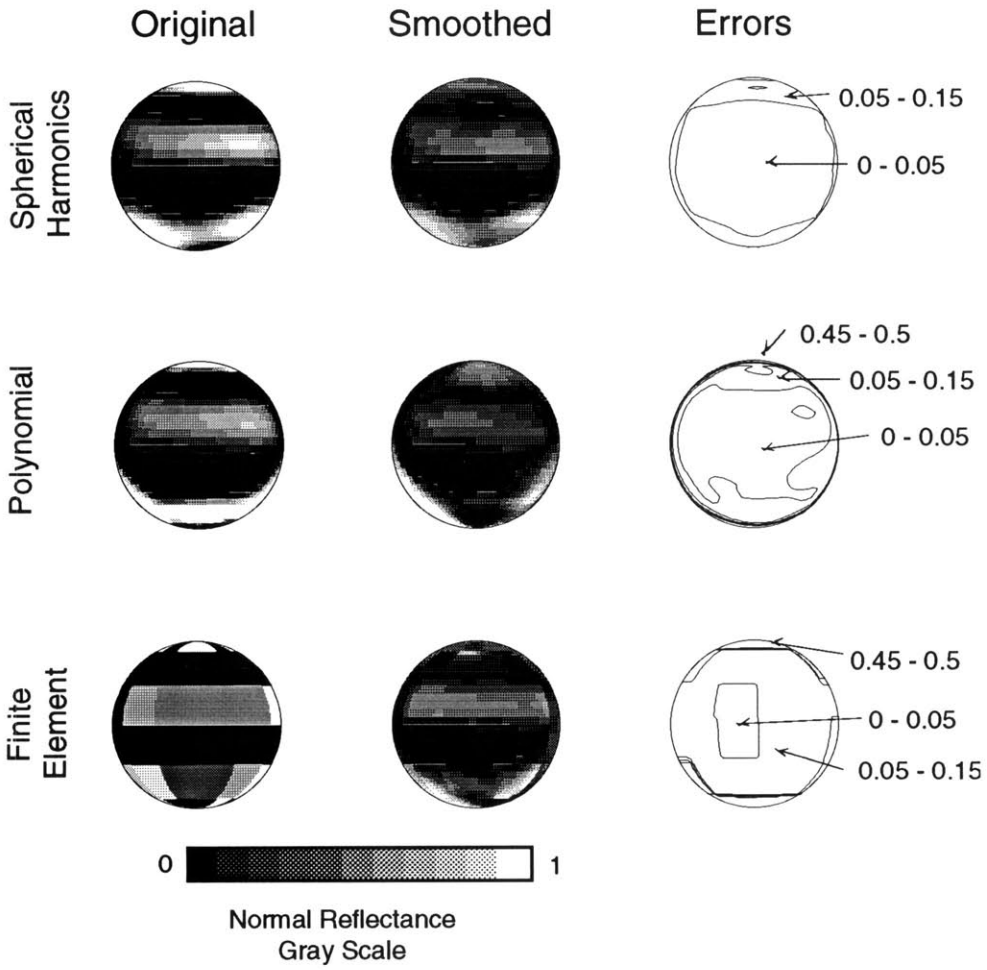

Figure 15. Normal reflectance maps of Pluto showing Pluto's sub-Charon hemisphere.

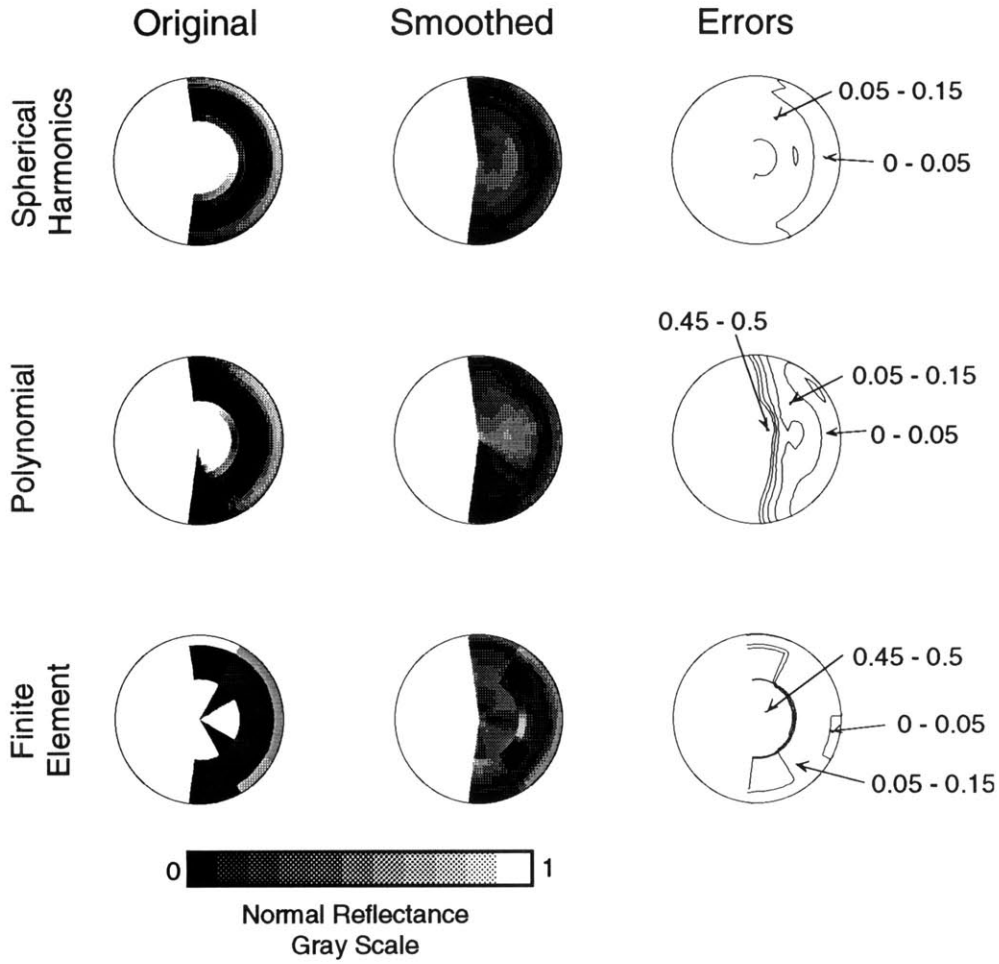

Figure 16. Normal reflectance maps of Pluto showing Pluto's north pole.

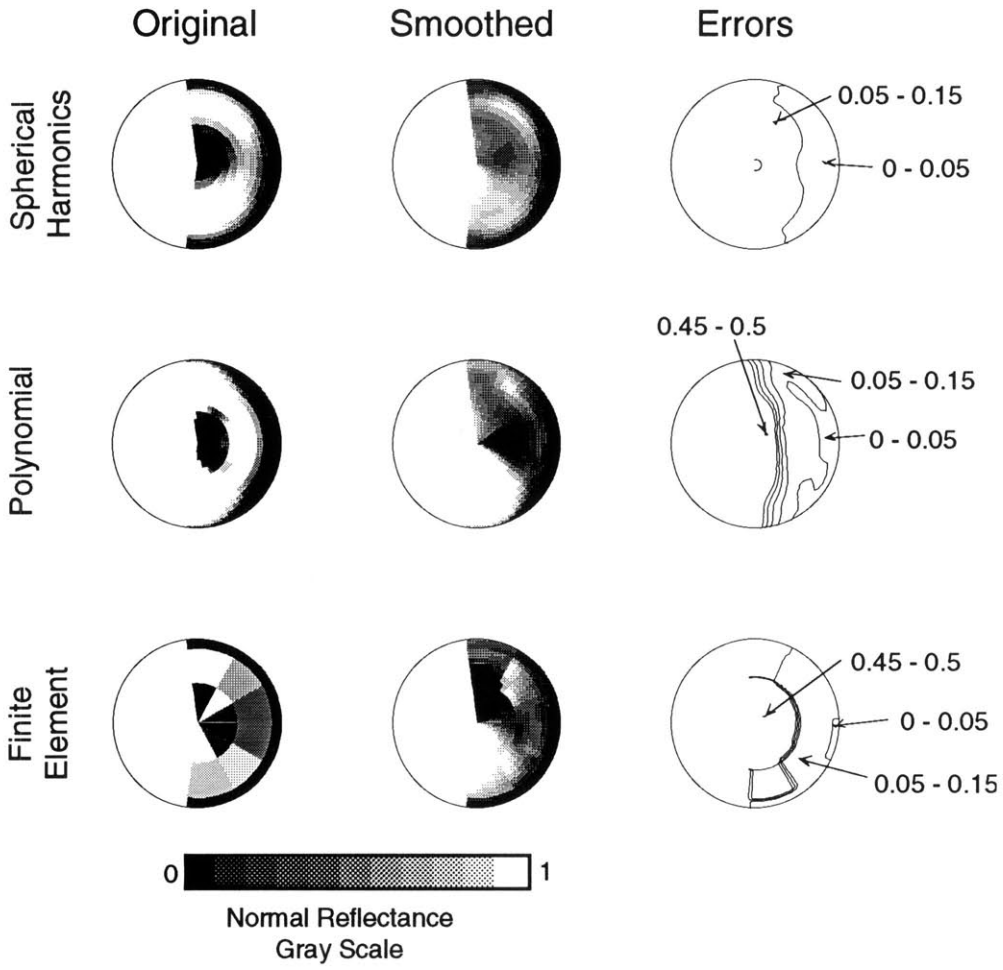

Figure 17. Normal reflectance maps of Pluto showing Pluto's south pole.

D. The Extreme Poles

All three maps exhibit apparent artifacts at the poles: a localized bright area at the extreme north pole and a dark area at the extreme south pole. The uncertainties at the pole are high, as discussed in Section A of this chapter. Is there a direct way to determine the actual albedos at the extreme latitudes? In 1985 and 1990 Charon grazed over Pluto's north and south polar regions respectively. We can run "spot checks" calculating the average albedo of the covered portion of Pluto for an individual observation. At individual timesteps, we compare the area covered to the fractional decrease in brightness relative to the pre- or post-eclipse baseline value. The ratio of the fractional decrease in brightness over the fractional decrease in exposed area is equal to the albedo of the covered region relative to Pluto's average albedo. The fractional area covered and the corresponding decrease in observed brightness are listed in Table 13 for

several points in the 1985 and 1990 lightcurves. The lightcurve geometry is shown in Figure 18.

Table 13. Spot checking the albedos of the extreme north and south poles.

17 FEB 1985 Hours since mid-event	(North Pole Coverage) Exposed Area (Percent)	Observed Intensity	Average Brightness of Covered Part (rel. to Pluto)
-0.67	97.9	0.964	0.587
-0.50	97.0	0.961	0.762
-0.31	96.3	0.960	0.912
-0.10	95.8	0.957	0.992
0.14	95.8	0.955	0.940
0.32	96.1	0.982	2.189
0.52	96.8	0.985	2.205
0.70	97.6	0.985	1.629
0.89	98.6	0.996	3.609
	Average:	1.5 ± 0.98	(Perhaps bright; error too large)

24 FEB 1990 Hours since mid-event	(South Pole Coverage) Exposed Area (Percent)	Observed Intensity	Average Brightness of Covered Part (rel. to Pluto)
-0.257	99.0	0.991	1.05
-0.105	98.7	0.990	1.29
-0.082	98.7	0.983	0.77
-0.011	98.6	0.978	0.65
0.023	98.5	0.988	1.17
0.046	98.5	0.984	0.95
0.082	98.5	0.978	0.66
0.105	98.5	0.980	0.74
)			
	Average:	0.91 ± 0.24	(Darker than its neighborhood

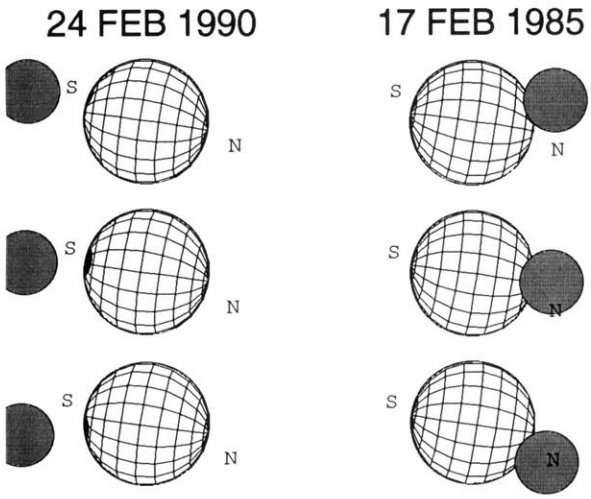

Figure 18. Geometry of the 1985 and 1990 mutual events. The 1985 event provides coverage of Pluto's north polar latitudes, while the 1990 event (a very shallow shadow event) covers Pluto's south polar latitudes.

The 1985 lightcurve indicates a mean albedo for the transited region of 0.75 ± 0.5 (150 % of Pluto's average). The 1985 lightcurve supports the least squares models by finding a bright region on the extreme north polar cap. The scatter in the 1985 lightcurve is so great that we cannot conclude that this feature is real at any reasonable confidence level. The 1990 lightcurve shows an albedo for the extreme south pole of 0.45 ± 0.12, lower than the surrounding region. The scatter from this lightcurve is low enough to suggest that the extreme south pole has local darkening that is real.

E. Reconstruction of Synthetic Maps

We generate lightcurves from four synthetic Plutos to test the ability of each model to reconstruct Pluto's surface albedo distribution . Each synthetic Pluto has regularly spaced black squares on a white background. The squares range in extent from 72 km to 1152 km. The synthetic lightcurves were constructed by stepping through the geometry of the six mutual events in our data set and calculating the exposed brightness of the artificial Pluto at each timestep. Using the synthetic lightcurves as input, we try to reconstruct the albedo distributions from which they were generated. These reconstructions are shown in Figure 19.

Reconstructions of Synthetic Plutos

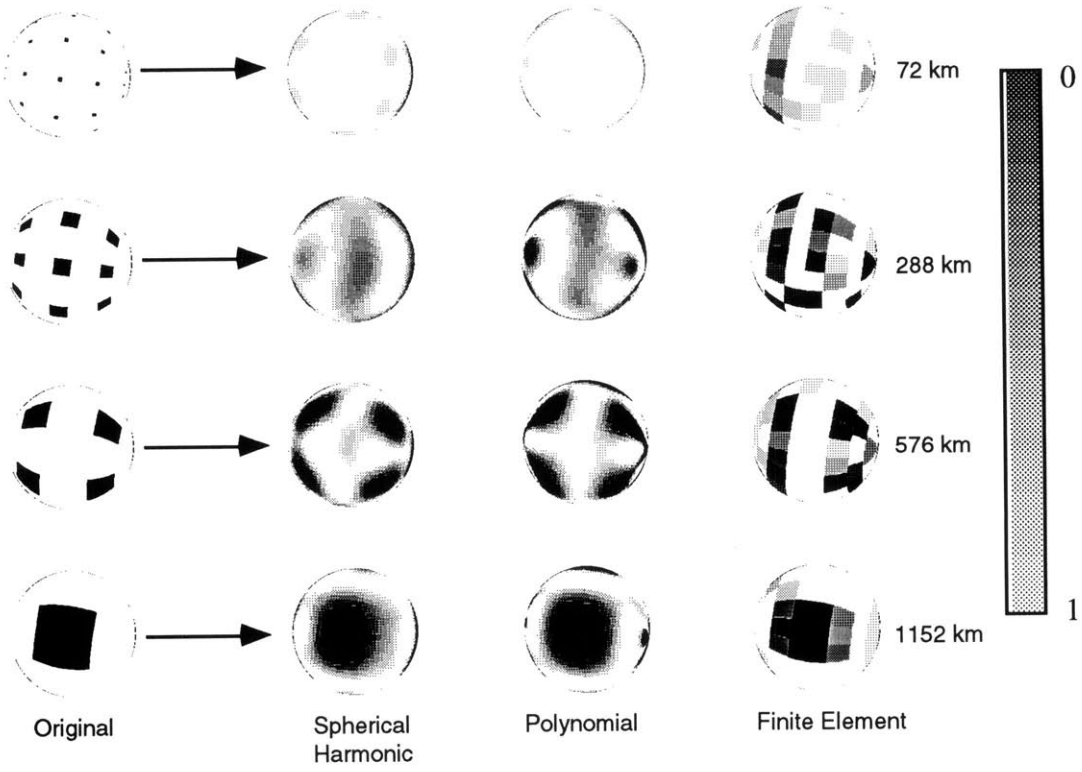

Figure 19.

The reconstructions tell us two things: first, they demonstrate the resolving ability of the surface maps to be about 400 - 500 km. The reconstructions easily reproduce the 580 km features, but have trouble reproducing the 290 km features. Second, the reconstructions confirm that all three models produce similar reconstructions of the synthetic maps.

A related test of the Pluto maps is a comparison of model-generated lightcurves to the observed lightcurves. Figure 20 compares lightcurves generated from the spherical harmonic with the observed lightcurves. The boxes □ represent observed points, the solid lines are generated by the spherical harmonic model, and the bottom line is uses an expanded scale to show the residues. To the right of the residue plot is a typical error bar of the observed points.

17 FEB 1985

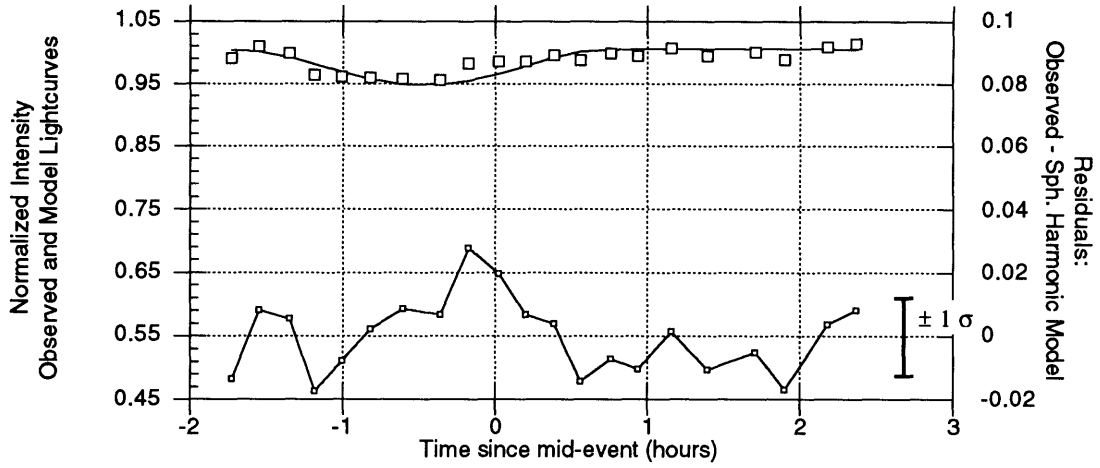

20 MAR 1986

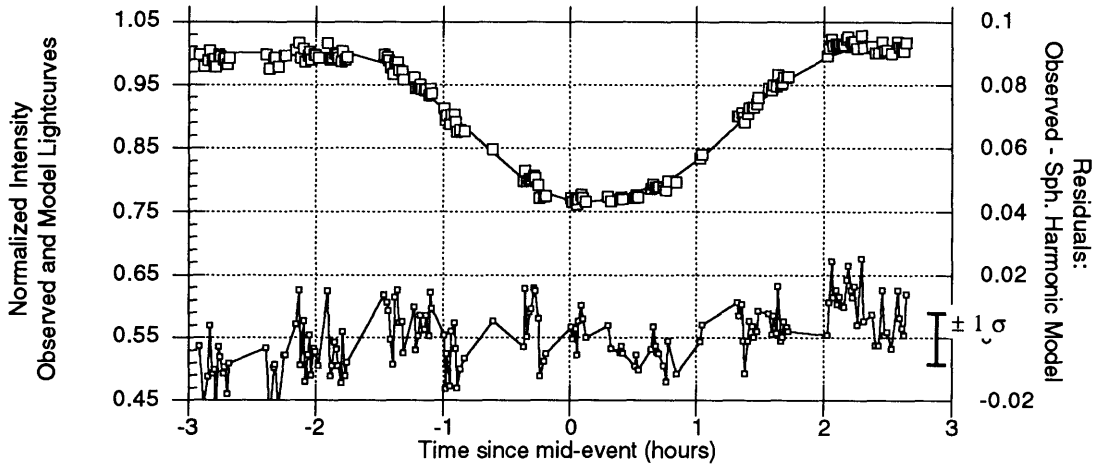

22 MAY 1987

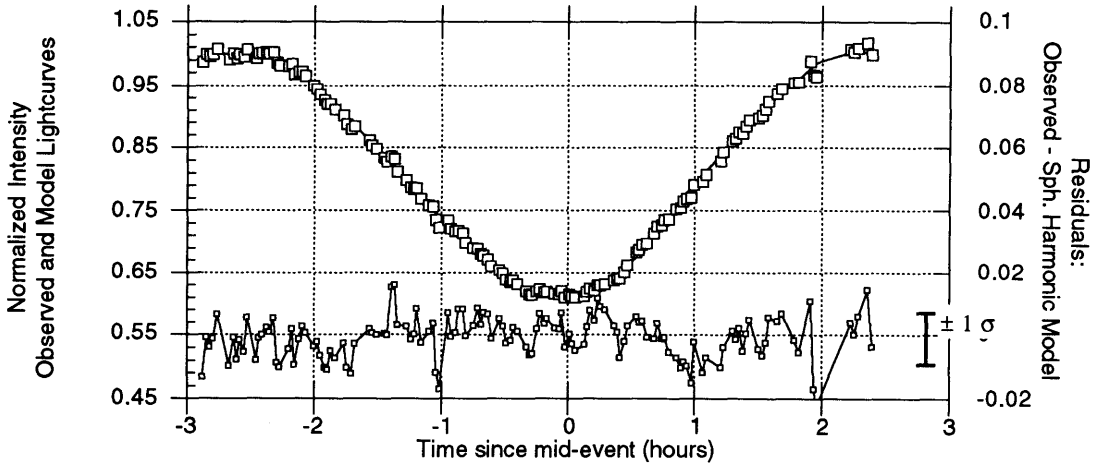

18 APR 1988

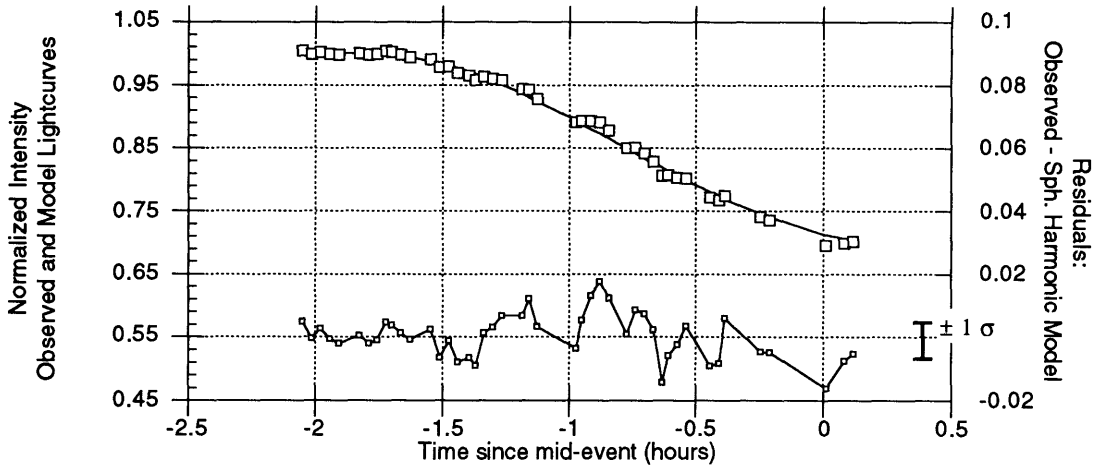

30 APR 1989

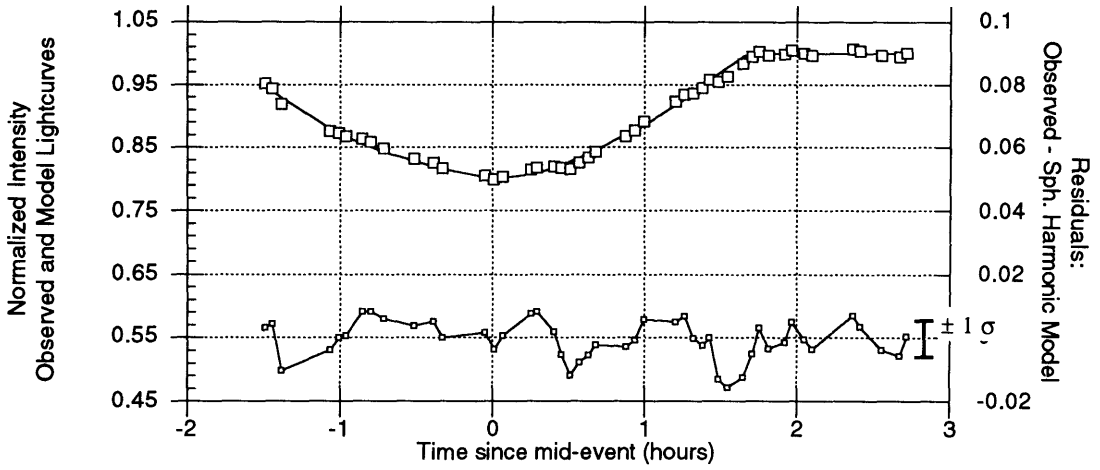

24 FEB 1990

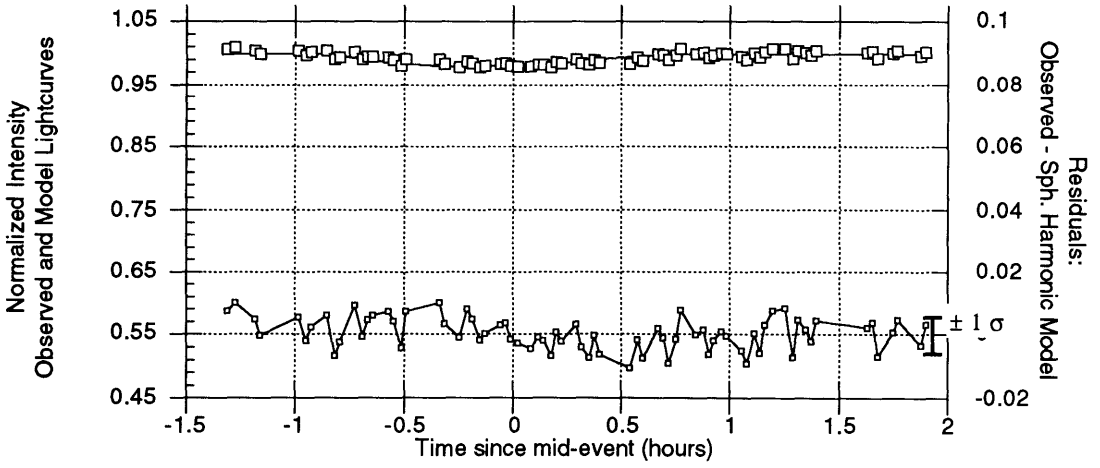

Figure 20 (a-f). Observed and Model Lightcurves with residuals

F. Comparison to the MEM Map

Marc Buie kindly sent us a copy of his MEM map before its publication in *Icarus* so that we could compare our maps to it. Figure 21 shows the sub-Charon hemispheres of the spherical harmonic map and the MEM map.

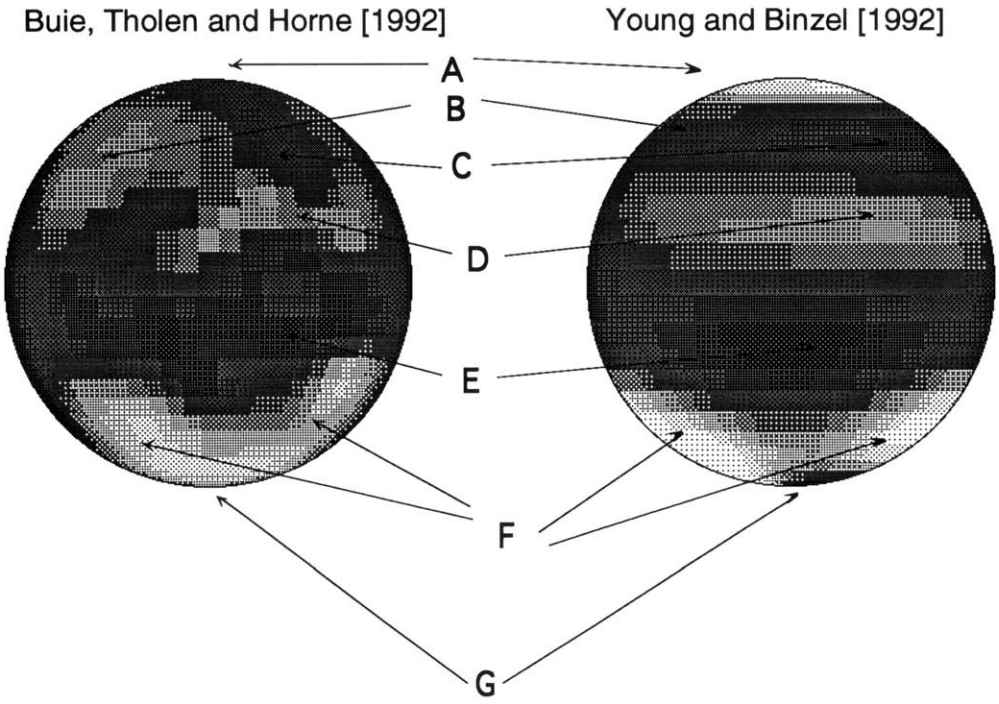

Figure 21. A comparison of sub-Charon hemispheres (zero longitude at the center of the maps) between the MEM map [Buie et al., 1992] and the spherical harmonic map [Young and Binzel, 1992]. The MEM map is in bidirectional reflectances as defined in Eq. (1), and the spherical harmonic map is in normal reflectances. The gray scales are 0 to 0.2 in the MEM case and 0 to 1.0 in the spherical harmonic case.

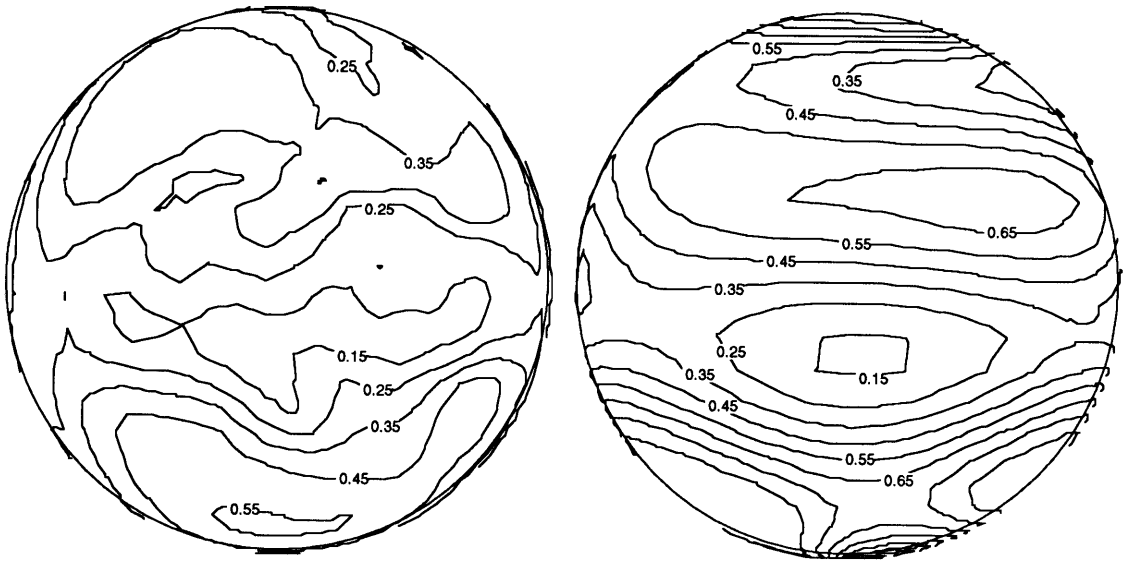

Buie, Tholen and Horne [1992] Young and Binzel [1992]

Figure 22 A contour plot version of Fig. 21. This figure compares the MEM map of Buie et al. (left) to the spherical harmonic map of Young and Binzel. Unlike Fig. 21, the bidirectional reflectances of the MEM map have been scaled by a factor of π to allow a direct comparison with a normal reflectance map. See Appendix E for a discussion of the relative scaling of bidirectional and normal reflectances.

The bidirectional reflectances (left) in Figure 21 are generated from the single scattering albedo map of Buie et al. [1992], using their values for the phase coefficient and packing parameter (P(0) = 3.0 and h = 0.3) and assuming an orbital geometry such that the subsolar and sub-Earth points both lie on the equator and the sub-Charon longitude (i.e., the sun, Earth, Charon and Pluto are in syzygy). The MEM map and the spherical harmonic map are in good agreement, especially considering that they are based on independent data sets and use different reconstruction algorithms. Both maps show a bright south polar cap with similar upside-down crescent shape (**F**), as well as a dark latitude feature (**E**) adjacent to the south polar cap, a bright region (**D**) just north of the equator, and a dark region (**C**) further north. Our northern dark feature extends to the west of the sub-Charon longitude, but the MEM map has a bright region (**B**) there. The other major differences occur at the poles: we have a bright north polar tip (**A**) which may not be significant [see section E], and a dark southern tip (**G**) that probably is significant. Neither of these extreme polar features is seen in the MEM map. The northern feature is not likely to be seen in many other maps, since it requires a lightcurve from 1985 to resolve a latitude feature that far to the north. Most groups do not have access to a 1985 lightcurve, and our 1985 lightcurve is the noisiest in our data set. The south polar tip is resolved from 1990 events, which both groups have, and it

represents an unresolved conflict. Except for the south polar tip (**G**) and the northwest feature (**B**), both maps are in excellent agreement.

G. Recap and Discussion

The pre-mutual event maps (the SHELF Model and the Two Spot Model) are based solely on rotation lightcurves. Both maps find a large, bright north polar cap and a smaller south polar cap, in direct conflict with the Eleven Panel Map and other mutual event-based maps. Rotation lightcurves by themselves do a poor job of constraining features in latitude, hence the difficulty of the SHELF and Two Spot Models in constraining the extent of the polar features.

Because Pluto's north pole was in constant shade during the approach to perihelion, we had expected it to be brightened with newly deposited frost. The results of our Eleven Panel Map and Spherical Harmonic Map showed instead that the south pole was the brightest region of the planet, and the north pole lacked a similar large bright feature. These results are particularly compelling in light of the close agreement between the MEM Map and the Spherical Harmonic Map, two maps based on completely independent data sets and calculated from different reconstruction algorithms. Both of these maps include the following features:

- A bright south pole area, normal reflectances ranging from 0.8 to 1.0.
- A dark region adjacent to the south polar cap, normal reflectances less than 0.2.
- A bright region just north of the equator, normal reflectances of 0.8 to 1.0.
- A dark region or band at higher northern latitudes, normal reflectances between 0.2 and 0.4.

These are the major findings of our Spherical Harmonic, Polynomial and Finite Element Maps. Each one prompts some speculation and perhaps even an explanation.

The bright south polar feature has been in constant sunlight during Pluto's approach to perihelion. As the most highly insolated part of the planet, we might expect it to have built up a layer of dark residues on the surface from impurities left behind by sublimating volatiles. There are at least two theories explaining the brightness of the south pole. It may be that the south pole is intrinsically bright enough to reflect most of the sunlight during the last half Pluto orbit. If only a fraction of the incident solar energy is absorbed, the south polar surface will be a relative cold spot and a site for frost condensation *despite* the fact that it is in direct sunlight. A second theory is that some highly insolated frosts get brighter instead of darker. This phenomenon has been observed on Mars, Triton, and now Pluto. Perhaps dark impurities sink into the surface instead of remaining on top. We explore the first theory but not the second in Chapters

IV and V.

The dark band adjacent to the bright south polar region is a strange feature. No other satellite or planet shows such high contrast in albedo except for Iapetus, and we think its contrast is due to its sweeping up particles in its orbit around Saturn. Pluto's surface is undoubtedly ice-covered - this conclusion is inescapable given the detection of N_2, CO and CH_4 on the surface and a 3 μbar atmosphere. The presence of bright frosts can explain Pluto's high geometric albedo, but we still need to model a mechanism for producing adjacent regions with such different albedos. In Chapters IV and V we show that Pluto will develop regions of high and low albedos if there is a very bright feature in the middle of a highly insolated part of the planet.

The lack of a bright north pole brings up two questions: why isn't it bright, and why isn't Pluto's albedo distribution symmetrical when the annual insolation is nearly symmetrical? One possible explanation for the lack of a large, bright north polar cap is that Pluto's atmosphere freezes out as Pluto approaches aphelion, and volatile transport is choked off during the post-aphelion segment of the orbit. It may be that there is a limit to how much material the atmosphere can transport (because of an upper limit on the wind speeds), and this limit is exceeded during the post-aphelion part of the orbit. If the atmosphere can easily transport volatiles during the post-perihelion quarter, but has difficulty moving volatiles in the post-aphelion quarter, Pluto's albedo distribution would be asymmetrical even though the same amount of insolation was received by the north and south hemispheres. It may be that thermal inertia of the surface also contributes to the asymmetry [Spencer and Moore, 1992]. Volatile transport in a very thin atmosphere and thermal inertia are beyond the scope of this thesis, but are likely topics for future study.

IV. The Volatile Transport Model

Recent spectroscopic observations of Pluto [Owen et al., 1992] and the 1988 stellar occultation by Pluto [Elliot and L. Young, 1992] provide a reasonable basis for implementing a volatile transport model. The reasons for looking at volatile transport are evident from the discussion in Section G of the last chapter. Briefly, we seek an explanation for the bright cap over Pluto's south pole and the lack of one over the north pole. We also seek a mechanism to explain Pluto's high contrast, the second highest observed in the solar system.

Figure 23 shows Pluto's orientation during the pre-perihelion quarter of its orbit. During that time Pluto's south pole was in constant sunlight and Pluto's north pole was in constant shadow. At perihelion Pluto's insolation distribution is temporarily like the other (low obliquity) planets in the solar system, with all of Pluto receiving sun diurnally and the equator receiving the most insolation.

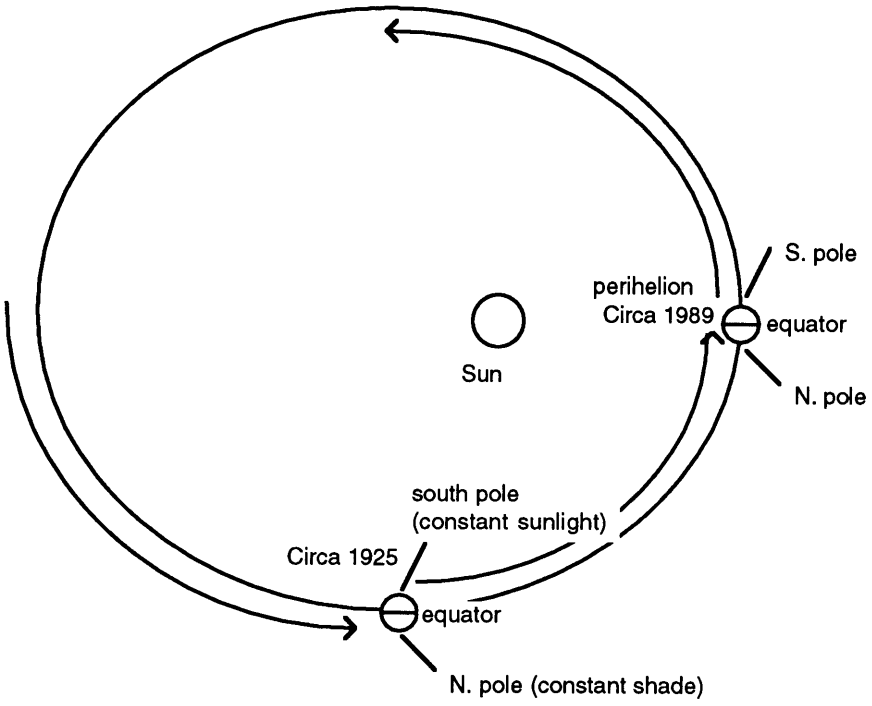

Figure 23. Pluto's orientation during its approach to perihelion.

A. Pluto's Surface

Our plan is to develop a frost model for Pluto similar to previous models for Triton [e.g., Spencer, 1990]. This model requires knowing the pressure, temperature, and composition at the surface-atmosphere interface.

The temperature and pressure of Pluto's surface are extrapolated in the analysis of the 1988 stellar occultation [Elliot and L. Young, 1992]. Their occultation lightcurve has a discontinuity at a radius of 1215 ± 11 km, representing the top of a haze layer or a steep thermal gradient. Given N_2 as the dominant constituent of the surface and the atmosphere, Elliot and L. Young find the pressure at this height is 2.38 ± 0.49 μbar and the temperature is 104.2 ± 21 K. By assuming hydrostatic equilibrium for the atmosphere below 1215 km and vapor-ice equilibrium at the surface, Elliot and L. Young extrapolate to get self-consistent surface pressures and temperatures. Their surface pressure and temperature for N_2 (β) are 3.25 ± 0.84 μbar and 35.25 ± .049 K respectively assuming a clear atmosphere with a steep thermal gradient. If one assumes a haze layer instead, the surface pressure and temperature are greater than or equal to 3.1 μbar and 35.7 K respectively.

Table 14. Summary of surface temperatures and pressures derived from model fits to the 1988 stellar occultation of Pluto, adapted from Table 9 of Elliot and L. Young [1992].

Parameter	CH_4	N_2	CO	Model
Surface Pressure (μbar)	≥1.8	≥4.5	≥4.1	**Haze, No Steep**
Surface Temperature (K)	>48.8	>35.7	>39.5	**Thermal Gradient**
Surface Pressure (μbar)	1.2±0.26	3.25±0.84	2.83±0.71	**Steep Thermal**
Surface Temperature (K)	48.04±0.45	35.25±0.37	39.02±0.38	**Gradient, No Haze**

Why assume an N_2 atmosphere? For many years methane was the only molecule identified from Pluto spectra. Recent spectra [Owen et al., 1992] have now identified N_2 and CO. There are several reasons why the detection of N_2 is evidence for N_2 being the dominant component of Pluto's surface frost and atmosphere. First, the vapor pressure of N_2 is about ten thousand times higher than that of CH_4 and over five times higher for CO. As long as there is enough N_2 to fill the atmosphere (and at around 50 cm-A, this is

not a stringent requirement), the atmosphere will be dominated by N_2. Table 15 compares the vapor pressures of CH_4, N_2, and CO at temperatures ranging from 20 to 60 K. The second argument in favor of N_2 is the spectral nature of the constituents. Because methane is so spectrally active compared to N_2, methane easily obliterates N_2's spectral features. In order for N_2 to be detected at all, methane can only be a trace constituent on Pluto's surface, with a molar fraction of less than a percent [Cruikshank, 1992]. The relative strengths of the N_2 and the CO spectral features indicate that CO is also a trace constituent, making up less than 2% of the surface frost [Cruikshank, 1992]

Table 15. Vapor pressures of various molecules at temperatures ranging from 20 - 60 K, based on data from Brown and Ziegler [1980].

Molecule	Temperature (K)	Vapor Pressure (μbar)
CH_4	20	1.62e-15
	30	4.31e-07
	40	7.89e-03
	50	2.94e+00
	60	1.53e+02
N_2	20	2.86e-08
	30	4.65e-02
	40	5.78e+01
	50	3.96e+03
	60	6.33e+04
CO	20	9.94e-11
	30	2.71e-03
	40	1.02e+01
	50	1.18e+03
	60	2.56e+04

Trafton [1990] has looked in depth at a two component model for Pluto's atmosphere, using methane and N_2 as the components. The presence of methane can affect the surface pressure of the N_2 atmosphere. Methane and N_2 form a true solid solution, meaning that molecules of methane actually take the place of N_2 molecules and vice-versa. The partial pressures of each gas can be estimated from Raoult's law, an approximation which is good to within 50% for the N_2- CH_4 case [Lunine, 1992]. (Raoult's law is a much better approximation for the N_2-CO case.) Raoult's law is

$$p_i = X_i P_i \tag{21}$$

where p_i is the partial pressure of the i^{th} gas,
X_i is the mole fraction in the solid solution, and

P_i is the vapor pressure over pure ice of the i^{th} component.

Even if Pluto's solid surface had an improbably high fraction of methane, say 50%, the partial pressure due to methane would still be less than a ten thousandth of the partial pressure due to N_2. But Trafton points out that if Pluto's volatile reservoir (the gases that sublimate and recondense every Pluto year) has even a trace of methane (a molar fraction of 0.002 or more in his example), then the molar fraction of CH_4 on the surface will be over 92%. The enhancement of the surface methane concentration is due to the fact that N_2's vapor pressure is so much higher than methane's, presumably leaving a CH_4 residue after many sublimation – condensation cycles. Could Pluto's atmosphere be primarily N_2, but its surface be mostly methane? We don't believe so, for the following reasons: First, Pluto's atmosphere by itself is too tenuous to be responsible for N_2 spectral features, so the nitrogen features must come from surface frost. Second, as stated before, methane's opacity is so much greater than N_2's that methane can only be a minor component of the surface, or we would not see an N_2 feature in Pluto's spectrum. Third, methane's spectral features are shifted by roughly 18 wavenumbers in a way consistent with methane being frozen in solid N_2 [Cruikshank, 1992].

The arguments against a substantial CO presence in the surface frost are similar. The main evidence against CO is in the relative strengths of the spectral lines of CO and N_2 as detected by Owen et al. [1992]. While interpreting planetary spectra is a complicated business, Dale Cruikshank has communicated to me that the surface frost is likely to be over 90% nitrogen and less than 2% CO or CH_4. The interpretation and modeling of Plutonian spectra is work in progress.

At the extremely low pressures of Pluto's surface, solid nitrogen can form two possible crystals; α nitrogen (a cubic crystal) and β nitrogen (hexagonal close packed). The transition from β to α takes place at 35.61 K [Scott, 1976], which is nearly the surface temperature found by Elliot and L. Young's extrapolation [1992]. Since the stellar occultation occurred in 1988, when Pluto was presumably near its warmest temperature, it seems likely that Pluto's surface would be covered with α nitrogen during most of its orbit. We wondered if the latent heat of transformation from α to β nitrogen could be important in governing the surface temperature. A rough calculation using the Clausius-Clapeyron equation [Moore, 1962] yields an estimate of λ, the heat of transformation.

$$\frac{dP}{dT} = \frac{\lambda}{T \Delta \overline{V}} \tag{22}$$

dP/dT is the pressure-temperature slope along the α–β phase boundary,
T is 35.6 K, and
$\Delta\nabla$ (Change in volume) is 0.8% [Scott, 1976].

From Figure 2 in Scott (which shows the phase diagram of solid N_2 on the P-T plane) we estimate that dP/dT is about 227 x 10^6 μbar/K. We solve for $\lambda \approx 1 \times 10^8$ ergs/g. This is roughly one twenty-fifth of the latent heat of sublimation, which is 2.54 x 10^9 ergs/g. We will therefore ignore the latent heat of transformation between the α and β solid phases, although the fact that Pluto's surface temperature may coincide with the transition temperature suggests that the latent heat of this transition may play a role. Perhaps the transition from β to α nitrogen can govern the surface temperature provided it is already close to the transition temperature of 35.6 K. The effect of the α–β transition is a topic for future study.

B. The Triton Model: A Globally Uniform Atmosphere

The Triton model assumes a uniform temperature over the volatile-covered portion of a planet. The temperature on any planet with little or no atmosphere is primarily governed by insolation and thermal radiation. In the absence of surface volatiles, these two effects lead to a diurnal temperature cycle, perhaps limited by the thermal inertia of the surface. If volatiles are present, there is a much more substantial governing mechanism than thermal inertia for limiting the amplitude of diurnal temperature fluctuations. We assume that volatiles are available and in vapor-ice equilibrium over Pluto's entire surface, having no information to the contrary[1].

The heat of transformation from a solid to a gas (or vice-versa) always opposes any change in Pluto's temperature. As a surface element on Pluto rotates from sunlight to shadow, the atmosphere cools and condenses. The heat of condensation opposes the cooling of the surface. Conversely, when the surface element rotates from darkness into

[1]How would one detect bare ground on Pluto? A few possible schemes include

• Look for evidence of 60°K "Hot Spots" on Pluto with 20- 60μ infrared detectors. Since bare ground is not cooled by sublimation, the subsolar point would have an equilibrium temperature of 60°K. It may be possible to detect the Rayleigh-Jeans part of a 60°K blackbody spectra directly, since a hot spot at 60°K may outshine the rest of the planet at 35°K. Alternatively, it may be possible to model the thermal spectrum of Pluto as two superimposed blackbodies, similar to Io. Both of these tasks are well suited to an orbiting IR detector such as ISO.

• Construct albedo maps in other wavelengths. A K-band map, for example, should tell us the location of methane frost, since 2.2μ is a strong absorption feature of methane. If a region on Pluto is bright in the V or B-bands but dark in the K-band, then it is likely that the region is covered with bright methane frost.

sunlight, the molecules sublimate from the surface, helping to maintain a cool surface despite the increased insolation. At every point on Pluto's surface we can solve the heat balance equation by requiring that the net heat flux on any point on the surface will try to remain zero as long as there are volatiles present to govern the process. Since volatile transport only redistributes the heat flux over the planet, the global temperature depends on the total amount of heat coming into the planet and the total amount leaving due to thermal radiation. In the steady state these two are equal.

$$\varepsilon\sigma T_v^4(4\pi R^2) = Flux_{sun}\,(1 - A)\,\pi R^2 \tag{23}$$

where R = Pluto's radius,

A = the average Bond albedo of Pluto,

ε = emissivity of the frost,

T = global temperature, and

σ = Stefan-Boltzmann constant = 5.66956×10^{-5} erg/cm^{2}deg^{4}sec.

If we plug in an albedo of 0.75 and an emissivity of 1.0, we solve for a global temperature of 35.8 K. Lower emissivity values will raise that temperature, as will lower albedos. Pluto's average geometric albedo is 0.5 [Binzel and Mulholland, 1984]. The Bond albedo, A, and the geometric albedo, p, are related by a phase integral, q.

$$A = pq \tag{24}$$

We do not have phase integrals for Pluto, but we do for Triton. Voyager results determined that q = 1.2 and 1.5 for Voyager's green and violet filters respectively [Smith et al., 1989]. Although our mutual event maps are based on lightcurves using Johnson B filters, we use a value of q = 1.5. The cold surface temperature (35.25 K) of the stellar occultation results requires that A = 0.75.

Insolation and thermal radiation do not balance each other locally, only globally. The local heat balance equation requires some sublimation or condensation to occur to make up the difference between solar flux and thermal radiation.

$$\frac{L_{sun}\,(\hat{n}\cdot\hat{p})\,(1 - A)}{4\pi r^2} = \varepsilon\sigma T^4 + H\dot{E} \tag{25}$$

where $\hat{n}$ is the normal to a given point on the surface,

$\hat{p}$ is the unit vector that points from Pluto to the sun,

H = the latent heat of the volatile,

$\dot{E}$ = the mass sublimation rate in gm/sec.

L_{sun} = 3.826x10^{33} erg/cm^{2}sec (luminosity of the sun),
r = distance to Pluto, 4.5x10^{14} cm at perihelion

We solve for $\dot{E}$, the only unknown in this equation. The local heat balance equation (25) gives us the condensation and sublimation rates. We can step through Pluto's orbit at small intervals and find the integrated frost deposited on or sublimated from the surface.

Highly insolated regions of Pluto will lose mass, while shaded regions will gain mass. Is the total mass accumulation zero? We can calculate the global mass accumulation by rearranging Equation (25) and integrating over the entire sphere.

$$\int_{\phi}\int_{\theta}\left(\frac{L_{sun}\,(\hat{n}\cdot\hat{p})\,(1-A)}{4\pi r^2} - \varepsilon\sigma T^4\right) d\theta\, d\phi = \int_{\phi}\int_{\theta} H\dot{E}(\theta,\phi)\, d\theta\, d\phi \qquad (26)$$

where θ and ϕ are latitude and longitude.

The left hand side is the net planet-wide difference between the heat input rate from the sun and the heat loss rate due to thermal radiation. We require these two heating rates to balance in Equation (23), so the left hand side of Equation (26) must be zero. There is no net mass loss or gain from the surface in this model.

C. The Subsonic Regime

Near perihelion, Pluto's global temperature is a constant. The vapor pressure of N_2 is an extremely steep function of temperature. There simply cannot be a significant difference in temperature over Pluto's surface, because if there were, a huge pressure gradient would be the result. There is a constant flow from the highly insolated to the less insolated parts of the planet. The observational evidence for a globally uniform atmosphere comes from the 1988 stellar occultation. The ingress and egress portions of the lightcurves are mirror images of each other, despite the fact that one probes the atmosphere above the morning terminator, and the other probes the above evening terminator. If the planet could heat up locally while exposed to the sun, then the two parts of the lightcurve would be different.

What are the limits of the global temperature model? Presumably when excessive flow is required to balance an ensuing pressure gradient, the dark side of the planet will end up with a thinner, colder atmosphere than the sunlit side. The threshold for

"excessive flow" is when the required winds are supersonic. The winds from the subsolar point may be able to go faster than the speed of sound (up to $v_{max} = \sqrt{2C_pT_0}$, where T_0 is the subsolar surface temperature [Ingersoll et al., 1985]), but we will only use the global temperature model in the subsonic regime.

As Pluto leaves the sun, its atmosphere cools and the number density decreases. The pressure gradients from sunlit to shaded areas are still high, however, because the vapor pressure is such a steep function of temperature. To balance these gradients the atmosphere needs to maintain the same flux of gas; if the density decreases the flow velocities must increase. We can estimate the horizontal wind speeds by setting the sublimation rate equal to the divergence of the horizontal flux.

$$\dot{E} = \nabla\cdot\left(\frac{P_s}{g}\,\mathbf{v}\right) \tag{27}$$

where P_s is the surface pressure,
g is the gravitational acceleration, and
v is the velocity.

Equation (27) is the result of vertically integrating the conservation of mass equation,

$$\frac{\partial\rho}{\partial t} = \nabla\cdot(\rho\,\mathbf{v}) \tag{28}$$

where ρ is the density and t is time.

Remember that we have already solved for $\dot{E}$ using Eq. (25), so we should be able to solve for **v** from Eq. (27). One caveat: we are assuming that the velocity is not a function of height, which it undoubtedly is. If the horizontal wind is confined to an Ekman boundary layer, for example, then the surface speeds could be greater. Nevertheless, let us proceed with this assumption to get a first order answer.

If we ignore Pluto's relatively sedate rotation of 6.38 days, then the subsolar flow problem is symmetric about the subsolar point.

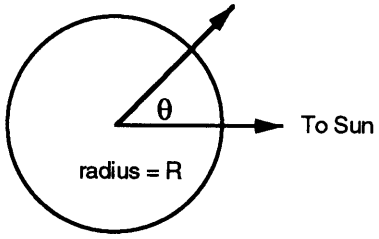

Figure 24. θ is the angle from the subsolar point measured from the center of Pluto's sphere.

Let T, P_s, $\dot{E}$, and **v** be functions of θ, the angle from the subsolar point measured at the center of the planet. Integrating both sides of Eq. (27) gives us a simple interpretation for the conservation of mass: in the symmetrical case, the mass flowing through the circumference of a circle centered on the subsolar point is equal to the integrated mass flux from the surface within that circle.

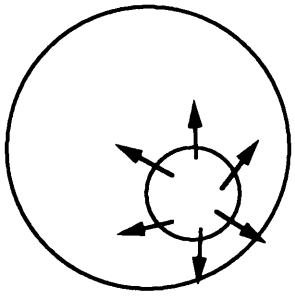

Figure 25. Mass flux through a circle concentric about the subsolar point must equal the integrated mass leaving the surface from within the circle.

$$\left(\frac{P_s \mathbf{v}}{g}\right) 2\pi R \sin\theta = \int_0^{\theta} \dot{E}\, dA = \int_0^{\theta} \dot{E}\, 2\pi R^2 \sin\theta\, d\theta \tag{29}$$

where R is Pluto's radius and dA is an thin, concentric ring area element.

The global temperature (from Eq. (23)) is

$$T = \left[\frac{L_{sun}(1 - A)}{16\pi d^2 \varepsilon \sigma}\right]^{1/4} \tag{30}$$

The insolation on the day side is a function of θ.

$$S(\theta) = S_0 \cos\theta, \quad S_0 = \frac{L_{sun}(1 - A)}{4\pi d^2} \tag{31}$$

where $S(\theta)$ is the insolation, and S_0 is the insolation at the subsolar point,

If we solve for the sublimation rate, $\dot{E}$, in Eq. (25) and substitute for the insolation and the global temperature, we get an expression for $\dot{E}$ in terms of θ.

$$\dot{E} = \frac{1}{H}\left[S_0\cos\theta - \varepsilon\sigma T^4\right] = \frac{S_0(\cos\theta - 0.25)}{H} \quad \text{for the sunlit hemisphere}$$

and (32)

$$\dot{E} = \frac{1}{H}\left[-\varepsilon\sigma T^4\right] = \frac{-S_0}{4H} \quad \text{for the dark hemisphere.}$$

Now we can substitute for $\dot{E}$ in Eq. (29) and integrate the right side with respect to θ. For now we'll integrate up to the limb, because we're interested in the maximum of $v(\theta)$, which occurs on the day side.

$$\left(\frac{P_s v}{g}\right) 2\pi R\sin\theta = \int_0^\theta \dot{E}\, dA = \int_0^\theta \frac{S_0(\cos\theta - 0.25)}{H}\, 2\pi R^2 \sin\theta\, d\theta$$

which becomes

$$\left(\frac{HP_s v}{gS_0 R}\right)\sin\theta = \int_0^\theta (\cos\theta - 0.25)\sin\theta\, d\theta \tag{33}$$

this integral is

$$\left(\frac{HP_s v}{gS_0 R}\right)\sin\theta = \int_0^\theta (\cos\theta - 0.25)\sin\theta\, d\theta = \frac{1}{2}\left[\sin^2\theta + \frac{\cos\theta}{2}\right]_0^\theta$$

or

$$\left(\frac{HP_s v}{gS_0 R}\right)\sin\theta = \frac{1}{2}\left(\sin^2\theta + \frac{\cos\theta - 1}{2}\right) \tag{34}$$

Solving for $v(\theta)$ gives us

$$v(\theta) = \frac{gS_0 R}{2HP_s}\left(\sin\theta + \frac{\cos\theta - 1}{2\sin\theta}\right) \tag{35}$$

on the daylight side, for $\theta = 0$ to $\pi/2$. On the night side we get

$$v = \frac{gS_0R}{4HP_s}\left(1 + \frac{\cos\theta}{\sin\theta}\right) \text{ for } \pi > \theta > \pi/2 \tag{36}$$

Since we want to know v's maximum value, we differentiate v(θ) with respect to θ and find a local maximum. By differentiating Eq. (35) we find a local maximum at θ = 68.53°, at which point the maximum velocity is

$$v_{max} = 0.29\,\frac{gS_0R}{HP_s} \tag{37}$$

Table 16. Maximum wind velocities as a function of time for N_2 (β) and A = 0.77.

YEAR	Temp (K)	P (μbar)	V_{max} (cm/sec)
1980	35.09	2.92e+00	9.80e+01
1990	35.40	3.61e+00	8.19e+01
2000	35.06	2.86e+00	9.96e+01
2010	34.21	1.56e+00	1.65e+02
2020	33.11	6.77e-01	3.34e+02
2030	31.96	2.68e-01	7.32e+02
2040	30.90	1.07e-01	1.60e+03
2050	29.99	4.59e-02	3.31e+03
2060	29.22	2.18e-02	6.28e+03
2070	28.61	1.16e-02	1.08e+04
2080	28.14	7.02e-03	1.67e+04
2090	27.79	4.81e-03	2.32e+04
2100	27.57	3.74e-03	2.89e+04
2110	27.45	3.30e-03	3.23e+04
2120	27.46	3.30e-03	3.23e+04
2130	27.57	3.74e-03	2.89e+04
2140	27.79	4.80e-03	2.32e+04
2150	28.13	7.00e-03	1.68e+04
2160	28.61	1.16e-02	1.08e+04
2170	29.22	2.17e-02	6.30e+03
2180	29.98	4.56e-02	3.32e+03
2190	30.90	1.06e-01	1.61e+03
2200	31.95	2.66e-01	7.36e+02
2210	33.10	6.73e-01	3.35e+02
2220	34.20	1.55e+00	1.66e+02

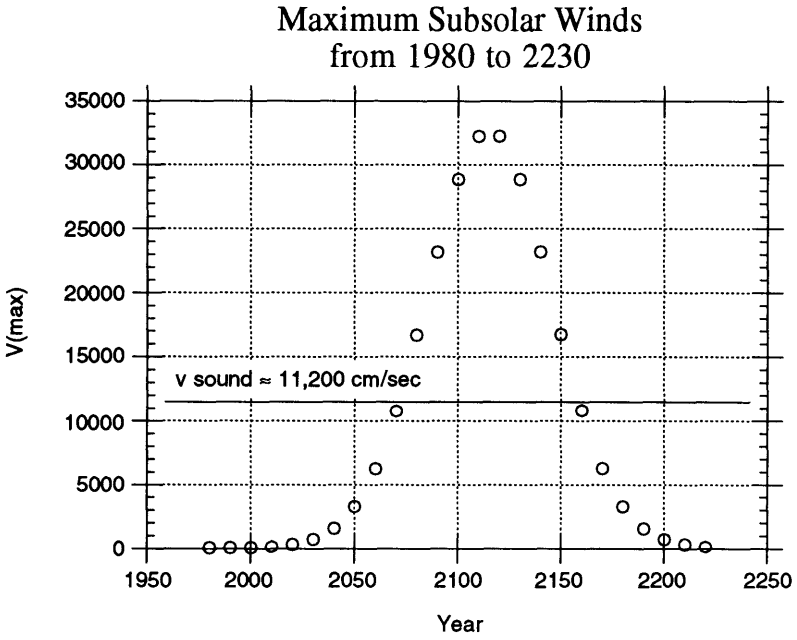

Figure 26. Predicting supersonic winds from 2070 to 2160.

$v_{sound} = (\gamma R^* T)^{1/2}$ = around 11,200 cm/sec. (Remember that $R^* = R/\mu$.) The subsolar flow in this case is supersonic from 2070 through 2160, a period of about 90 years.

How robust is the determination of the supersonic crossover year? In Eq. (37) v_{max} is inversely proportional to the surface pressure, which in turn is a sensitive function of temperature. Small changes in albedo, for example, could change the global temperature by a fraction of a degree, resulting in shifts of decades in the onset of supersonic winds. Figure 27 plots the year of the predicted crossover to supersonic winds as a function of the global temperature in 1990. In each case the temperature for the rest of the orbit is determined by scaling the insolation by the inverse square law.

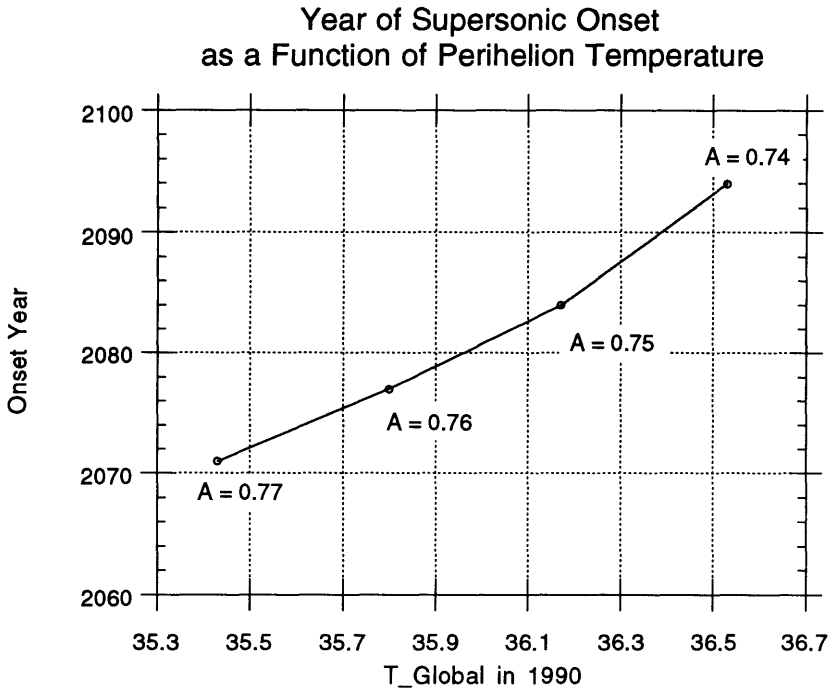

Figure 27. The predicted onset of supersonic winds is extremely sensitive to the global temperature. The average Bond albedos corresponding to a certain global temperature are also listed.

The time of supersonic wind onset is a sensitive function of the planetary temperature. If we assume that Pluto's average geometric albedo is 0.5, then a phase integral of 1.46 yields a Bond albedo of 0.73 (neglecting wavelength dependences). The temperature (and consequently the pressure) is high enough (about 36.8 K at perihelion) to preclude supersonic winds altogether. If the phase integral is just a little higher, say 1.48, then the Bond albedo is 0.74, and we find supersonic winds beginning in 2094. An increase of just 0.02 in the phase integral corresponds to a shift forward of about *seven years* in the predicted onset of supersonic winds.

From this analysis it is quite possible that Pluto never leaves the subsonic regime. All that is required is for the perihelion temperature to be over 36.8 K. This surface temperature is consistent with the haze model results of the 1988 stellar occultation [Elliot and L. Young, 1992], and cannot be ruled out. On the other end of the scale, we can probably rule out the onset of supersonic winds before the year 2050 because of the unlikely possibility of having perihelion surface temperatures below 35 K. The 1988 occultation gives a lower limit in the haze scenario of 35.7 K. A global temperature model with surface frost emissivities less than one and phase integrals less than 1.5 result in steady state surface temperatures over 36 K (as described in the next chapter).

V. Short Term Frost Model Predictions

We have implemented Triton-like frost model for Pluto. In this chapter we model the transport of volatiles on Pluto's surface over the next 50 years. In this section we will

- Characterize the surface temperature and pressure for the next 50 years.
- Predict albedo changes due to frost migration.
- Estimate the bulk atmospheric mass over the next 50 years. We are interested in what fraction of the atmosphere freezes out during this period.

A. Choice of Parameters

There are several unknown parameters in the Plutonian volatile transport model. When faced with a lack of data, we have tried to run the model for a range of possible case. For example, we run the model for both α and β nitrogen, since it is not clear if supercooled β nitrogen would spontaneously change to α nitrogen. Another issue is how to update the surface albedos when volatiles sublimate from or condense onto the surface. We use three updating schemes: (a) an multilayer particle model, (b) a multilayer particle model with extra-large particles, and (c) no updating at all.

The emissivity of the surface is also unknown. While it is theoretically possible to calculate ε for nitrogen frost or other substances from measurements of their optical constants, we are not sure of the molecular makeup of the frost, nor what effect the frost's porosity would have on the emissivity. We choose an emissivity of $\varepsilon = 1.0$ in order to be consistent with the extrapolated surface temperature of 35.25 K. Our best guess for the phase integral, q, comes from Voyager observations of Triton, putting q at 1.2 or 1.5 for green or violet band filters respectively. As with the emissivity, we choose $q = 1.5$ to be consistent with the cold surface temperature. At a distance of 4.5×10^{14} cm, a phase integral of $q = 1.5$ results in an average Bond albedo of 0.75 and a global temperature of 35.9 K.

Throughout the rest of this thesis we use 35.25 K as the operational value for Pluto's surface temperature. Direct observations of Pluto's blackbody spectrum may tell us the surface temperature in the near future, but in the meantime we use the 35.25 K value. Keep in mind that this value is an extrapolation from a model fit – two generations away from a direct measurement. Some of the findings are robust in the face of this assumption. For example, the fraction of Pluto's atmosphere that freezes out over the next 50 years will still be over 97%, regardless of the absolute surface pressures involved. Two results in particular are sensitve to the choice of adopted surface

temperature: the column abundance as a function of time, and the onset of supersonic winds. Figure 28 plots the column abundance as a function of temperature, and Figure 27 looks at the onset of supersonic winds as a function of the assumed surface temperature at perihelion. The migration of frost depends on the imbalance between local insolation and thermal radiation. The local variations in insolation dominate the heat imbalances, and a slight elevation in the global temperature has almost no effect on the resulting frost migration.

B. Fifty Year Projections for Temperature and Bulk Atmosphere (Bond Albedo = 0.75)

The calculation of Pluto's global temperature depends Pluto's average albedo, emissivity and Pluto's distance from the sun. As long as the surface is in vapor-ice equilibrium, this temperature determines the surface pressure. The column abundance is nearly equal to the surface pressure over the surface gravity.

$$[m] = P_s/g \tag{38}$$

where [m] = column mass,

P_s = surface pressure, and

g = surface gravity

Using 1150 km and 2 g/cm as Pluto's radius and density, we find that g = 64.2 cm/sec^2. Eq. (38) is approximate because the acceleration due to gravity is a function of height. In Appendix C we integrate the column mass as a function of height above the planet and find that the ratio between the surface pressure and the column mass is 60.1 cm/sec^2. Thus Eq. (38) underestimates the column mass by about 6%. To correct for this factor we replace g in Eq. (38) with g' = 60.1 cm/sec^2.

Table 17. Surface temperatures and pressures and column mass abundances for an N_2 atmosphere from 1990 through 2040. Bond albedo = 0.77, emissivity = 1.0.

Molecule	Year	Temperature (K)	Vapor Pressure (μbar)	Column Mass (gm/cm^2)
N_2 (β)	1990	35.40	3.61	6.01e-02
	2000	35.06	2.85	4.75e-02
	2010	34.21	1.56	2.59e-02
	2020	33.10	0.67	1.12e-02
	2030	31.96	0.26	4.40e-03
	2040	30.90	0.10	1.70e-03
N_2 (α)	1990	35.40	2.34	3.89e-02
	2000	35.06	1.75	2.92e-02
	2010	34.21	0.83	1.38e-02
	2020	33.10	0.28	4.80e-03
	2030	31.96	0.08	1.40e-03
	2040	30.90	0.02	4.00e-04

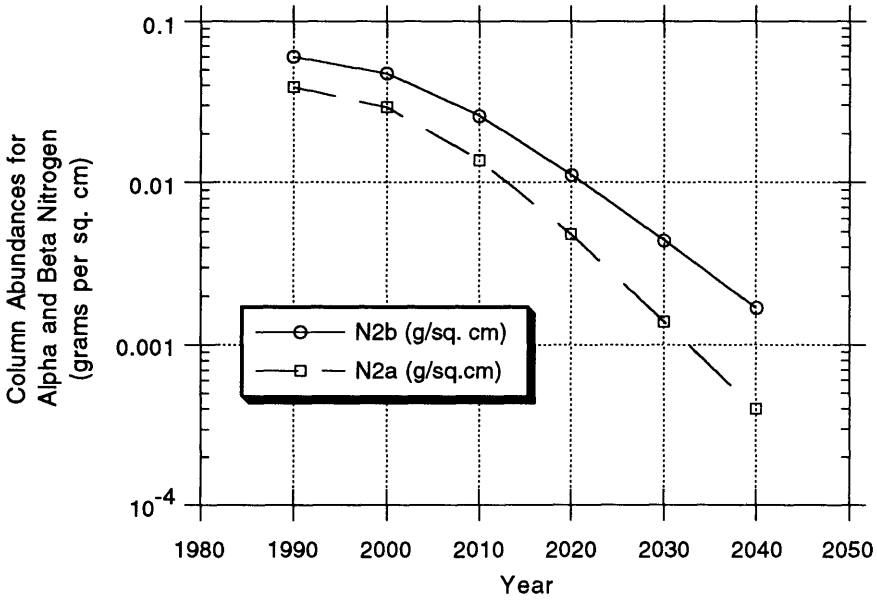

Figure 28. Column abundances of α and β nitrogen from 1990 to 2040. For both species over 97% of the atmosphere freezes out during this period.

Summary of results of the 50 year projection:

- The global temperatures do not depend on the choice of volatile. There is a 5.5 degree drop in temperature over the next 50 years.

- Substantial thinning of the Plutonian atmosphere is predicted for both nitrogen species. For N_2 (β) the atmosphere in 2040 has only 2.8% of its 1990 mass; for N_2 (α), 1.1%. (This decrease in Pluto's bulk atmosphere is not particularly sensitive to the exact value of Pluto's temperature in 1990. Even if we let Pluto's surface pressure differ by factors of 3 or 4 from the 1988 stellar occultation solutions [Elliot and L. Young, 1992], the *fractional* decrease in Pluto's bulk atmosphere from 1990 to 2040 is still about the same.)
- The drop in temperature, pressure, and other related quantities is slowest during the ten year interval from 1990 to 2000, because the solar distance changes least during this period. More dramatic (and more easily observable) changes in the bulk atmospheric parameters occur after the year 2000.

Is it possible that Pluto's surface is kept warm by the global condensation of its atmosphere? If Pluto's atmosphere were denser, it would significant retard Pluto's cooling rate in the post-perihelion segment of the orbit. Pluto's atmosphere is so thin, however, that the latent heat available from the entire atmosphere is a small fraction of the energy received from the sun or lost by thermal radiation. Suppose that Pluto has an N_2 atmosphere with a column abundance of 0.1 g/cm^2 at perihelion. If the entire atmosphere were to condense to the beta form of solid nitrogen, 2.54 x 10^9 ergs/g would be released, yielding 2.54 x 10^8 ergs/cm^2. At perihelion, the solar power striking Pluto is approximately 1500 ergs/cm^2 sec, so the energy released from the total solidification of Pluto's atmosphere is equivalent to 170,000 seconds of sunlight, or about 1.9 days of sunlight. Since Pluto's atmosphere freezes out on a timescale of decades, the latent heat from the atmosphere's long term, global condensation is negligible compared to heating by solar insolation and cooling by thermal radiation.

C. Albedo Maps and Frost Transport

We use three different albedo maps to initialize the frost transport simulation. All three maps have sub-Charon geometric albedos of 0.5. The three maps are

- A uniform map with normal reflectances of 0.5 (Map *A*),
- A latitudinally averaged map. This map is the smoothed spherical harmonic map [Chapter 3], averaged in latitude and stretched over the anti-Charon side of the planet (Map *B*), and
- A half mutual event, half latitudinally averaged map. This map is the smoothed spherical harmonic map on the sub-Charon side and its latitudinally averaged values on the anti-Charon side (Map *C*). The smoothing is preformed after assigning the average normal reflectances to the anti-Charon side to reduce the discontinuity

across the boundary of the sub-Charon and anti-Charon hemispheres.

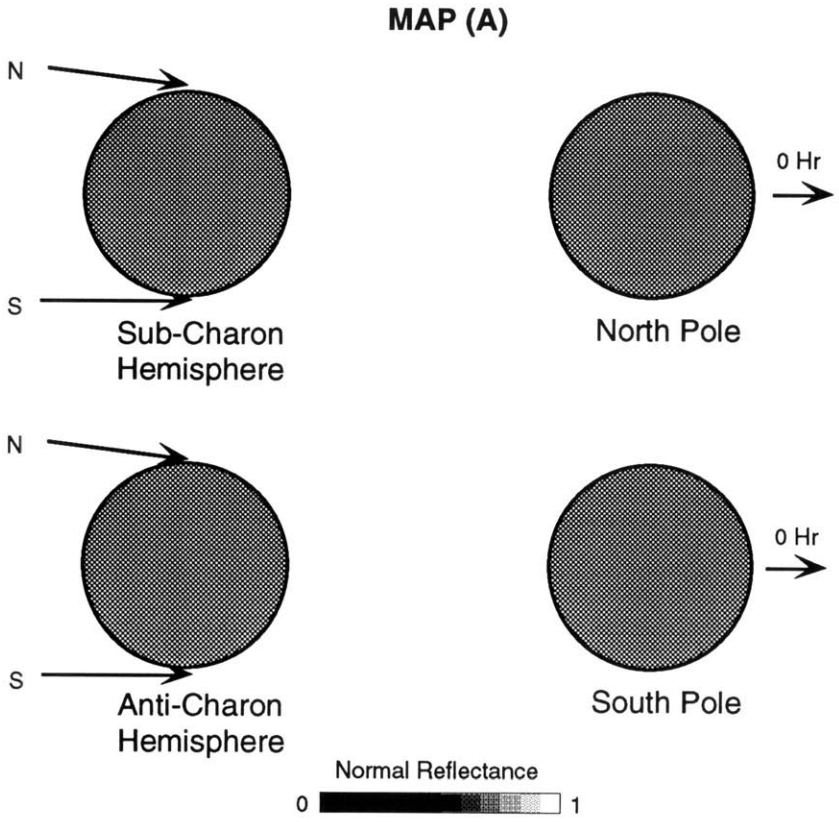

Figure 29. Map *A*, a uniform reflectance of 0.5 over the entire planet.

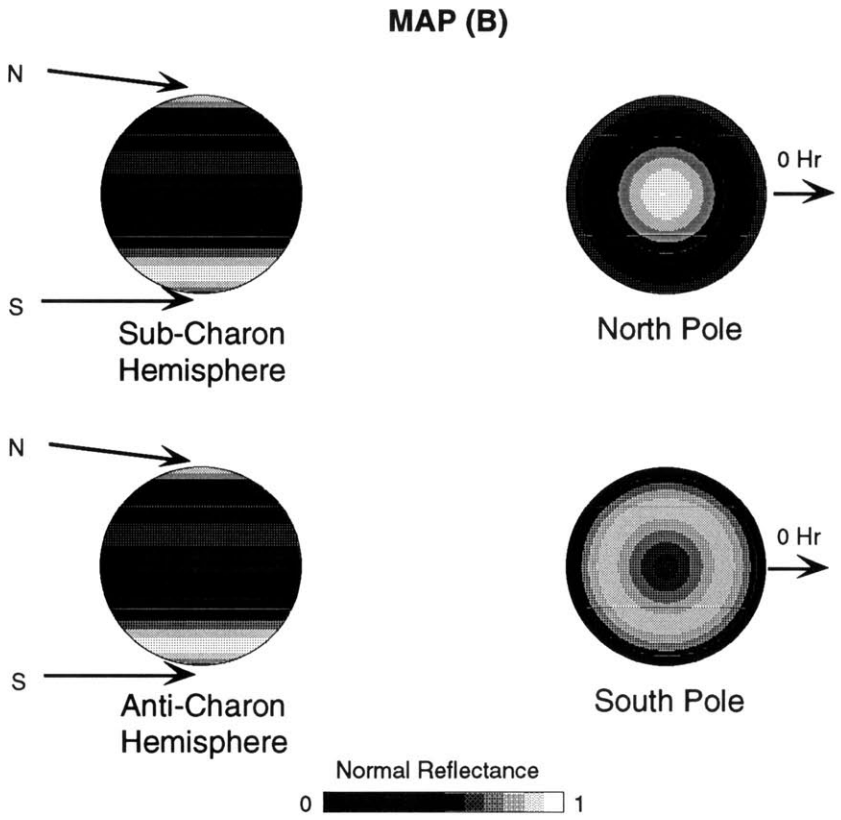

Figure 30. Map *B*, the spherical harmonic map averaged in latitude and stretched over the entire planet.

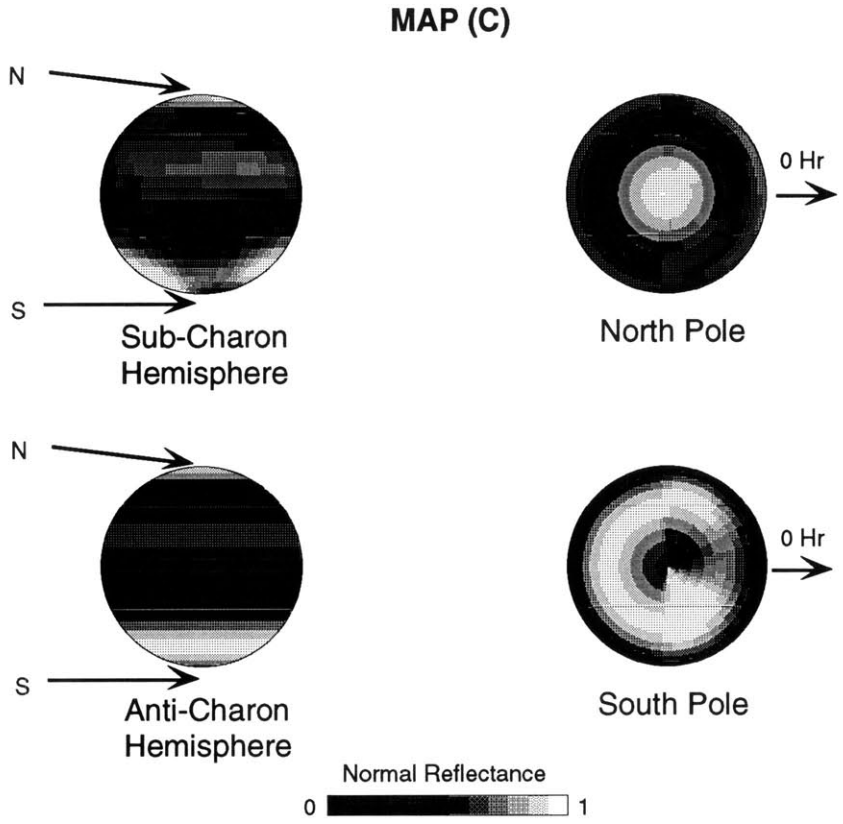

Figure 31. Map *C*, the spherical harmonic map. The anti-Charon hemisphere is filled in with the latitudinal averages from the sub-Charon side.

These maps constitute a basic sensitivity test determining how much the transport of volatiles is affected by the pre-existing albedo map. A comparison between Map *A* and Map *B* tells us if albedo variations in latitude are important, and a comparison between Map *B* and Map *C* gauges the effect of variations in longitude.

i. Modeling Frost Reflectivity

We assume that new frost is bright, and frost with other material mixed in is darker. There have been proposals that nitrogen frost gets *brighter* as it receives insolation [Spencer, 1990]. Spencer uses an empirical rule to describe the brightening of highly insolated N_2 on Triton. We choose not to use this rule because it may supplant a brightening mechanism effected by the transport of volatiles. Without further evidence, we will assume that new frost on Pluto is bright and that dark material is the result of polymerization of CH_4 by UV radiation, transforming methane into substances that grow darker and redder as their molecules grow longer [Stern et al, 1988]. The two key questions are: how bright is new frost and how does the brightness of frost change as

dark material is mixed in?

The recent maps by Buie et al. [1992], Burwitz et al. [1991] and Young [Chapter 3] show large regions of the planet with normal reflectances between 0.90 and 1.0. Other evidence for bright frost comes from the Voyager 2 images of Triton – the brightest regions on Triton have normal reflectances of 0.95 [Smith et al, 1989]. We attribute a reflectance of 0.95 to the pure frost.

The frost albedo decreases dramatically with only a small fraction of dark material mixed in [Clarke et al, 1986]. We model the absorption of ice-polymer mixtures on the behavior of mixtures of water ice and charcoal.

Table 18. Reflectances of water ice-charcoal mixtures at 6500Å [Clark et al., 1986].

Percentage Charcoal by weight	Temperature (Kelvin)	Observed Reflectance
0.0	151	0.45
0.03	142	0.225
0.1	122	0.15
1.0	128	0.15
10.0	125	0.095

We know that a small fraction of impurities can have a strong effect on the albedo [Clarke et al., 1986]. We model the surface frost as a stack of single-particle thick layers. Each layer has a transmittance, T, and a reflectance, R. One advantage of this type of model is its flexibility: R and T can accommodate many physical processes. We seek values of R and T that can duplicate the results of Clarke et at [1986] in Table 18. We also want to relate R and T to the fractional amount of impurities in each frost layer.

The stack of layers has a global reflectance different from a single layer's reflectance. This overall reflectance may be due to reflections several layers below the surface. The expression for the surface reflectance is derived in Appendix E.

$$A = \frac{1 + R^2 - T^2 - \sqrt{R^4 + T^4 - 2(R^2 + T^2 + R^2T^2) + 1}}{2R} \tag{39}$$

where A = surface albedo,

R = reflectance of a single layer, and

T = transmittance of a single layer.

What are R and T for a pure frost layer (A = 0.95)? There are several reasons why R might be small for a single layer:

- There may be lots of empty space in a single layer.

- The frost particles may be clear with very low absorption. They may only reflect 5 - 10% at each interface, and may transmit 90 - 95%.
- Nitrogen frost may anneal efficiently into clear layers or large clear particles [Eluszkiewicz, 1991].
- An tiny increase in absorption has a large effect when much of the reflected light comes from below the surface. This only happens when R is small.

On the other hand, there are reasons why R might be large:

- Most planetary surfaces (such as the lunar regolith) have phase functions that are strongly backscattering. This is the result of internal scattering within the particles, which is characterized by larger R values.
- The results of Clarke et al. [1986] may be skewed by relative particle sizes. If the impurity is of fine grain relative to the frost, it will absorb a disproportionate amount of light. We assume that frost and impurities have the same grain size. This eases the need for a very steep albedo dependency on the fraction of impurities.

We plot four cases in which R takes on values of 0.05, 0.25, 0.5, and 0.75. The transmittance varies from zero to (1 - R).

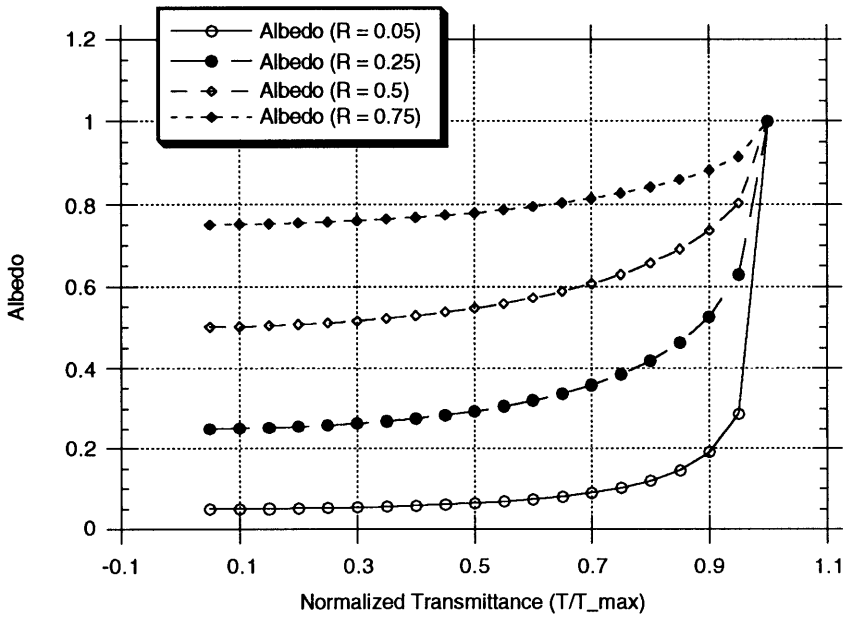

Figure 32. The albedo as a function of the normalized transmittance for four different cases: R = 0.05, 0.25, 0.5, and 0.75. Notice that the smallest single layer reflectivity, R = 0.05, results in a curve that looks most like the data of Clarke et al. [1986].

If the single layer absorption is proportional to the fraction of impurities in the frost, then the R = 0.05 curve best duplicates the results of Clarke et al. [1986]. This result

supports a small value of R for the single layer reflectivity. Somewhat arbitrarily we choose a single layer reflectivity of R = 0.05, and let the transmittance be a function of the amount of dark impurities present in the nitrogen frost. One boundary condition is that pure frost should have a net reflectivity of 0.95. A second condition is that the net reflectivity should asymptotically approach 0.2 as the level of impurities increases. A third condition is that a very small level of impurities should be able to change the net reflectivity from 0.95 to 0.2. Notice that we are forcing the frost to be the agent responsible for a wide range of albedos, as opposed to modeling part of the planet by exposed silicates (for example). The range of values for the transmittance are determined from the conditions that R = 0.05, the maximum reflectivity is 0.95, and the minimum reflectivity is 0.2. The transmittance is constrained to the range 0.94993 > T > 0.865. A simple empirical function for R and T as functions of the molar fraction of impurities present is

$$R = 0.05$$

$$T = 0.94993 - 0.08493\,F \tag{40}$$

where F = the fraction of particles that are dark impurities.

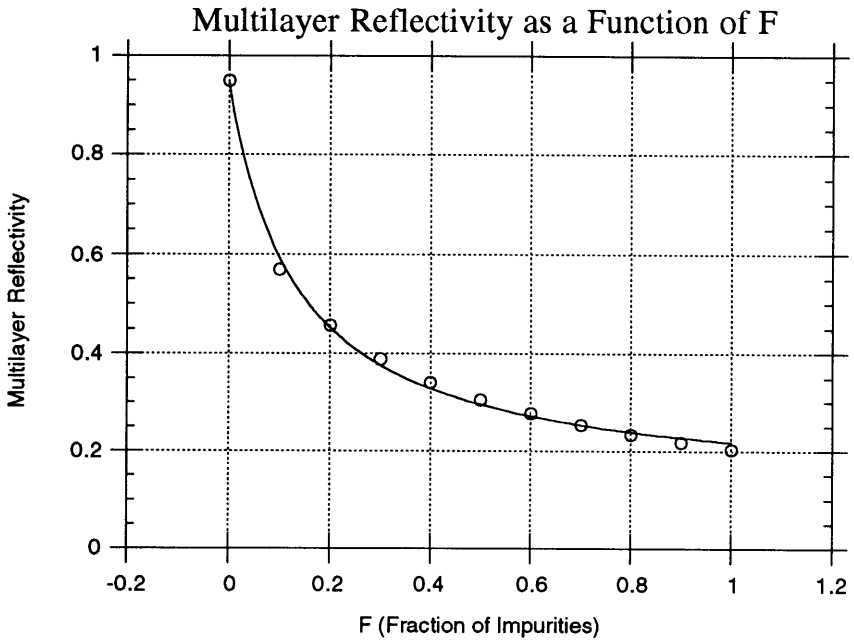

Figure 33. The multilayer reflectivity as a function of F, the fraction of impurities. Notice that the reflectivity spans a range from 0.2 to 0.95. The solid line is a rational polynomial we use as a simple approximation for the normal reflectivity as a function of F.

The multilayer reflectivity is a complicated function of F. We need to be able to estimate the fraction of dark material from the albedo, as well as generating the albedo given a certain mixing ratio. We use a simple rational polynomial to model the albedo as a function of F.

$$\text{Normal Reflectivity} = r_n = 0.12 + 0.11156 / (0.13525 + F) \quad (41)$$

The inverse of (41) is

$$F = -0.13525 + 0.11156 / (r_n - 0.12) \quad (42)$$

Equations (41) and (42) let us determine the surface mixing ratio from the albedo or estimate an albedo from the mixing ratio. We will use Eq. (41) to update the reflectance when frost sublimates or condenses on the surface and changes the mixing ratio.

ii. Multi-Component Frosts

The albedo changes when a layer of new frost is deposited or when a layer of dark material collects on top of the original frost layer. This situation cannot be modeled with a stack of identical thin layers, because the top layers have different R and T parameters from the underlying frost. We use a two-component model, where the top component has a finite thickness *h* and reflectance/transmittance values of R_1 and T_1. The underlying frost is considered infinite in extent and has reflectance/transmittance values of R_2 and T_2.

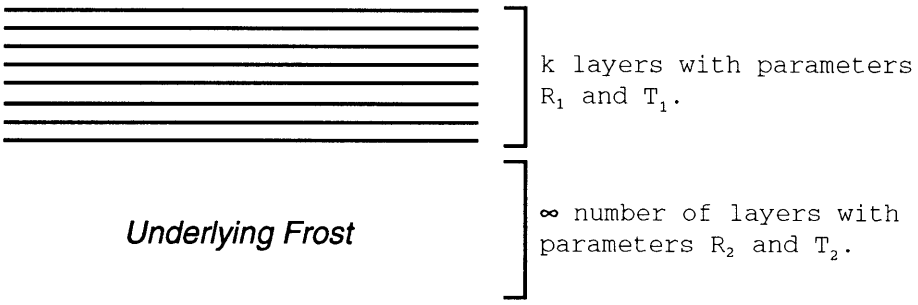

Figure 34. Modeling the surface after condensation or sublimation of frost. The top layers will have different transmittance and reflectance than the underlying frost layers.

Since we have modeled each layer as being one particle-diameter in height, the number of layers in the upper stack is

$$k = h/d \quad (43)$$

where k = number of layers in the upper frost component,
h = thickness of the upper frost component, and

d = particle diameter.

The normal reflectivity of a two-component frost with an h-cm thick layer on top is

$$r_n = \frac{\lambda_1^k - \lambda_2^k}{s_1\lambda_1^k - t_1\lambda_2^k} + \left(\frac{s_1 - t_1}{s_1\lambda_1^k - t_1\lambda_2^k}\right)^2 \frac{1}{u_1} \tag{44}$$

where

$$\lambda_1 = \frac{1 - R_1^2 + T_1^2 + \sqrt{R_1^4 + T_1^4 - 2(R_1^2 + T_1^2 + R_1^2T_1^2) + 1}}{2T_1},$$

$$\lambda_2 = \frac{1 - R_1^2 + T_1^2 - \sqrt{R_1^4 + T_1^4 - 2(R_1^2 + T_1^2 + R_1^2T_1^2) + 1}}{2T_1},$$

$$s_1 = \frac{2R_1}{1 + R_1^2 - T_1^2 - \sqrt{R_1^4 + T_1^4 - 2\left(R_1^2 + T_1^2 + R_1^2T_1^2\right) + 1}},$$

$$t_1 = \frac{2R_1}{1 + R_1^2 - T_1^2 + \sqrt{R_1^4 + T_1^4 - 2\left(R_1^2 + T_1^2 + R_1^2T_1^2\right) + 1}},$$

$$u_1 = \frac{2R_2}{1 + R_2^2 - T_2^2 - \sqrt{R_2^4 + T_2^4 - 2\left(R_2^2 + T_2^2 + R_2^2T_2^2\right) + 1}}, \text{ and}$$

$$V_1 = \frac{2R_2}{1 + R_2^2 - T_2^2 + \sqrt{R_2^4 + T_2^4 - 2\left(R_2^2 + T_2^2 + R_2^2T_2^2\right) + 1}},$$

and R_1, T_1, R_2, T_2 are the transmittance and reflectance of the top component layers and bottom component layers respectively. The multi-component albedo of Equation (44) is derived in Appendix E.

iii. The Frost Model, Step by Step

Initialization

- Choose a start date (e.g., 1 JAN 1990) and a step size (e.g., 90 days).
- Choose parameters: emissivity and choice of volatile.
- Load the mutual event albedo map.

- Calculate and store a mixing ratio (F, the fractional purity of the frost) for each surface element based on the albedos.

At Each Time Step

1. Compute positions for Pluto and Charon. We use Charon's position to define the line of zero longitude on Pluto.
2. Calculate the insolation at each surface element.
3. Average the insolation in latitude (equivalent to using the diurnally averaged solar flux).
4. Calculate the uniform global temperature using Equation (23).
5. Calculate the mass sublimation rate, $\dot{E}$, from Equation (25) for each surface element.
6. Multiply $\dot{E}$ by the duration of the time step, Δt, and accumulate the result for each surface element. This yields the cumulative mass transported to or from each surface element.
7. Assume a density of 0.91 gm/cm^2 to transform accumulated masses into frost depths [Scott, 1976]. Use the cumulative frost depths to modify the albedo map for the next iteration. If the frost depth is negative, estimate the amount of deposits that have accumulated on top of the frost; if positive, estimate depth of new frost layer. Use Equation (42) to get the new albedo at that surface element.
8. Increment the time by Δt.

Repeat each time step until the desired interval of time has elapsed.

iv. Frost Model Results

The results of 18 50-year simulations are shown in this section. We looked at α and β nitrogen, used three different starting conditions (Maps A, B, and C, shown in Figures 29-31), and employed three different ways of updating the surface albedos as a function of the cumulative frost depth.

We used three maps to test the sensitivity of a volatile frost model to structure in longitude and latitude. Models based on the uniform-reflectance map (Map A) are primarily functions of insolation during the post-perihelion quarter, providing a comparison to models using Maps B and C. This comparison illustrates some of the conditions that lead to bright polar caps and high contrast albedo distributions.

The models turned out to be very sensitive to the method employed for updating the surface albedos. The three schemes for updating the albedos range from doing no updating at all to using 1mm diameter particles in a multilayer reflectivity model. The diameter of 1mm represents the large end of plausible particle sizes [Eluszkiewicz, 1991];

we also used a multilayer model with 30 μm diameter particles.

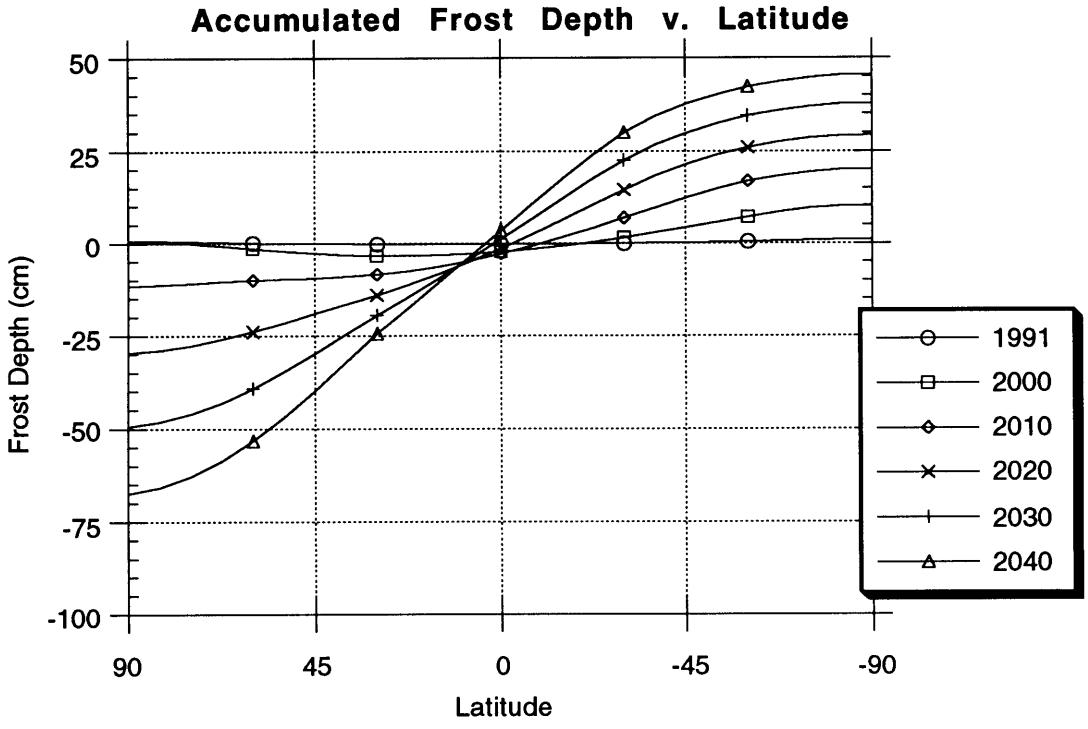

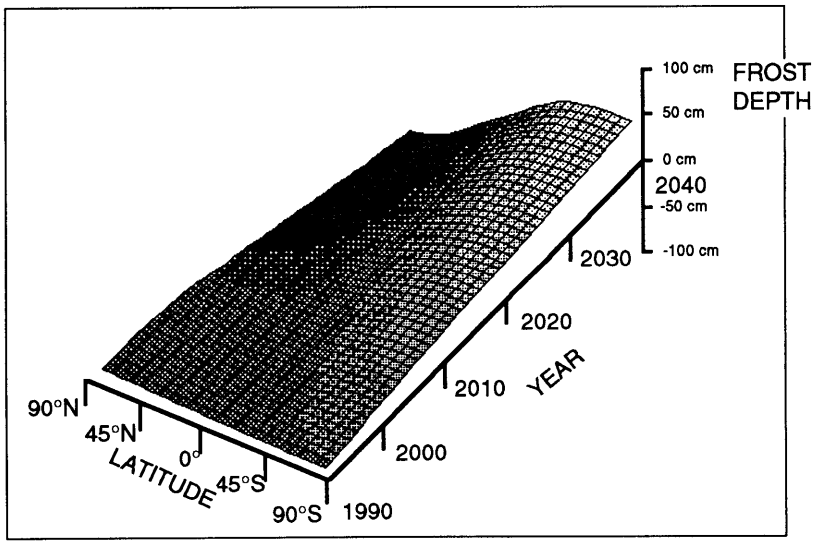

Figure 35
Map A
α nitrogen
No albedo update

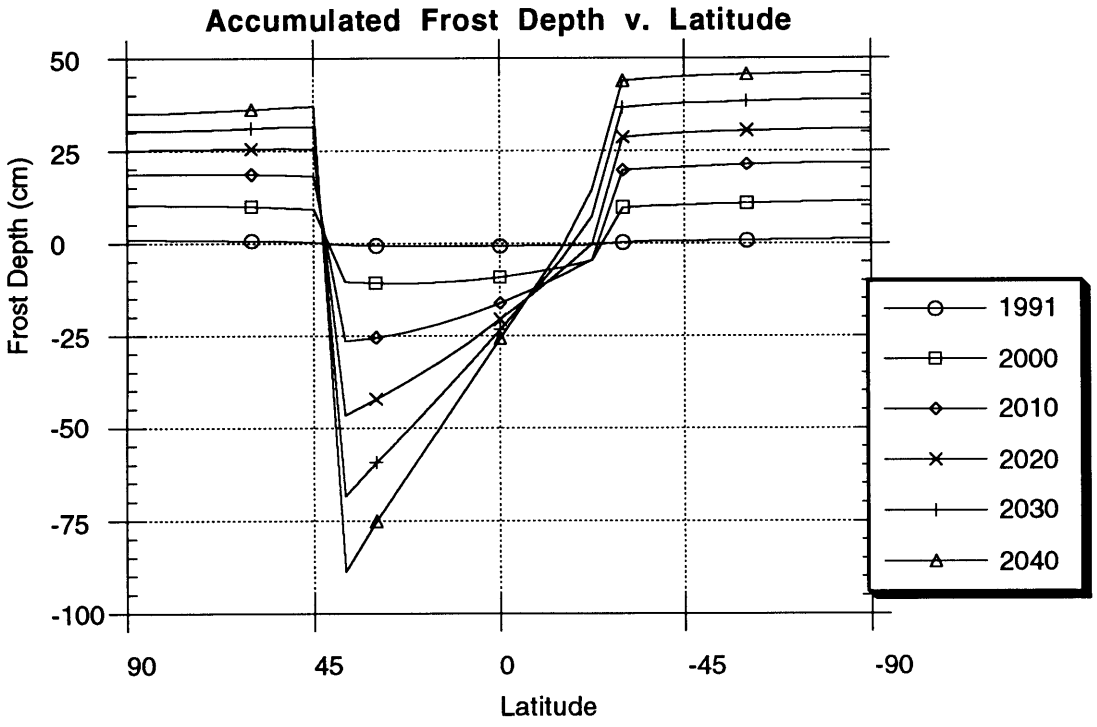

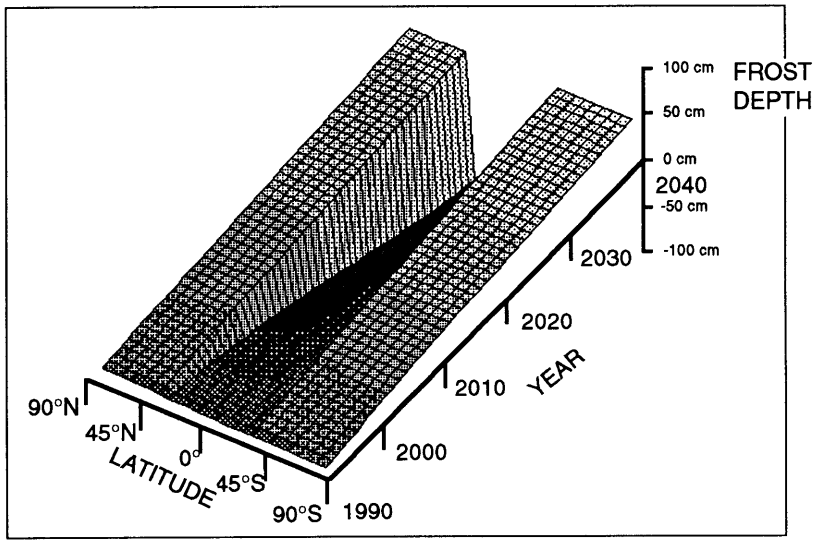

Figure 36
Map A
α nitrogen
30 μm particles in a multilayer model

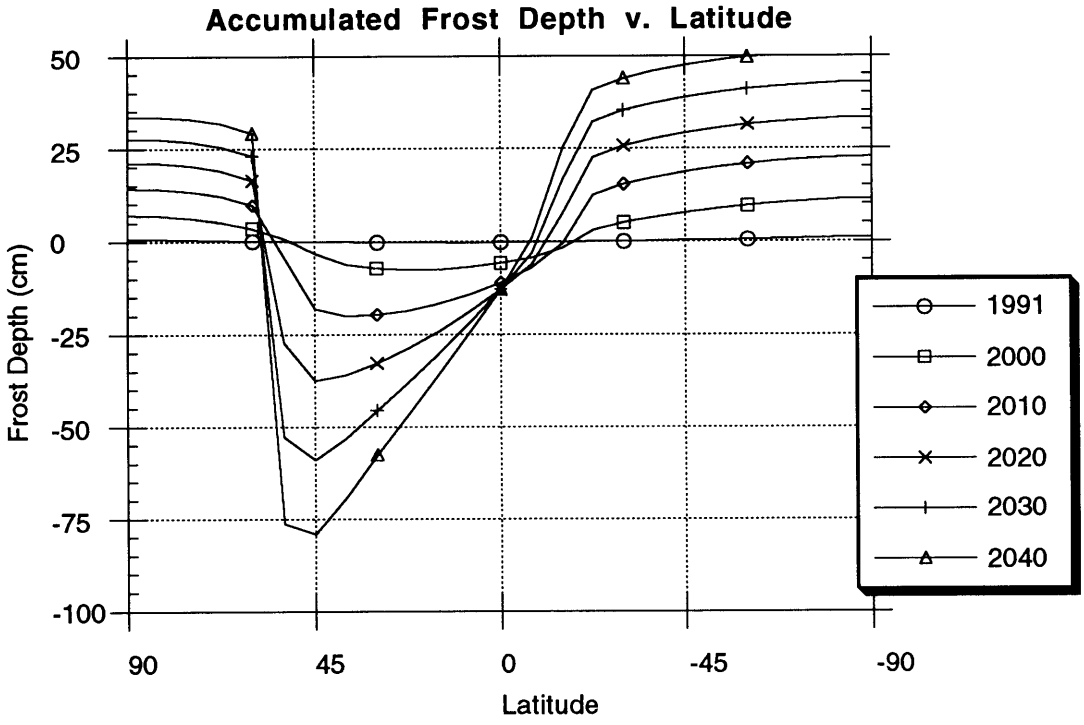

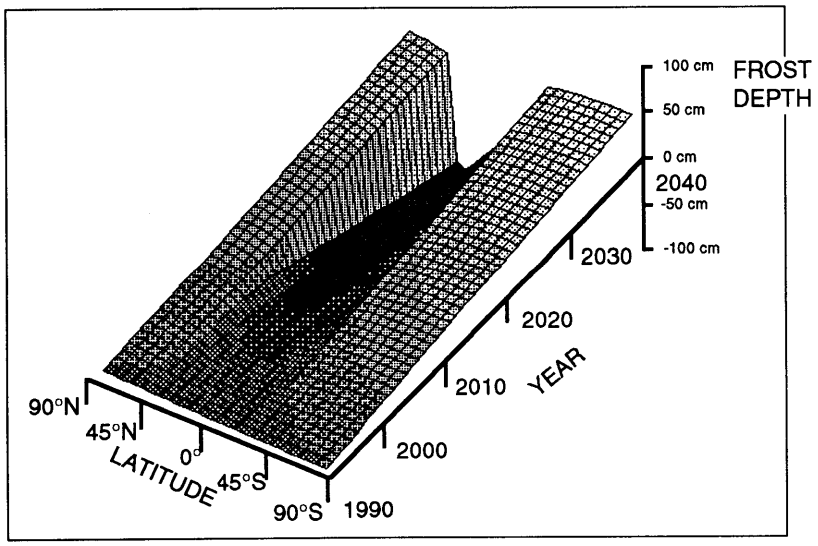

Figure 37
Map A
α nitrogen
1 mm particles in a multilayer model

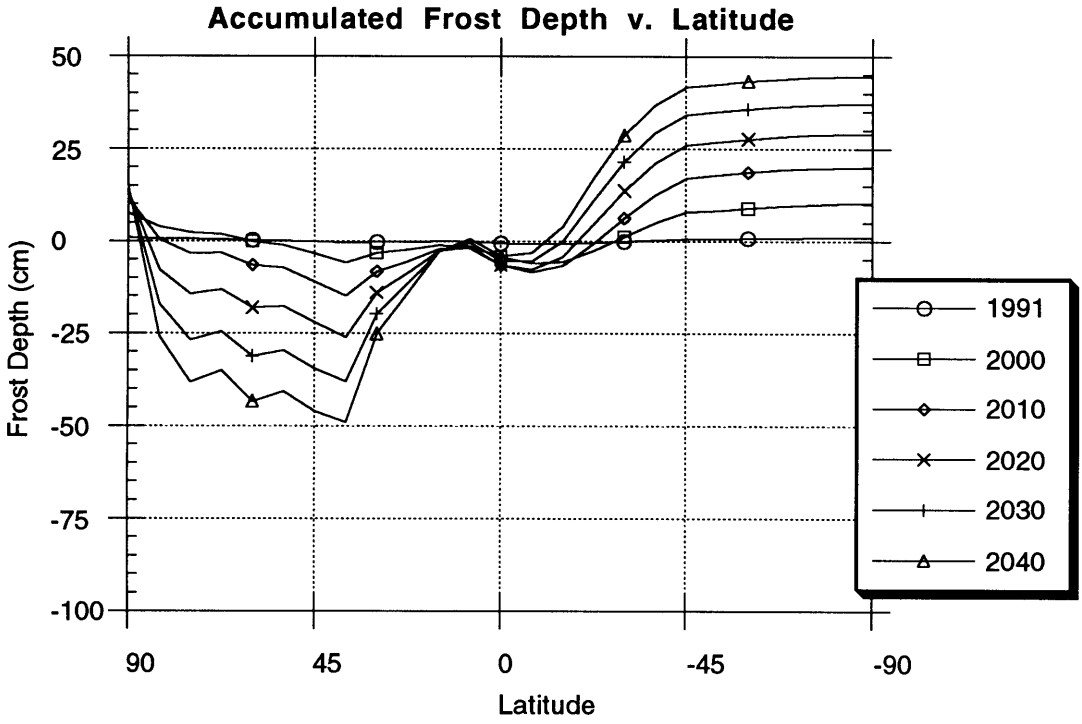

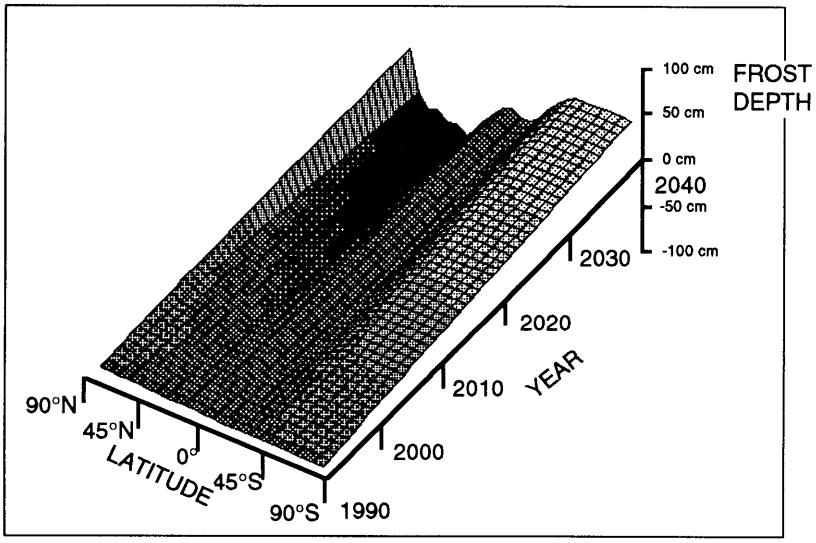

Figure 38
Map B
α nitrogen
No albedo update

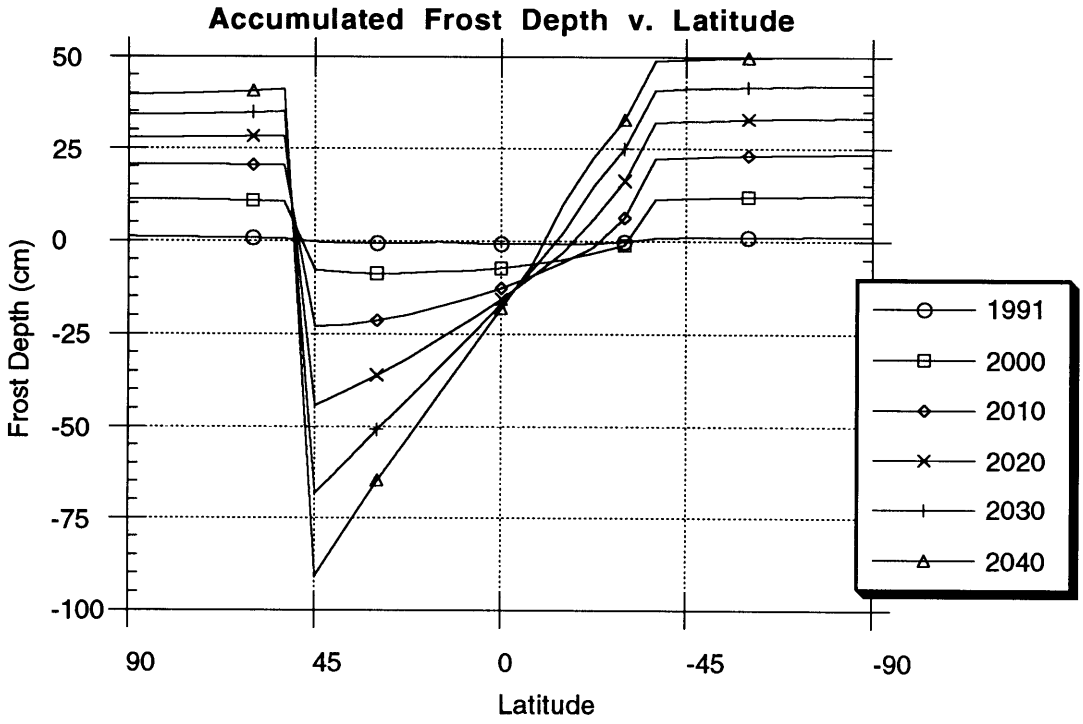

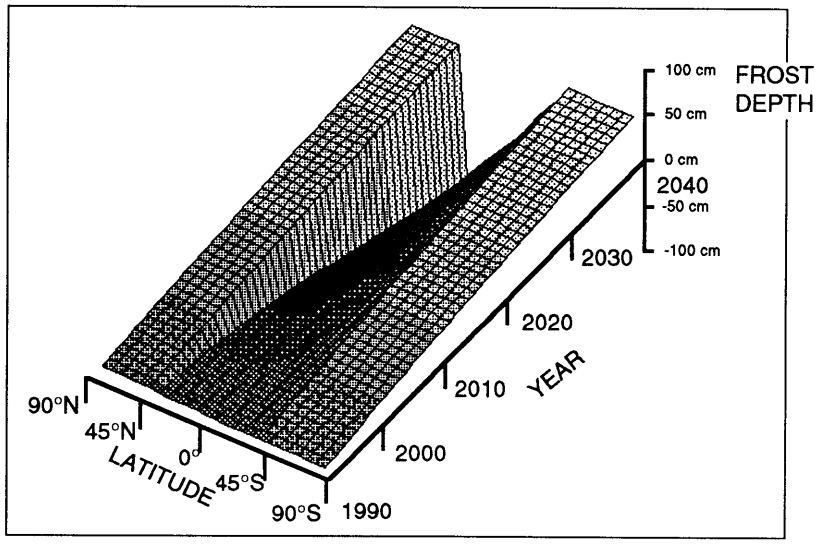

Figure 39
Map B
α nitrogen
30 μm particles in a multilayer model

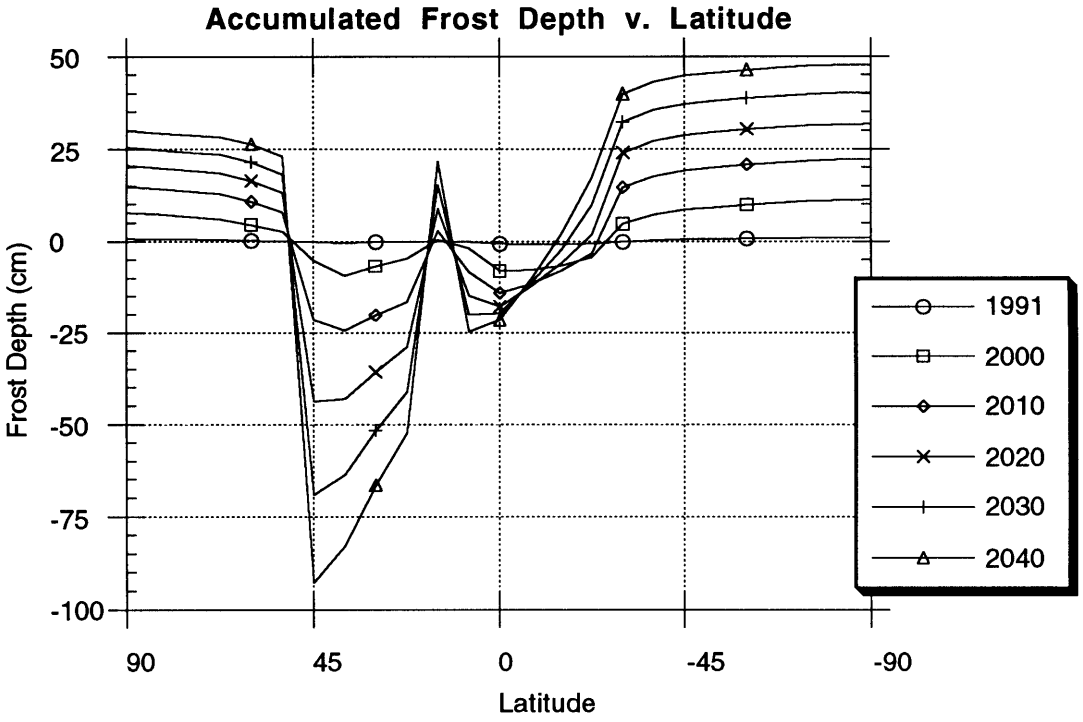

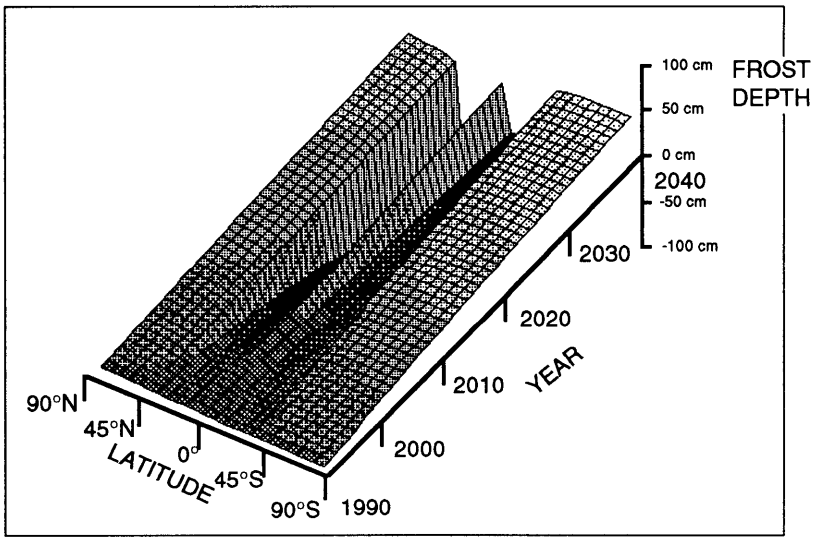

Figure 40
Map B
α nitrogen
1 mm particles in a multilayer model

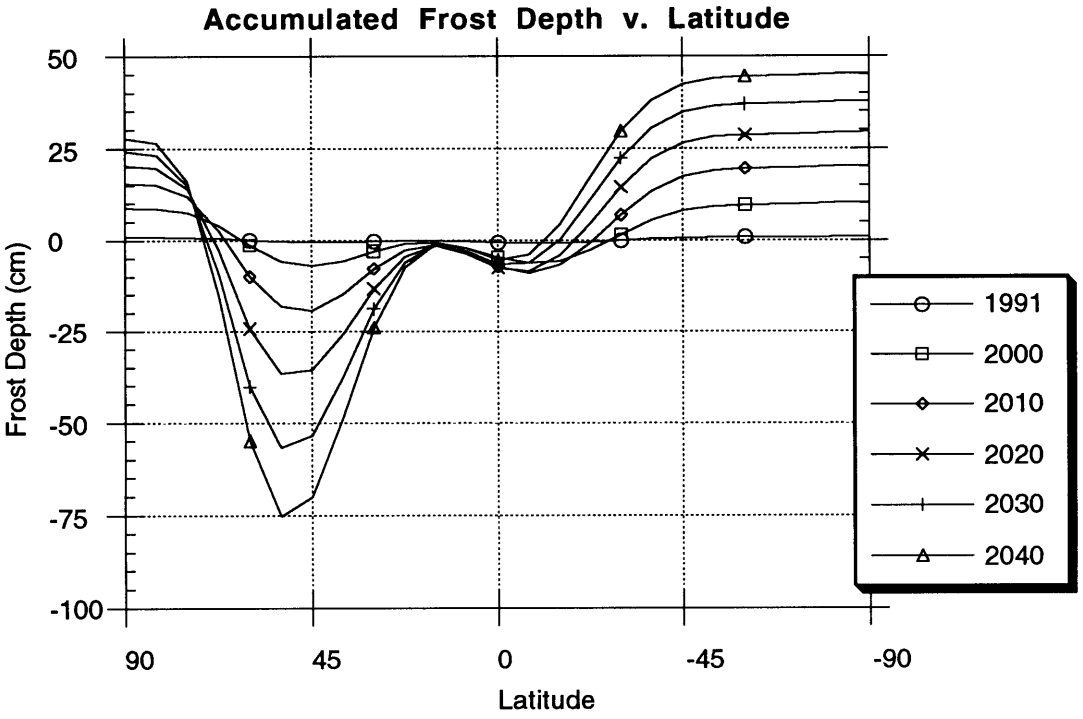

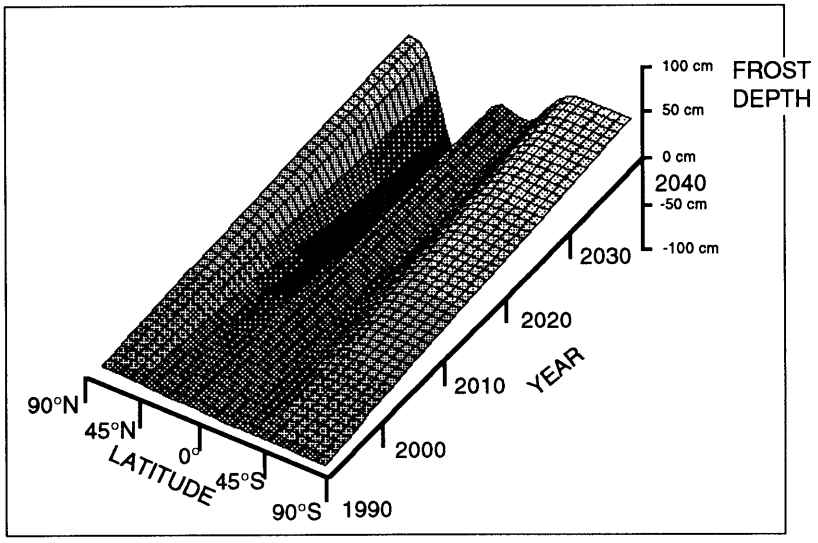

Figure 41
Map C
α nitrogen
No albedo update

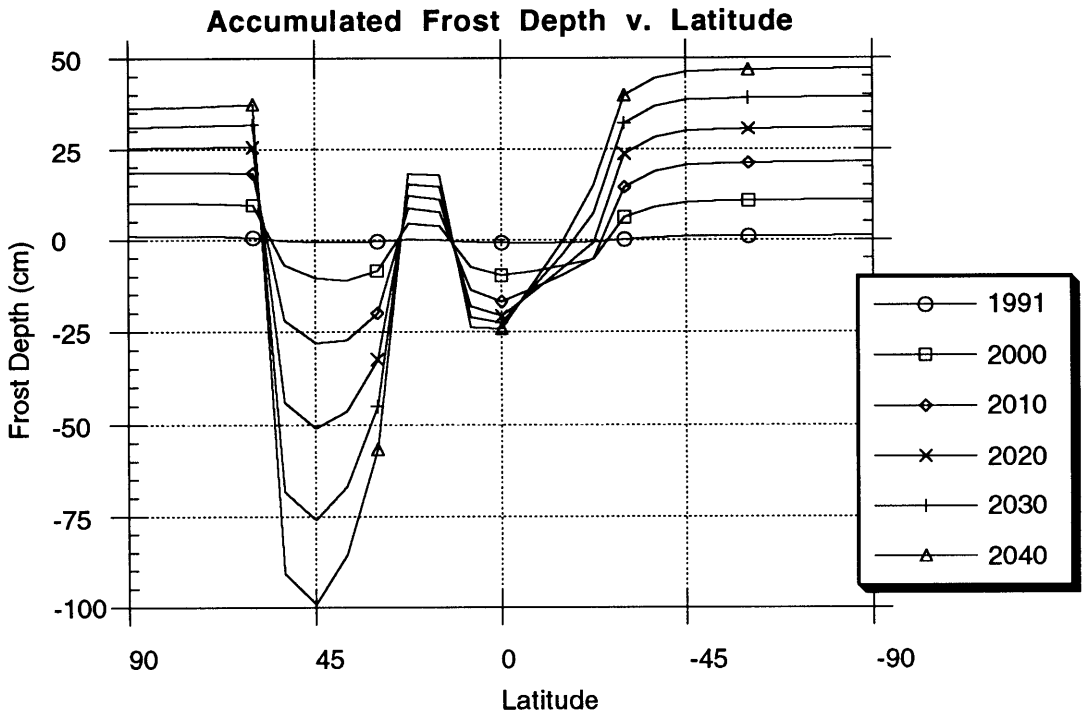

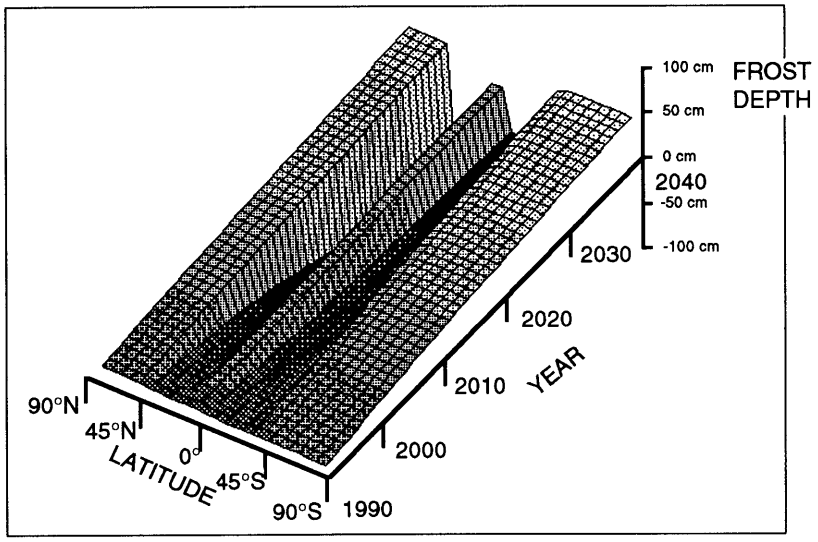

Figure 42
Map C
α nitrogen
30 μm particles in a multilayer model

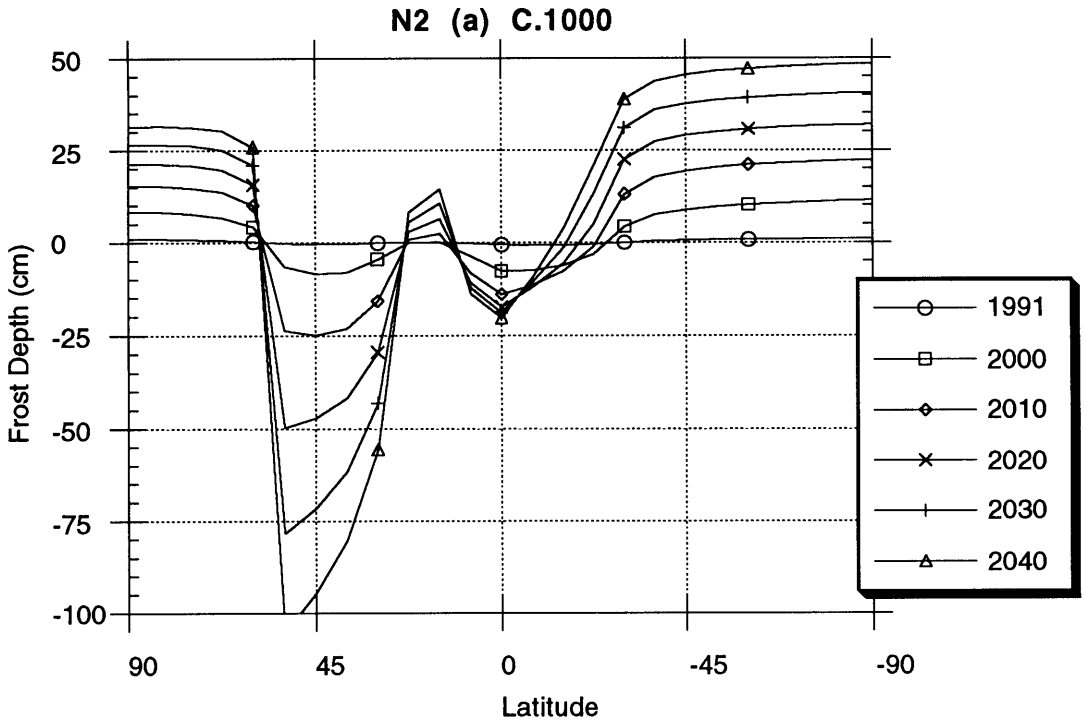

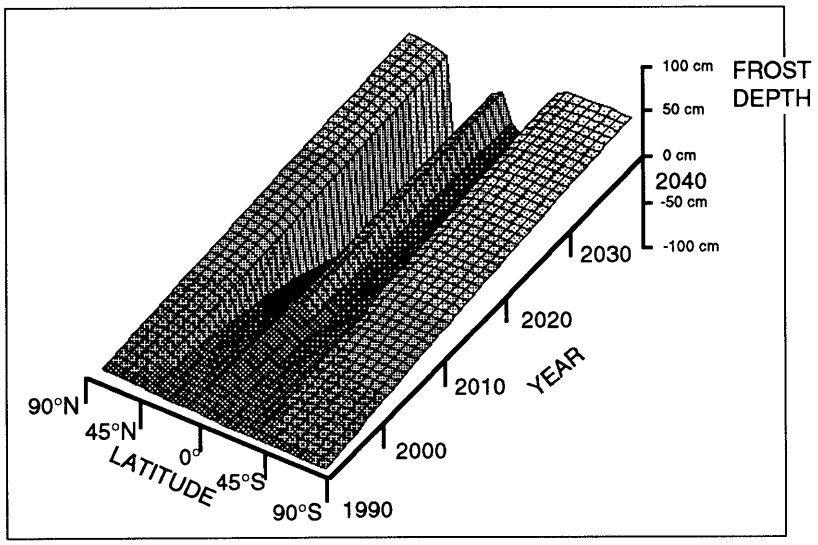

Figure 43
Map C
α nitrogen
1 mm particles in a multilayer model

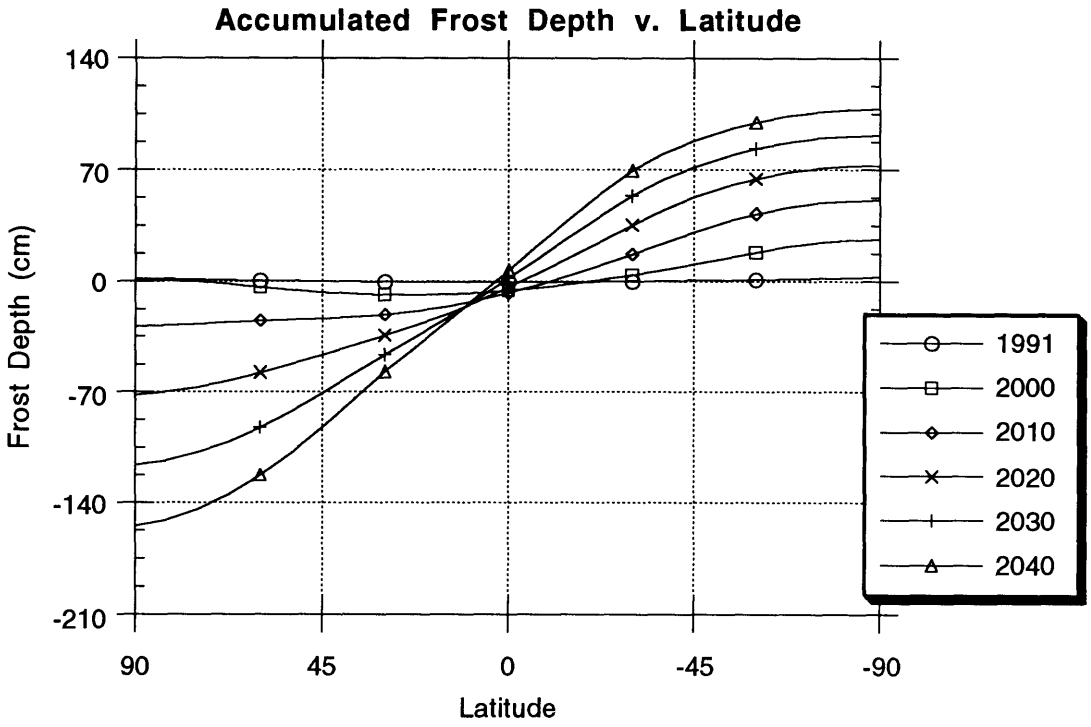

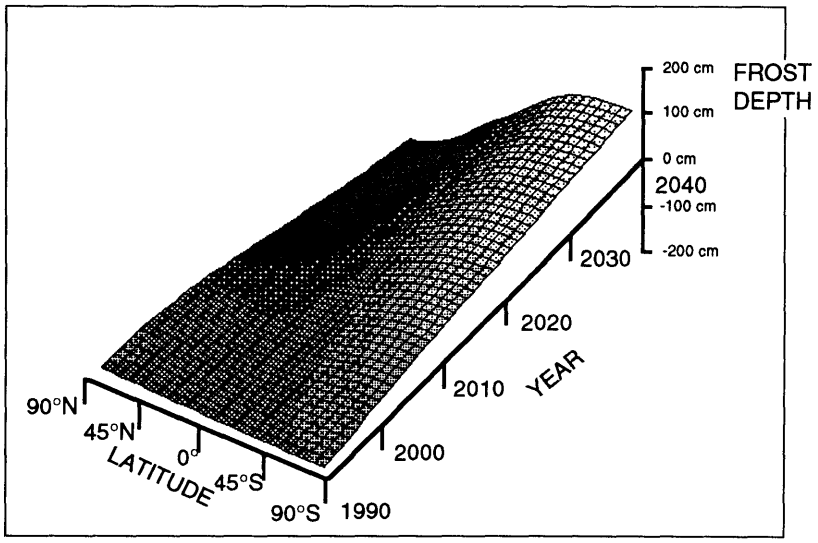

Figure 44
Map A
β nitrogen
No albedo update

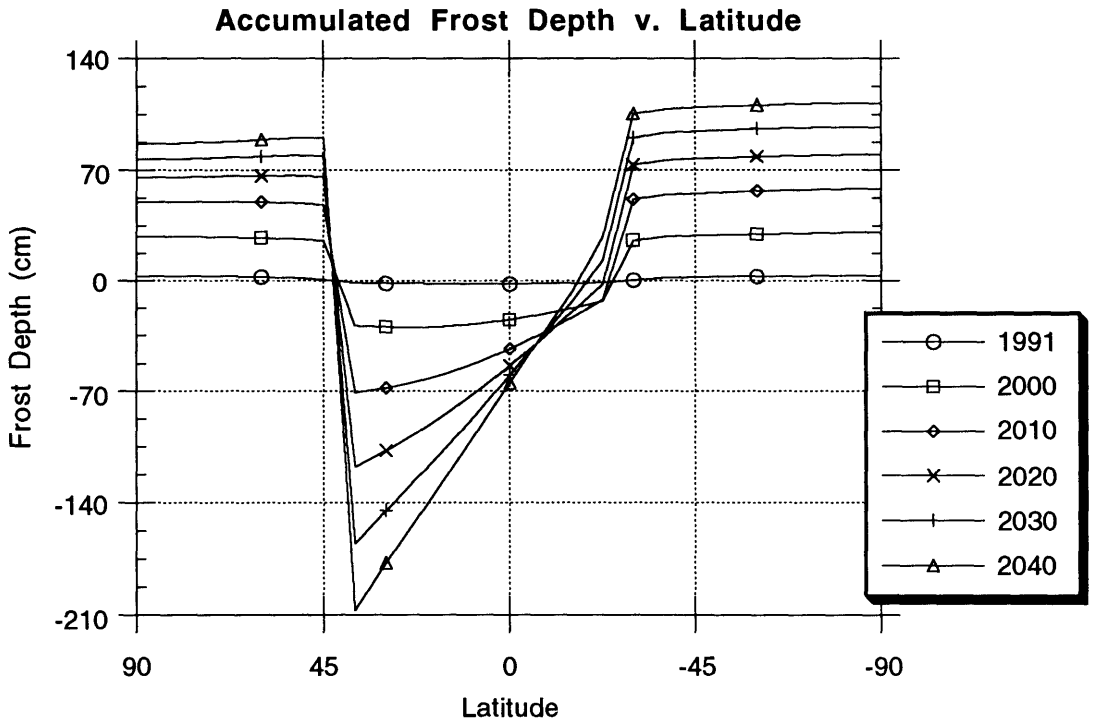

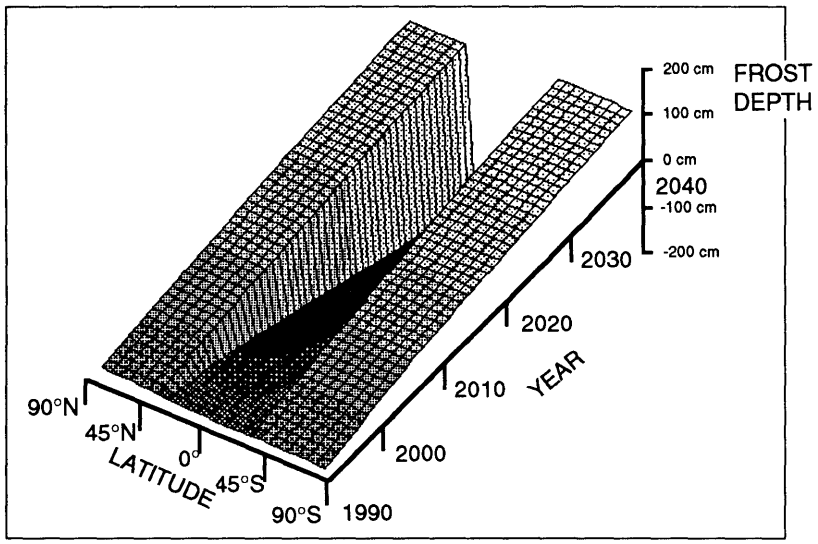

Figure 45
Map A
β nitrogen
30 μm particles in a multilayer model

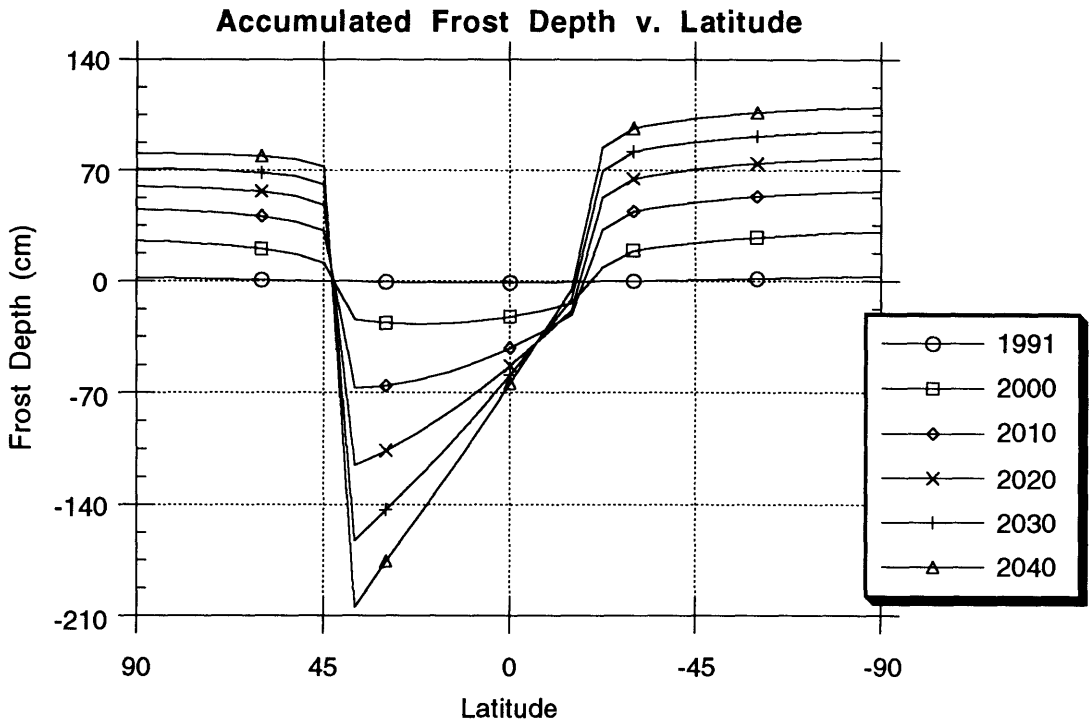

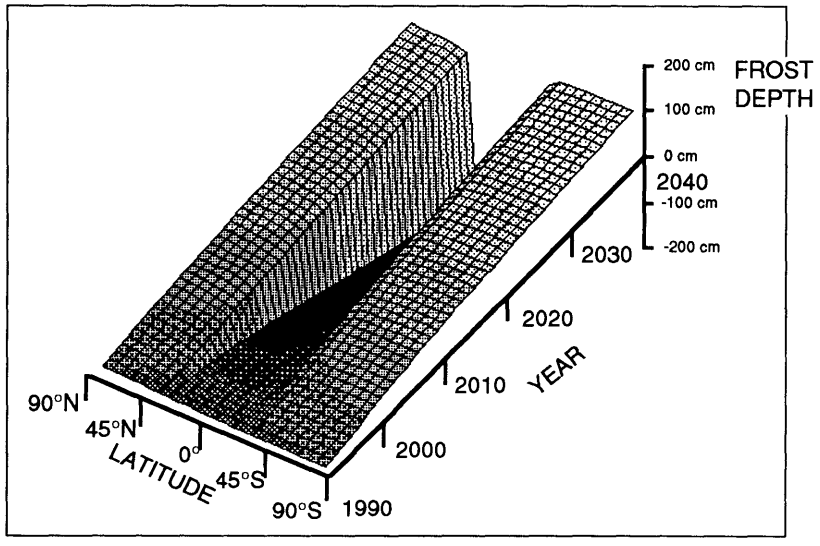

Figure 46
Map A
β nitrogen
1 mm particles in a multilayer model

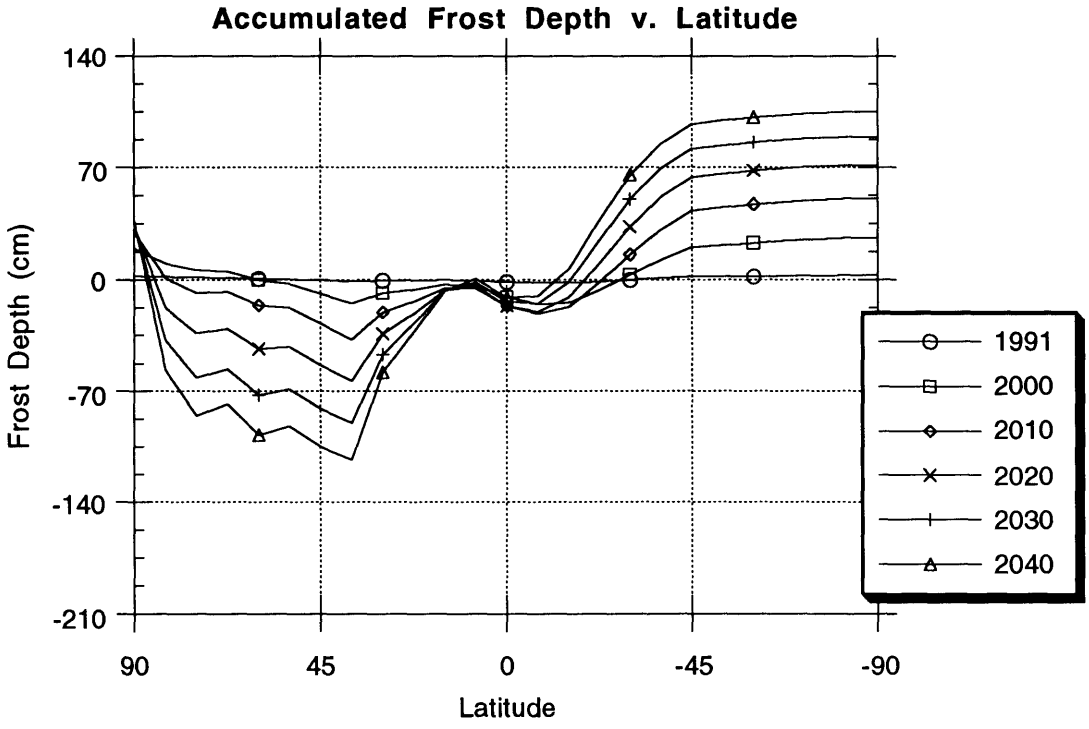

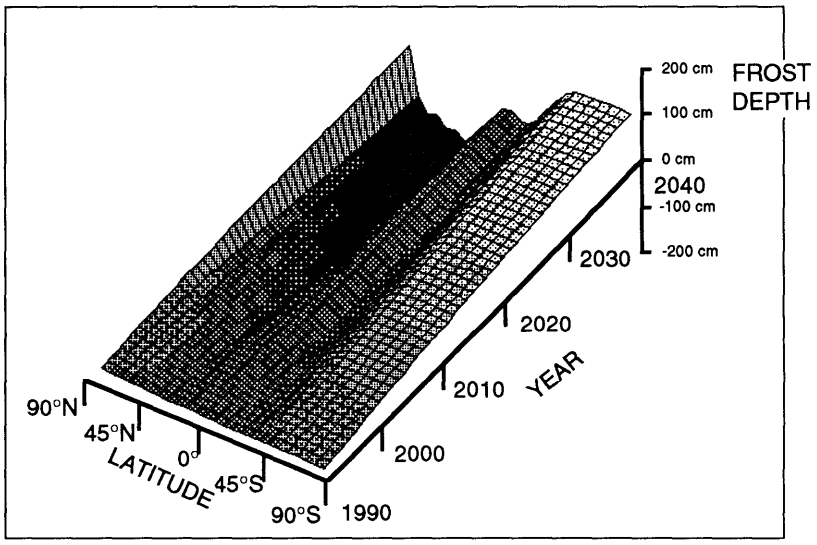

Figure 47
Map B
β nitrogen
No albedo update

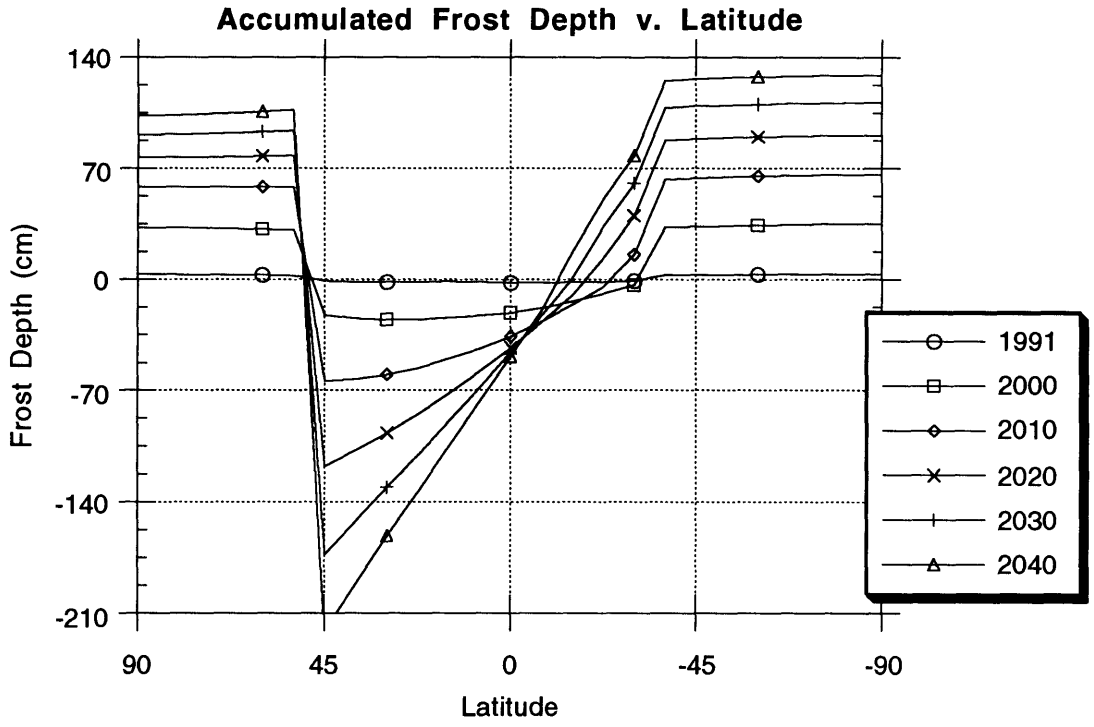

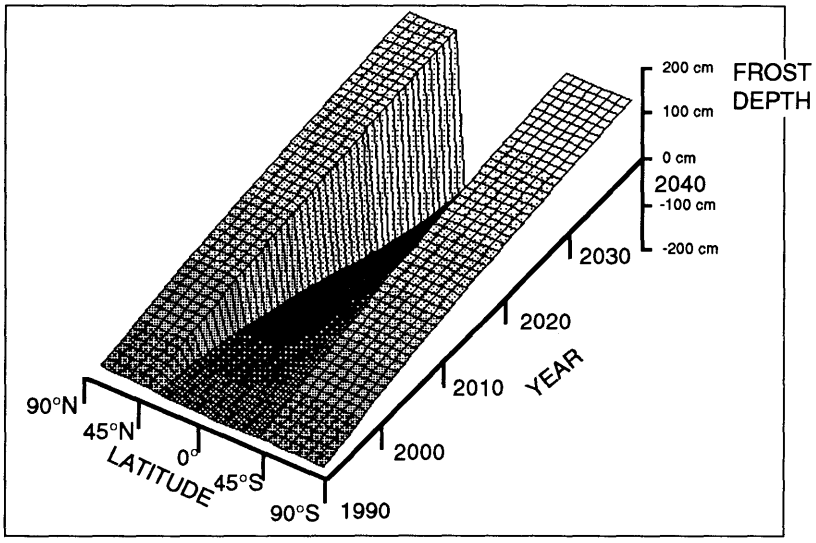

Figure 48
Map B
β nitrogen
30 μm particles in a multilayer model

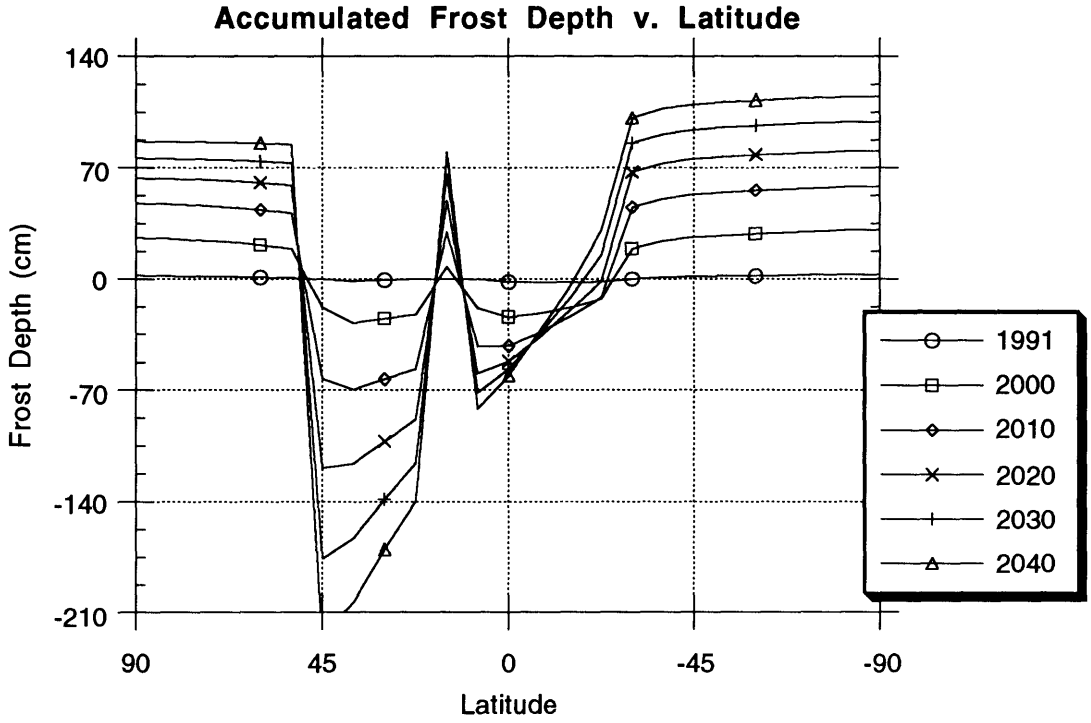

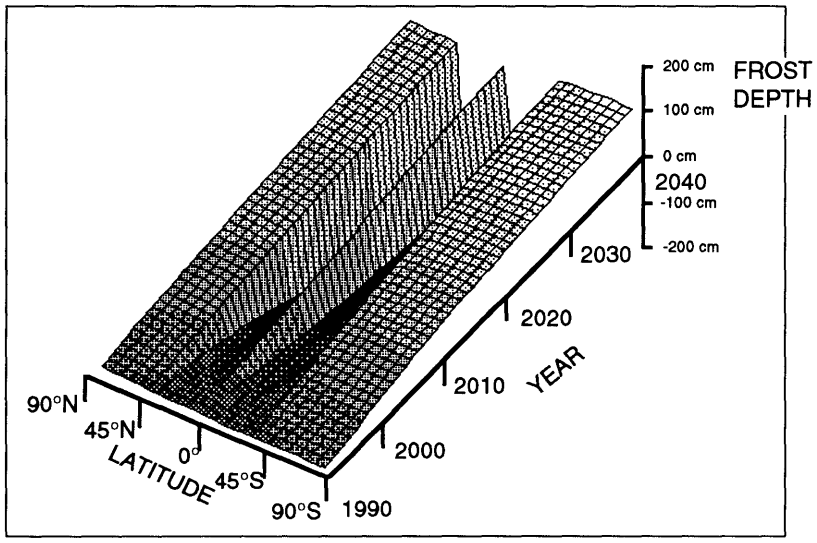

Figure 49
Map B
β nitrogen
1 mm particles in a multilayer model

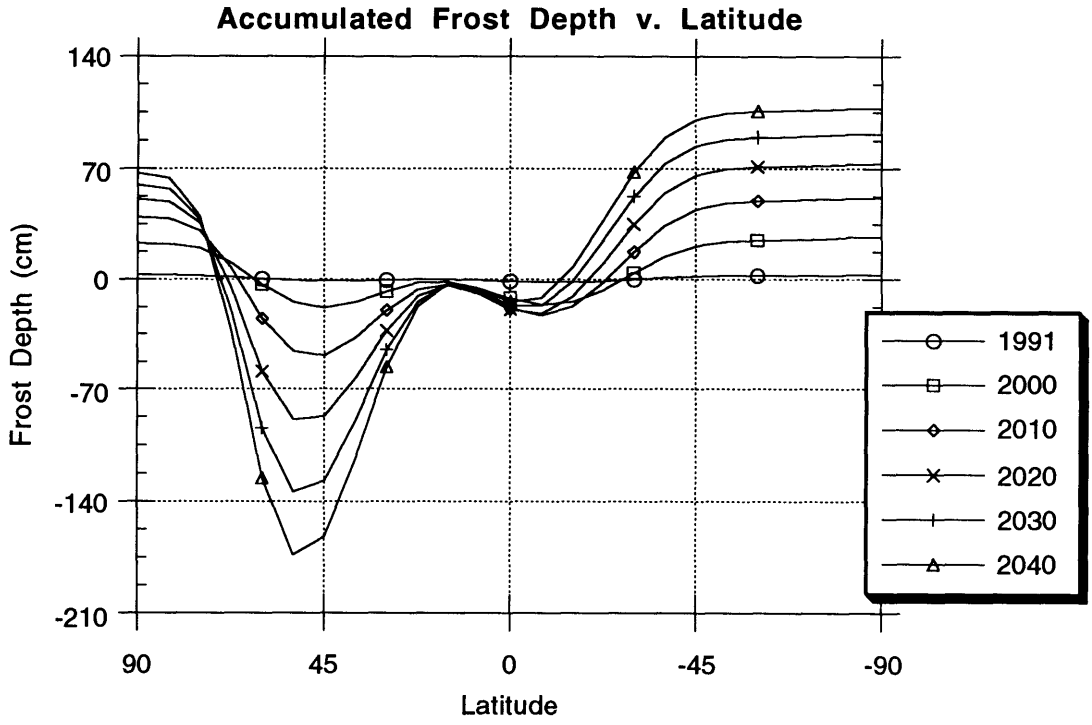

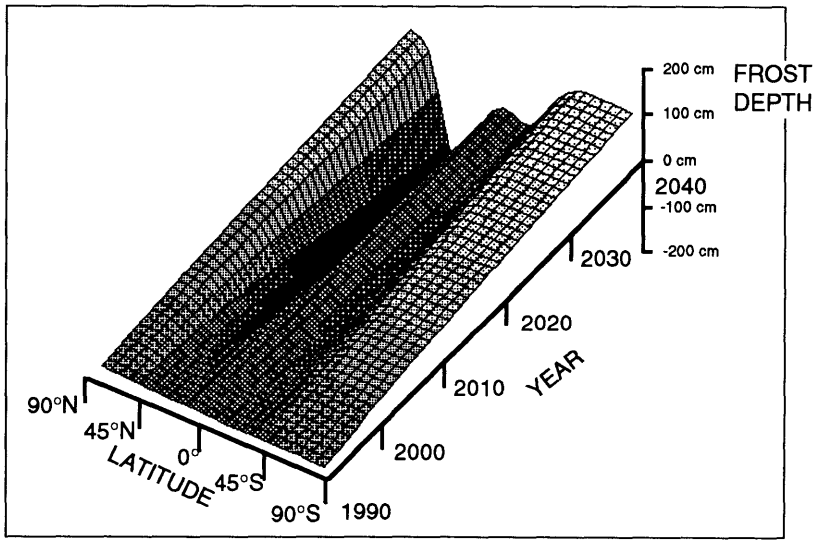

Figure 50
Map C
β nitrogen
No albedo update

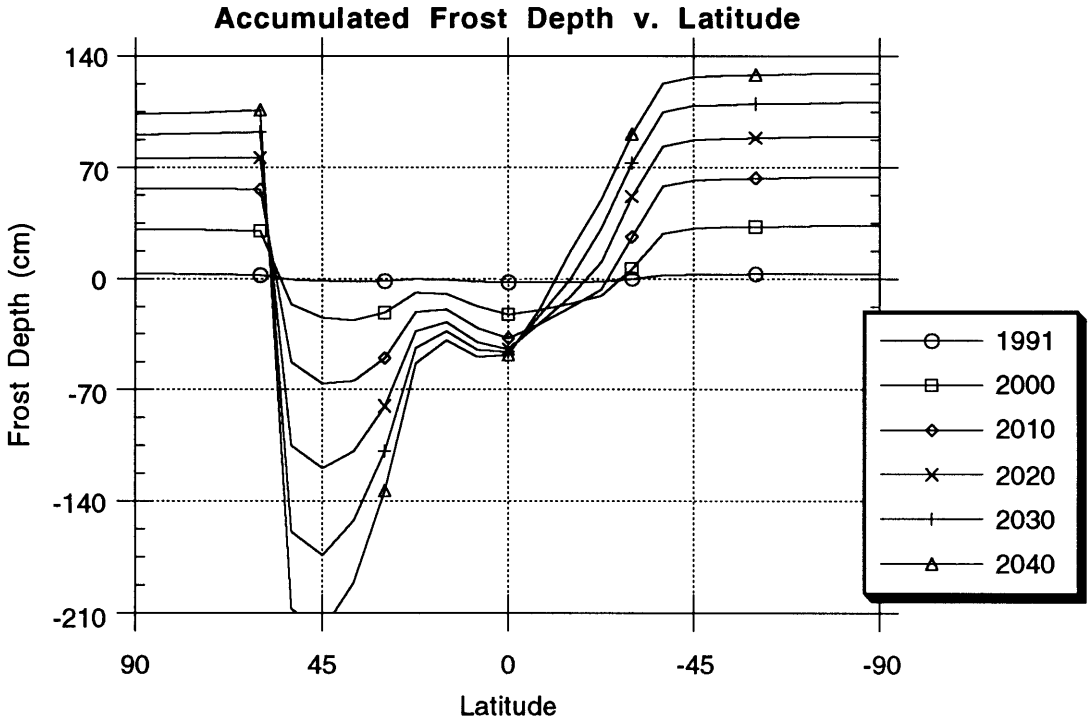

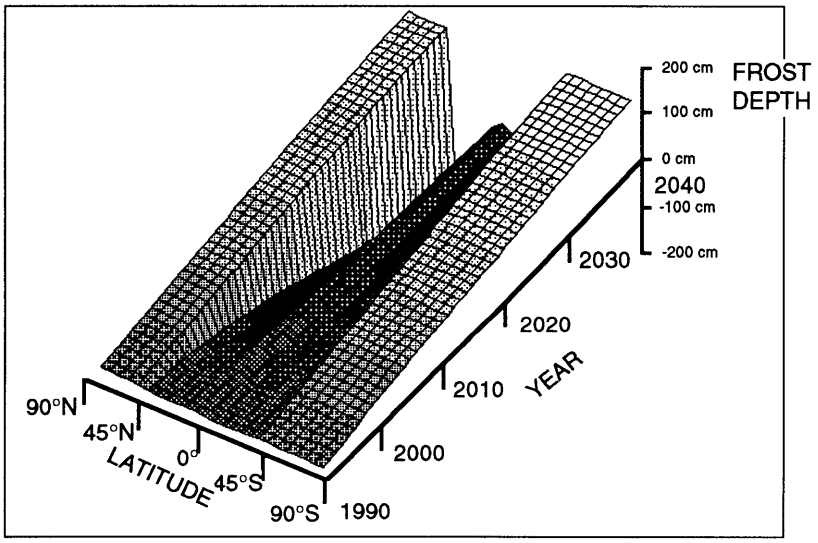

Figure 51
Map C
β nitrogen
30 μm particles in a multilayer model

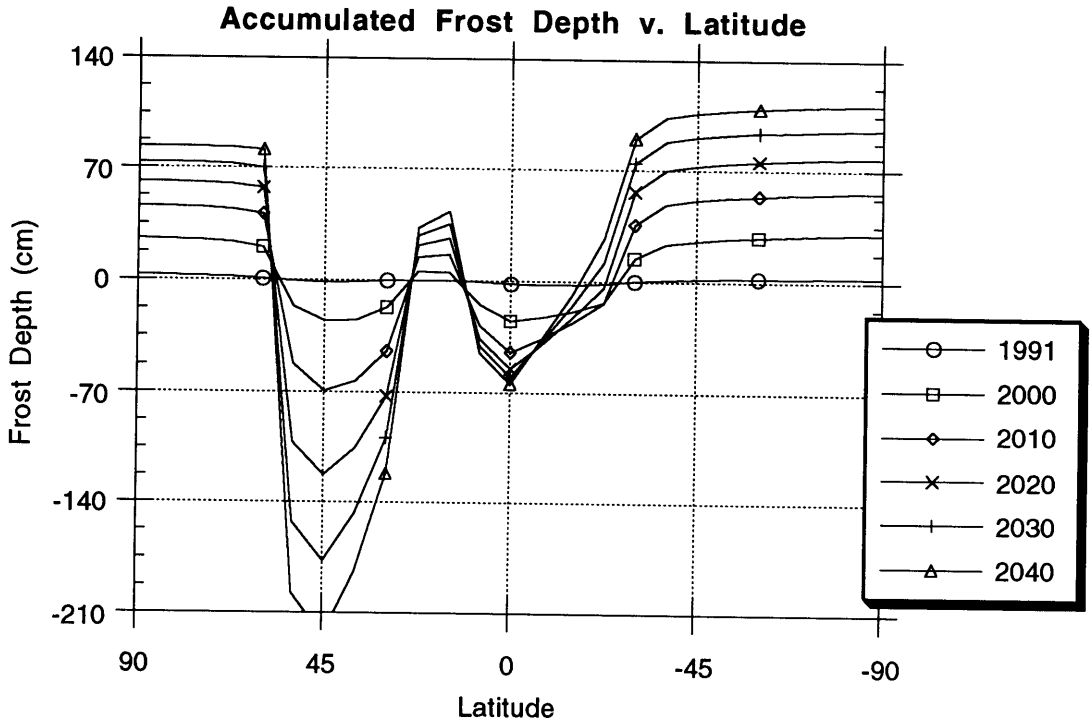

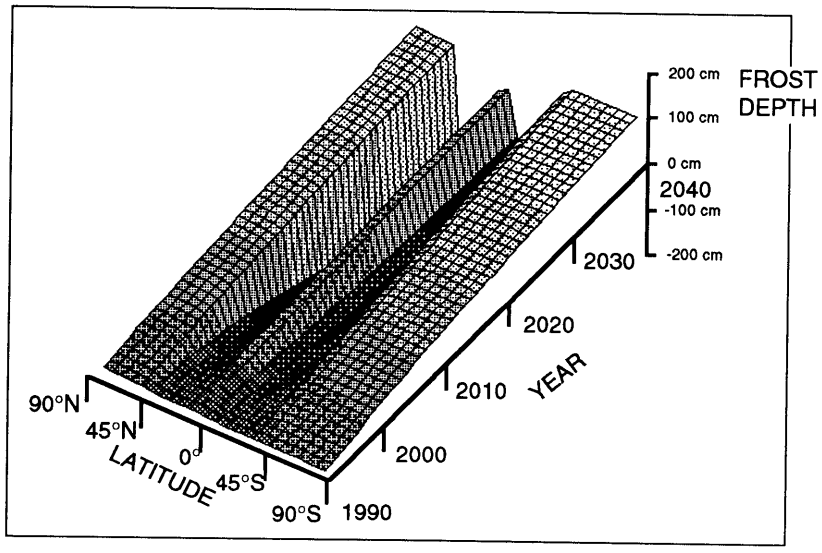

Figure 52
Map C
β nitrogen
1 mm particles in a multilayer model

The frost model results show that a significant amount of material is transported on a timescale of years. Roughly twice as much material is transported in the β nitrogen model compared to the α nitrogen one. The latent heat of sublimation is around 2.54 x 10^9 ergs/g for β nitrogen, about half of α nitrogen's latent heat, 5.0 x 10^9 ergs/g. Only half as much α nitrogen as β nitrogen needs to sublimate or condense to make up a local energy imbalance between insolation and thermal radiation.

The simulations based on the uniform-reflectance maps and no albedo-updating (the upper plots on pages 74 and 77) are simple functions of the net insolation. Wherever there is the most net solar flux over the 50 year period, that's where the most sublimation will take place. We know that this situation does not take place on Pluto, because Pluto's equator receives less insolation than the poles, yet there is no evidence of a frost band around the equator. These simulations do highlight the importance of the initial albedo distribution.

Bright regions on Pluto can be cold enough to form frost deposits, even when they are close to the subsolar latitude. When the simulation is initialized with Map A, the cumulative frost depth follows the cumulative insolation. But when the initial map has some bright regions, as Maps B and C do between 3°N and 20°N and at the extreme north pole, the net frost transported to those regions is *positive*, even though they intercept a relatively large amount of solar energy. This is a well known positive feedback effect – bright regions absorb less sunlight, stay relatively cool, and become sites of condensation which tends to make them brighter. This feedback mechanism affects volatile transport in longitude as well as latitude. A simulation using Map C demonstrates that longitudinal structure in the albedo map is important in determining regions of condensation or sublimation.

There is a bright region centered around 10°N of Map C that reflects 80 – 90% of the incident radiation. Even when the subsolar latitude is near the equator, this mid-equatorial bright region does not absorb enough sunlight to balance the heat lost from thermal radiation. The large amounts of material transferred from one latitude to another might lead one to expect that any albedo features would be quickly obliterated by new frost deposits. For example, Figure 35 (and most of the other multilayer models) show that some bright features may not accumulate a dark surface layer of residues, even when they have been in constant sunlight. In contrast, dark regions in the shade are quickly covered by bright frost deposits. The positive feedback experienced by bright, high-insolation regions of the planet is a possible explanation to the question of why the brightest parts Pluto and Triton are located in the most highly insolated regions. We did not implement the empirical albedo-brightening law of Spencer [1990] because the

albedo-brightening effect takes place without it. With Spencer's law in place we would not know the source of the albedo-brightening.

As Figure 35 demonstrates, a north polar cap develops in all of the models. In the non-albedo-updating models this northern cap disappears after about five years as the subsolar point migrates to the northern hemisphere. In the multilayer models, however, the frost deposited on the northern cap is substantial enough to establish a northern cap that survives and continues to grow despite the high solar flux. The north pole, once brightened, absorbs only about 5% of the incident sunlight, as opposed to the initial value of 50%. The survival and growth of the north polar cap through the year 2040 is evidence that the south pole should survive the pre-perihelion part of Pluto's orbit.

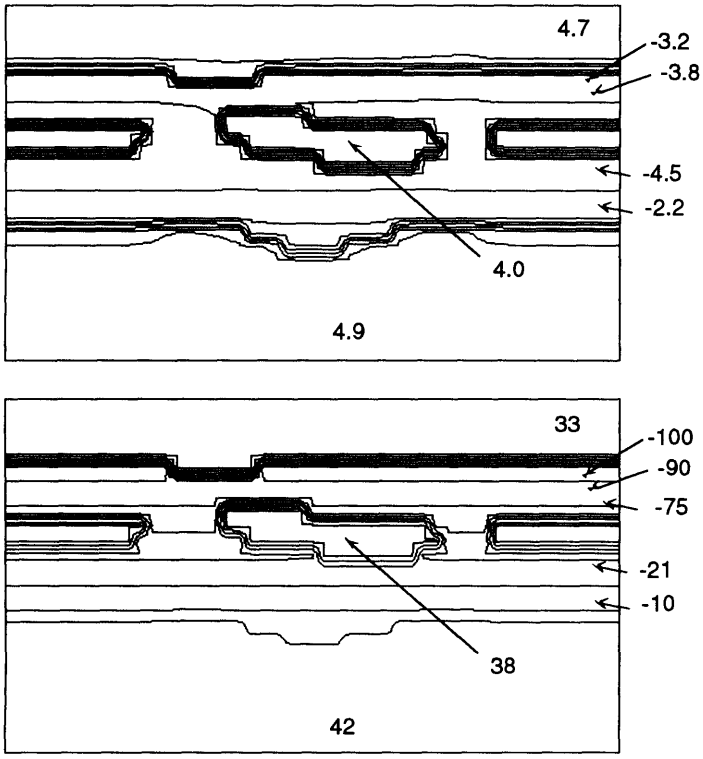

Figure 53 (a,b). The top plot shows frost depths after five years (1990 - 1995) predicted by a model initialized with map C and using the multilayer albedo-updating scheme with 30 μm particles. The lower plot shows the same simulation after 50 years, in 2040. Notice that the north pole has brightened by 1995 and *continues* to be a site of frost accumulation though 2040 *even though it is in constant sunlight.* The units of the contour labels are g/cm^3.

The formation of the north polar cap points out that the albedo-updating scheme is a major weakness of our volatile transport model. If we had started the simulations in 1985 instead of 1990, the models would predict a polar cap over the north pole in 1990.

The multilayer model changes the surface reflectance to 0.95 when just a few 30 μm-thick layers have been deposited. The effect is lessened by assuming 1 mm particles instead of 30 μm ones, but the models still progress rapidly to very bright and very dark albedo distributions.

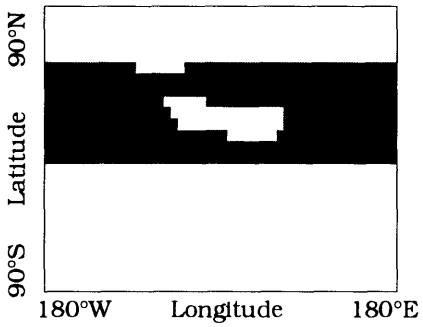

Figure 54. After five or ten years, all of the albedo-updating models produce maps like this one. The condensation sites map to brightnesses of 0.95 and remain there, while the darker regions are forced to sublimate at higher rates because their area has decreased.

The fact that bright and dark regions can coexist and tend to form next to each other helps explain some of the high-contrast features we see in the mutual event maps. Nevertheless, the extreme contrast shown in Figure 54 illustrates the deficiency of our albedo-updating scheme. There is undoubtedly more going on than simple frost deposition and sublimation. We have neglected UV photolysis, the presence of dark silicates, the possibility of bare ground, and mixing of the frost "regolith," among other things. Our motivation for trying the 1 mm thick multilayer model was the hope that the thicker layers would better model planetary conditions in forming bright or dark layers. For the most part the 30 μm thick and the 1 mm thick multilayer models have the same results, with the exception of the evolution of the bright feature at 20°N. In the 30 μm models this bright feature is covered by a dark layer and becomes a sublimation site during the post-perihelion quarter. In the 1 mm model the site remains bright - the darkening effect is slowed because a smaller number of 1 mm thick dark layers form. The difference between the two models underscores the need for more detailed albedo-updating schemes.

Another result of the multilayer models' propensity for brightening the surface too quickly when some frost has condensed is the north polar cap that would supposedly develop during the post-perihelion phase of Pluto's orbit. Enough frost is deposited on the north pole during the five or six years to theoretically form an optically thick layer of bright frost. Will the north pole develop a bright polar cap? We believe not, because no

such cap formed (that we can see in our maps) during the five or six years *before* perihelion, and one surely would have in our model if we began the simulation in 1980 instead of 1990. Figure 55 plots the initial thickness of a nascent north polar cap.

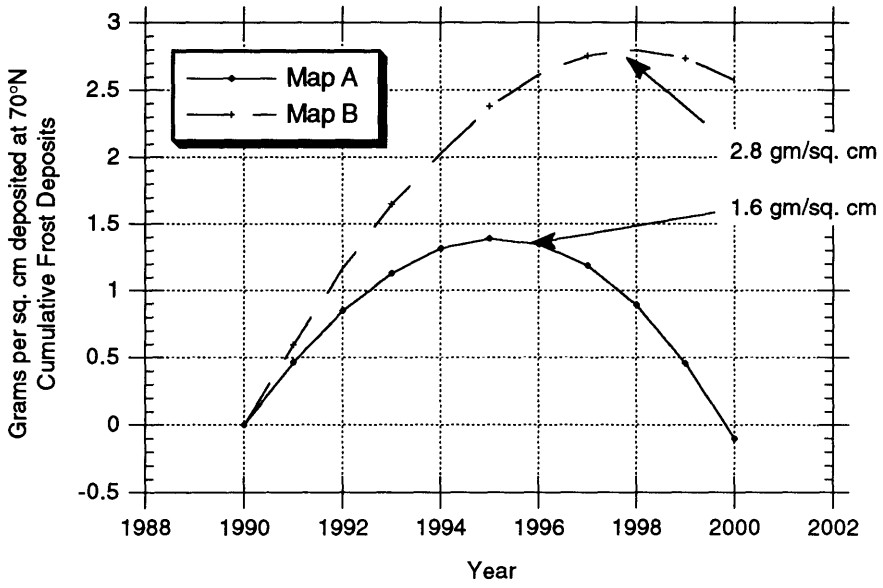

Figure 55. Cumulative α nitrogen frost depths at a latitude of 70°N as predicted by the constant albedo model. The peak depths for Maps A and B are 1.6 and 2.8 gm/cm^2, corresponding to thicknesses of 1.7 and 3.0 cm.

Figure 55 shows that both Map A and Map B (which has a bright northern strip) develop an optically thick frost layer by 1995. Will these layers be optically thick on a rough planetary surface? The inability of the multilayer models to explain the lack of a bright north polar cap is their most serious deficiency. Some of the results of the multilayer models (high contrast surfaces, bright north poles) must be taken with a grain of salt until further work can be done on the surface processes that control Pluto's albedo during the migration and deposition of frost.

VI. Summary of the Volatile Transport Model and Discussion of Future Work

Frost Model Results

We implemented a simple global equilibrium model to predict Pluto's bulk atmospheric parameters over the next 50 years. We found that Pluto's surface temperature drops about five and a half degrees from 1990 to 2040, regardless of the surface volatile. Because the volatiles in our model have vapor pressures with steep temperature dependencies, the drop in temperature corresponds to 97% of the atmosphere freezing out.

As Pluto's atmosphere thins, the winds required to balance the global pressure gradient increase. We predict that these winds might exceed Mach 1 as early as 2050. Because the surface pressures are steep functions of temperature, the cross over into the supersonic regime might happen decades later or not at all. The 2050 cross-over date represents a lower limit corresponding to the coldest plausible surface temperatures (and therefore the lowest surface pressures). We are confident that the global equilibrium model is valid for the period from 1990 through 2040.

We found that the amount of material transported in fifty years is easily enough to resurface the planet. The equator to pole migration was about 40 gm/cm^2 for an α nitrogen surface, and over twice that much for β nitrogen. This volume of material is comparable to amounts predicted by Spencer in his Triton model [1990], and is certainly sufficient to change Pluto's albedo on a timescale of decades. The use of lightcurves spanning 20 or 30 years in a surface map reconstruction is therefore suspect.

We found that bright regions on Pluto can stay bright even when they are close to the subsolar latitude. A bright north pole, for example, would not only survive direct sunlight in 2040, but continue to accumulate new frost. This positive feedback mechanism for keeping bright regions bright also tends to create albedo maps with neighboring dark and bright elements. A bright element in the middle of a highly insolated band remains bright in sharp contrast to the surrounding areas. This phenomenon is suggestive of high contrast features we observe in the mutual event maps. The location of the map features is not predicted by the short term frost model.

The albedo-updating models produced a north polar cap which accumulated frost continuously through 2040. It is likely over 1 cm of frost would accumulate on the north pole during the early nineties. This new frost layer, which extends down to about 70°N, is thick enough to create a bright polar feature which stays bright throughout the fifty

year simulation. The south pole accumulates the most frost of any region on the planet, because it is bright and because it is moving into continuous darkness. Since the north pole is gradually coming into constant sunlight, the brightness of Pluto over the next few years should indicate whether or not the north pole has actually brightened.

Future Work

Our models included insolation and thermal radiation effects. Now it is time to consider secondary effects, such as thermal inertia of the surface, solid state greenhouses, darkening rates of methane frost, atmospheric loss to space, and so on. Reports from Spencer and Moore [1992] indicate that thermal inertia can maintain an asymmetrical polar cap on Triton. In addition to these effects, there are key assumptions in our model that need to be verified. In particular we would like to know if the surface is entirely covered with volatiles. Further modeling is needed of surface processes to determine how the albedo changes as frost is deposited.

The most challenging project following the global equilibrium model contained in this thesis is a model capable of supersonic winds and non-equilibrium conditions. If Pluto does have supersonic winds during the aphelion portion of its orbit, we will need to model the transition from the subsonic to the supersonic regimes. Such a model would undoubtedly resemble the Io model of Ingersoll et al. [1985].

Appendix A.
The Data Set

There are six separate lightcurves used in this paper, collected at the University of Texas McDonald Observatory at approximately yearly intervals. The observations were made with the 0.9 m, 2.1 m and 2.7 m telescopes, using an RCA 8850 phototube. We recorded 10 second integrations, alternating between blue and visual Johnson filters. The lightcurves used in this paper are blue only, since the detector yields a higher signal to noise ratio with this filter. The ten second integrations are binned into 100 second intervals. The rms error for each 100 second data point was estimated from either Poisson statistics (square root of the number of incident photons) or the mean standard deviation of the ten observations, whichever is larger. The actual data set is listed with the source code in Appendix F in a file called `ALL_DATA 85-90`. The three columns of this file are time (Julian Day), normalized intensity, and standard deviation. The times have been corrected for light delay, so they represent events as they occurred on Pluto, not as observed on the Earth.

We have subtracted a constant representing Charon's contribution from each point. Charon only rotates about 12° during each five hour transit, and we assume that Charon's brightness is constant over that small range. We subtracted 15.3% of the average baseline (pre- and post- transit) intensity to remove Charon's contribution. Charon's contribution is estimated from occultations of Charon by Pluto in which the mid-event intensity is 84.7% of the baseline level. Pluto's anti-Charon side has about the same spectral color as its sub-Charon side [Binzel, 1988], and we assume that Charon has uniform brightness.

Note that the linear least squares problem is based on *derivatives* of contributions to the total brightness of the Pluto-Charon system. As long as Charon's contribution is constant over the 5 or 6 hours of each event, the solutions found by the least squares procedure will be independent of the fractional intensity assigned to Charon. Thus, the exact contribution due to Charon is not a major concern; a more important issue is the assumption that Charon's contribution has been constant over the six year period.

Has Pluto's brightness changed over the mutual event period? We perform a linear fit through the pre- and post-event baseline magnitudes of the 1985 - 1990 lightcurves.

Table A-1. Calibration of the lightcurve baselines

Event Date	Pre-Event B-Mag. ± error		Post-Event B-Mag. ± error	
17 FEB 85	16.162	±0.016	16.153	±0.0028
20 MAR 86	16.187	±0.0009	16.170	±0.0013
22 MAY 87	16.176	±0.0014	16.167	±0.0027
18 APR 88	16.183	±0.0015	NA	
30 APR 89	NA		16.164	±0.0012
24 FEB 90	16.179	±0.002	16.183	±0.0008

Pluto's pre- and post-event baseline B-magnitudes (Table A-1) yield slopes of -0.0021 ± 0.0016 and 0.0036 ± 0.0024 magnitudes per year respectively. A weighted average of these slopes (which are in opposite directions) yields a slope of 0.00026 ± 0.0014 magnitudes per year. The total magnitude change over the entire six year mutual event period is less than the smallest error of any individual data point. Hence we normalize all of the lightcurve baselines to one.

The orbits of Pluto and the Earth are derived from osculating elements found in section **E** of the Astronomical Almanac. These are given in six month intervals; we use linear interpolation to obtain elements between the Astronomical Almanac entries. Charon's semimajor axis was determined by speckle interferometry [Beletic et al, 1989], and the rest of its orbital elements from occultation lightcurves. Charon's orbital elements are given in a different reference frame and epoch than the elements for Pluto and the Earth [Tholen and Buie, 1989]. The sensitivity of the eclipse geometry requires a careful treatment of precession and translation from one frame to another [Green, 1985].

We use a three circle approximation to represent Pluto, Charon, and Charon's shadow as seen from the Earth. Charon's shadow is localized by extending the line of sight from the sun to Charon back onto Pluto's disk. Because Pluto is a three dimensional body, the projected outline of Charon's shadow may depart from a circle. This effect scales with the phase angle, however, and is not an important factor, since Pluto's phase angle is never more than 1.9°. The maximum phase angle for the entire data set is 1.8289°, during the 1990 event. The small phase angle means that the defect of illumination is also a negligible effect. At maximum phase, less than 0.03 % of Pluto's surface is in shadow.

Appendix B.
Smoothing the Maps

The smoothing algorithm convolves the maps with a 2-D Gaussian, thereby averaging a pixel with its nearest neighbors. The width of the Gaussian is proportional to the error of the pixel being smoothed, so low error regions are smoothed less than high error ones. The Gaussian is always square in extent with an odd number of pixels on a side. The width of the Gaussian is always a multiple of its width at the lowest-noise pixel in the map. Both the filter extent and the lowest-noise width are parameters set by the user. The spherical harmonic, polynomial and finite element maps presented in Figures 14, 15 and 16 are 40 x 40 pixels. The smoothing filter was 13 x 13 in extent. The Gaussian's width over the lowest-noise portion of the map was 7 pixels (full width at half maximum). The convolution was implemented directly in the space domain. Because a pixel's neighbors do not have equal areas, the filter scaled neighboring pixels by cos(Lat) to weight them by their relative areas.

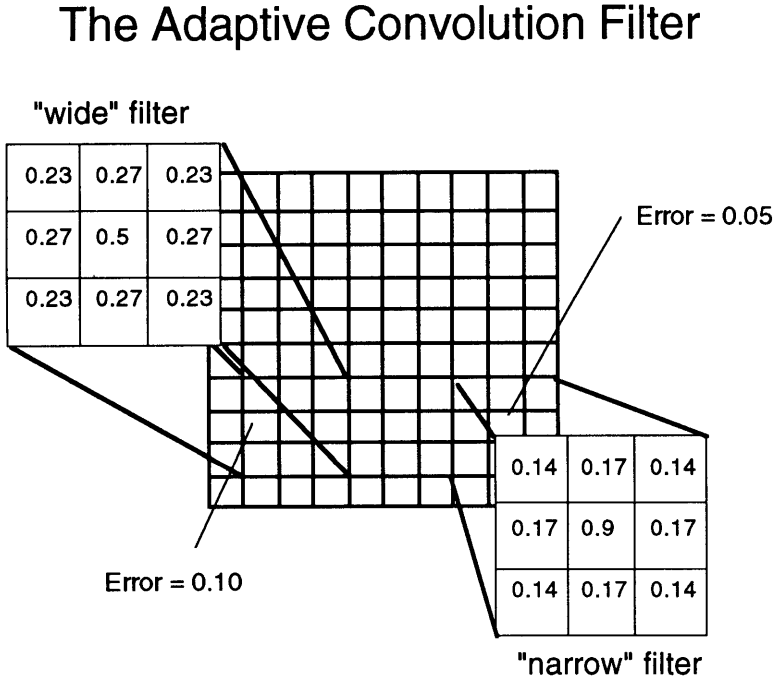

Figure B-1. A 3 x 3 convolution filter applied to two pixels with errors of 0.05 and 0.1. The filter over the noisier pixel is a broader Gaussian than the filter over the cleaner one.

Appendix C.
Integrating Column Abundances

Definition of Symbols

p pressure,

r radius, measured from the center of the planet,

r_p radius of the planet,

ρ density,

g gravitational acceleration at the surface of the planet,

V volume,

R gas constant,

n number of particles,

μ molar mass,

T temperature,

G gravitational constant = 6.67×10^{-8} in cgs units,

M mass of the planet,

A column area,

and [m] = column mass.

What is the amount of atmosphere in a square centimeter column above the surface of a planet? Hydrostatic equilibrium (C-1) and the ideal gas law (C-2) determine the functional form of the density v. height relation

$$\frac{dp}{dr} = -\rho g \qquad \text{(C-1)}$$

$pV = nRT$, or

$$p = \rho \frac{RT}{\mu} \qquad \text{(C-2)}$$

We eliminate the pressure from this system of equations.

$dp = d\rho \frac{RT}{\mu}$, so

$$\frac{dp}{dr} = -\rho g = \frac{d\rho}{dr} \frac{RT}{\mu} \qquad \text{(C-3)}$$

Next collect the densities to one side of the equation

$$\frac{d\rho}{\rho} = \frac{-\mu g}{RT}\,dr \tag{C-4}$$

and take the indefinite integral of both sides of the equation. We'll figure out the constant of integration in a moment. Remember to substitute for $g = GM/r^2$.

Integrating the left side gives us

$$\int \frac{d\rho}{\rho} = \ln(\rho) + C \tag{C-5}$$

and the right side is

$$\int \frac{-\mu g}{RT}\,dr = \frac{-\mu GM}{RT}\int \frac{dr}{r^2} = \frac{-\mu GM}{RT}\left(\frac{-1}{r}\right). \tag{C-6}$$

So we now have

$$\ln(\rho) + C = \frac{\mu GM}{RT}\left(\frac{1}{r}\right) \tag{C-7}$$

or equivalently

$$\rho = \exp\left(\frac{\mu GM}{RT}\left(\frac{1}{r}\right) - C\right) \tag{C-8}$$

The constant of integration are set by the condition that ρ_0 is the surface density when $r = r_p$, the surface radius of the planet.

$$\rho_0 = \exp\left(\frac{\mu GM}{RT}\left(\frac{1}{r_p}\right) - C\right) \tag{C-9}$$

Solving for C yields

$$C = \ln(\rho_0) - \frac{\mu GM}{RT}\left(\frac{1}{r_p}\right) \tag{C-10}$$

So the density equation for a planetary atmosphere in hydrostatic equilibrium is

$$\ln(\rho) - \ln(\rho_0) = \frac{\mu GM}{RT}\left(\frac{1}{r} - \frac{1}{r_p}\right), \text{ or}$$

$$\rho = \rho_0 \exp\left(\frac{\mu GM}{RT}\left(\frac{1}{r} - \frac{1}{r_p}\right)\right). \tag{C-11}$$

Now we can proceed to find the total mass in a column above the surface of a planet. We want to add up the masses of small volume elements in the column from the surface up to infinity. A mass element is

$$dm = \rho dv = \rho A dr, \tag{C-12}$$

The area, A, changes as a function of height.

$$A = A_0\left(\frac{r}{r_p}\right)^2 \tag{C-13}$$

On large planets with relatively thin atmospheres the column width will be nearly constant. On Pluto, where the scale height is about 1/20 of the radius, this amounts to a 10% correction. The total mass in a column will be

$$[m] = \int_{r=r_p}^{r=\infty} dm = \int_{r=r_p}^{r=\infty} \rho\, A_0\left(\frac{r}{r_p}\right)^2 dr \tag{C-14}$$

We substitute for r

$$[m] = \int_{r=r_p}^{r=\infty} \rho_0 \exp\left(\frac{\mu GM}{RT}\left(\frac{1}{r} - \frac{1}{r_p}\right)\right) A_0\left(\frac{r}{r_p}\right)^2 dr = \frac{\rho_0 A_0}{(r_p)^2} \int_{r=r_p}^{r=\infty} \exp\left(\frac{\mu GM}{RT}\left(\frac{1}{r} - \frac{1}{r_p}\right)\right) r^2 dr. \tag{C-15}$$

We solve the integral $e^{(a/x)}x^2dx$ numerically. The column mass per unit area is

$$[m] = \frac{\rho_0}{(r_p)^2} \int_{r=r_p}^{r=\infty} \exp\left(\frac{\mu GM}{RT}\left(\frac{1}{r} - \frac{1}{r_p}\right)\right) r^2 dr \tag{C-16}$$

The bounds on Eq. (C-16) are a little tricky. The factor of r^2 in the integrand makes this integral diverge. This does not mean that there is infinite mass in the atmosphere, just that the upper atmosphere is not in hydrostatic equilibrium. The upper atmosphere is bounded by an exobase or is undergoing hydrostatic blowoff. The exobase is a reasonable upper limit for the integral in (C-16), but Pluto does not have a classical

exobase, at least not in the isothermal approximation. McNutt [1989] points out

> The exobase is defined as the altitude at which the local mean free path equals the local scale height. The residual atmosphere can be thought of as "evaporating" from this level. However, if we assume an isothermal atmosphere [Elliot et al., 1989], we obtain an extrapolated atmosphere for which an exobase does not occur.

We obtain a similar result substituting N_2 for methane. McNutt concludes that atmospheric blowoff does not occur because the thermal structure of the atmosphere yields escape rates reduced by a factor of ~5.

The conclusion we draw from McNutt's argument is that the upper atmosphere has a limit and it does not contribute significantly to the total weight of a column. This hypothesis is borne out if one integrates Eq. (C-16) using 2, 3, or 4 Pluto radii as upper limits on the atmosphere. With these upper limits we found that the column abundances determined by Eq. (C-16) were identical to one part in ten thousand. Furthermore we found that the ratio between the integrated column abundance and the surface pressure was 60.1, slightly less than Pluto's surface gravity of 64.2 cm/sec^2. We therefore derive column abundances from surface pressures using Eq. (38), by dividing P_s by 60.1 cm/sec^2, not 64.2 cm/sec^2.

Appendix D.
Modeling the Reflectance of Thin Frost Layers

This appendix derives an expression for the reflectance of frost on a planetary surface. The model can accommodate frost-deposit mixtures. The model treats the surface as a stack of thin layers, each layer having a transmittance, T, and a reflectance, R. Each layer has a thickness of one particle diameter. Some of the particles may be clear, frost particles, and some may be dark deposits. Each mixture can be represented by a unique choice of R and T.

What happens if we have a large number of layers stacked on top of each other? The overall reflectance from the top layer will be the sum of many reflections from in between layers, especially if the absorption is low and the transmittance is high. One approach is to look at the relative intensities that exist in neighboring layers in the steady state.

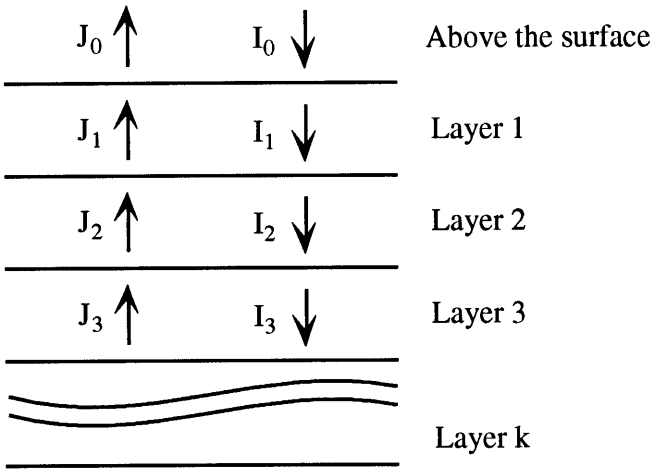

Figure D-1. Modeling the steady state intensity distribution in a stack of thin frost layers.

The incident intensity is I_0. The I's are the downward traveling intensities, and the J's are upward traveling intensities. Our goal is to figure out the ratio between J_0 and I_0.

The equations relating the intensities in adjacent layers are

$$I_{n+1} = T\,I_n + R\,J_{n+1}, \text{ and} \qquad \text{(D-1)}$$

$$J_n = R\,I_n + T\,J_{n+1}.$$

Here we have two equations and four unknowns. We know two of the unknowns,

since I_n will eventually be replaced by I_0, and J_{n+1} will eventually be assumed to be zero. The next step is to isolate I_n and J_n as functions of I_{n+1} and J_{n+1}, so we can cascade layers on top of each other.

$$I_n = (1/T)\, I_{n+1} + (-R/T)\, J_{n+1}, \text{ and} \qquad \text{(D-2)}$$

$$J_n = (R/T)\, I_{n+1} + (T - R^2/T)\, J_{n+1}.$$

If we consider several layers on top of each other, we get the matrix equation

$$\begin{bmatrix} I_n \\ J_n \end{bmatrix} = \begin{bmatrix} 1/T & -R/T \\ R/T & T - R^2/T \end{bmatrix}^k \begin{bmatrix} I_{n+k} \\ J_{n+k} \end{bmatrix} \qquad \text{(D-3)}$$

We raise the matrix to the k^{th} power by using the eigensystem decomposition

$$\mathbf{A}^k = \mathbf{S}\lambda^k\mathbf{S}^{-1} \qquad \text{(D-4)}$$

where λ is the matrix whose diagonal elements are the eigenvalues of the matrix **A**, and **S** is the matrix whose columns are the eigenvectors of **A**. To see how this decomposition works, just remember the definition of an eigenvalue and an eigenvector:

$\mathbf{A}\cdot\mathbf{u} = \lambda_1\mathbf{u}$ **u** is one eigenvector,

$\mathbf{A}\cdot\mathbf{v} = \lambda_2\mathbf{v}$ and **v** is the other. (D-5)

These two equations are equivalent to the matrix equation

$$\begin{bmatrix} A_{11} & A_{12} \\ A_{21} & A_{22} \end{bmatrix} \begin{bmatrix} u_1 & v_1 \\ u_2 & v_2 \end{bmatrix} = \begin{bmatrix} u_1 & v_1 \\ u_2 & v_2 \end{bmatrix} \begin{bmatrix} \lambda_1 & 0 \\ 0 & \lambda_2 \end{bmatrix} \qquad \text{(D-6)}$$

where $\mathbf{S} = \begin{bmatrix} u_1 & v_1 \\ u_2 & v_2 \end{bmatrix}$

If we post-multiply each side by $\mathbf{S}^{-1}$, then we get the $\mathbf{S}\lambda^k\mathbf{S}^{-1}$ decomposition. Getting back to the problem of reflectances, we seek an expression for J_0 / I_0. If we let

$$\mathbf{A}^k = \begin{bmatrix} a & b \\ c & d \end{bmatrix}, \qquad \text{(D-7)}$$

then we obtain the system of equations

$$I_0 = a\, I_k + b\, J_k, \text{ and} \qquad \text{(D-8)}$$
$$J_0 = c\, I_k + d\, J_k.$$

Rewrite this system so that the unknowns, J_0 and I_k, are explicit functions of the knowns, I_0 and J_k.

$$I_k = (1/a)\, I_0 + (-b/a)\, J_k, \text{ and} \qquad \text{(D-9)}$$
$$J_0 = (c/a)\, I_0 + (d - cb/a)\, J_k.$$

The ratio between J_0 and I_0 is c/a (because J_k is presumed to approach zero as $k \to \infty$). We translate c/a into eigenvectors and eigenvalues from the decomposition

$$\mathbf{S}\lambda^{\mathbf{k}}\mathbf{S}^{-1} = \begin{bmatrix} a & b \\ c & d \end{bmatrix}. \qquad \text{(D-10)}$$

Substituting for the elements a and c, we get

$$J_0/I_0 = c/a = [u_2 v_2 (\lambda_1^{\,k} - \lambda_2^{\,k})] \,/\, (u_1 v_2 \lambda_1^{\,k} - u_2 v_1 \lambda_2^{\,k}). \qquad \text{(D-11)}$$

One of the eigenvalues will be greater than one, the other will be less than one. We can assume without loss of generality that λ_1 is the larger eigenvalue. If k is large, the $\lambda_2^{\,k}$ term will become negligible, and we get

$$J_0/I_0 = (u_2 v_2 \lambda_1^{\,k})/(u_1 v_2 \lambda_1^{\,k}) = u_2/u_1. \qquad \text{(D-12)}$$

We used *Mathematica*™ to determine the eigenvalues and eigenvectors of **A**. These have been simplified to yield the eigenvalues:

$$\lambda_1 = \frac{1 - R^2 + T^2 + \sqrt{R^4 + T^4 - 2(R^2 + T^2 + R^2T^2) + 1}}{2T}$$
$$\lambda_2 = \frac{1 - R^2 + T^2 - \sqrt{R^4 + T^4 - 2(R^2 + T^2 + R^2T^2) + 1}}{2T} \qquad \text{(D-13)}$$

and the eigenvectors:

$$u_1 = \frac{1 + R^2 - T^2 - \sqrt{R^4 + T^4 - 2(R^2 + T^2 + R^2T^2) + 1}}{2R}$$

$$u_2 = 1$$

$$v_1 = \frac{1 + R^2 - T^2 + \sqrt{R^4 + T^4 - 2(R^2 + T^2 + R^2T^2) + 1}}{2R}$$

$$v_2 = 1. \qquad \text{(D-14)}$$

The surface reflectance is u_2/u_1.

$$\frac{J_0}{I_0} = \frac{u_2}{u_1} = \frac{1 + R^2 - T^2 - \sqrt{R^4 + T^4 - 2(R^2 + T^2 + R^2T^2) + 1}}{2R} \qquad \text{(D-15)}$$

How well does this expression work? Try a test case: let R = 0.05, and let T vary from 0.55 to 0.95.

R	T	J_0/I_0
0.05	0.59	0.076
0.05	0.61	0.079
0.05	0.63	0.083
0.05	0.65	0.086
0.05	0.67	0.091
0.05	0.69	0.095
0.05	0.71	0.101
0.05	0.73	0.107
0.05	0.75	0.115
0.05	0.77	0.123
0.05	0.79	0.134
0.05	0.81	0.147
0.05	0.83	0.163
0.05	0.85	0.184
0.05	0.87	0.212
0.05	0.89	0.252
0.05	0.91	0.315
0.05	0.93	0.430
0.05	0.95	0.999

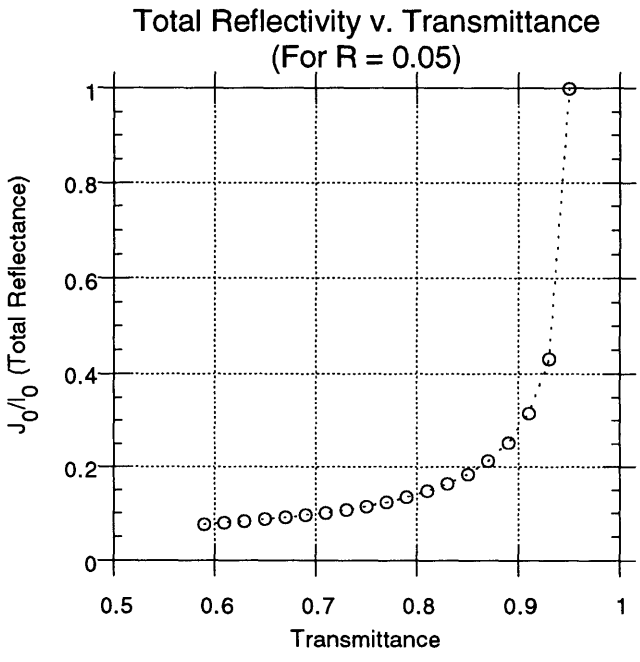

Figure D-2. Albedo as a function of transmittance. Since R is held constant, this plot can also be thought of as showing albedo as a function of absorption.

This graph supports our expectations - the overall reflectance drops sharply when there is any absorption in the system. We have assumed that a large part of the frost's reflectance comes from several layers beneath the top layer. We could have modeled the frost's high reflectance with a single high reflectance off of the top layer, but then we could not successfully model the effects of absorption within the frost.

Now we move on to the problem that motivated this treatment in the first place: what is the reflectance a two-component surface? This is a surface with an upper layer of one kind of frost or residue and an underlying layer of another type of frost. Define R_1, T_1 as the reflectance and transmittance of the top frost layers, and R_2, T_2, as the parameters of the underlying frost surface.

R_1, T_1	Top Layer, k layers thick
R_2, T_2	Underlying surface has infinite extent

Figure D-3. The two-component surface model.

The matrix equation we'll use is still of the form

$$\begin{bmatrix} I_0 \\ J_0 \end{bmatrix} = \mathbf{A} \begin{bmatrix} I_{n+k} \\ J_{n+k} \end{bmatrix}, \tag{D-16}$$

but **A** will be composed of two matrices.

$$\mathbf{A} = \begin{bmatrix} \frac{1}{T_1} & \frac{R_1}{T_1} \\ \frac{R_1}{T_1} & T_1 - \frac{R_1^2}{T_1} \end{bmatrix}^k \begin{bmatrix} \frac{1}{T_2} & \frac{R_2}{T_2} \\ \frac{R_2}{T_2} & T_2 - \frac{R_2^2}{T_2} \end{bmatrix}^\infty \tag{D-17}$$

Let **s** and **t** be the eigenvectors of the first matrix, and **u** and **v** be the eigenvectors for the second. We know that $s_2 = t_2 = u_2 = v_2 = 1$, and Equations (D-14) gives reasonably straightforward expressions for s_1 and t_1 in terms of R_1 and T_1, and u_1 and v_1 in terms of R_2 and T_2.

In the two-component system, some of the light will be reflected from layers in the top component, and some will be transmitted all the way through the top component,

reflect off of layers in the bottom component, and be transmitted back out through the top. Define R_top as the total reflectance of the top component, T_top as fraction of light that passes through the top component, and R_bot as the reflectance of the underlying frost component.

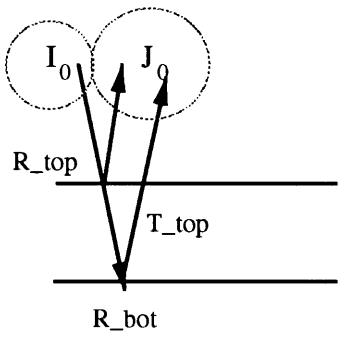

Figure D-4. R_top is the total reflection due to the top component. T_top is the overall transmittance of the top component. R_bot is the overall reflectance of the bottom layer.

How much light passes through the top component? From Equation (D-9) we see that the fraction of I_0 that passes through k layers is (1/a), or in terms of eigenvectors and eigenvalues

$$\frac{I_k}{I_0} = \left(\frac{s_1 - t_1}{s_1\lambda_1^k - t_1\lambda_2^k}\right) = T\_top \tag{D-18}$$

The fraction of I_0 reflected by the top k layers is

$$\frac{J_0}{I_0} = \frac{\lambda_1^k - \lambda_2^k}{s_1\lambda_1^k - t_1\lambda_2^k} = R\_top \tag{D-19}$$

Since the underlying frost layer is infinitely thick, the reflectance is the limit as k->∞.

$$\frac{J_0}{I_0} = \frac{1}{u_1} = R\_bot \tag{D-20}$$

As illustrated in Figure D-4, the total amount of light reflected by the two-component surface will be

$$\text{Albedo} = \frac{J_0}{I_0} = R\_top + (T\_top)^2\, R\_bot = \frac{\lambda_1^k - \lambda_2^k}{s_1\lambda_1^k - t_1\lambda_2^k} + \left(\frac{s_1 - t_1}{s_1\lambda_1^k - t_1\lambda_2^k}\right)^2 \frac{1}{u_1} \tag{D-21}$$

Suppose we deposit a layer of dark material on top of a bright polar cap - how does the overall surface reflectance change as a function of the depth of the top layer?

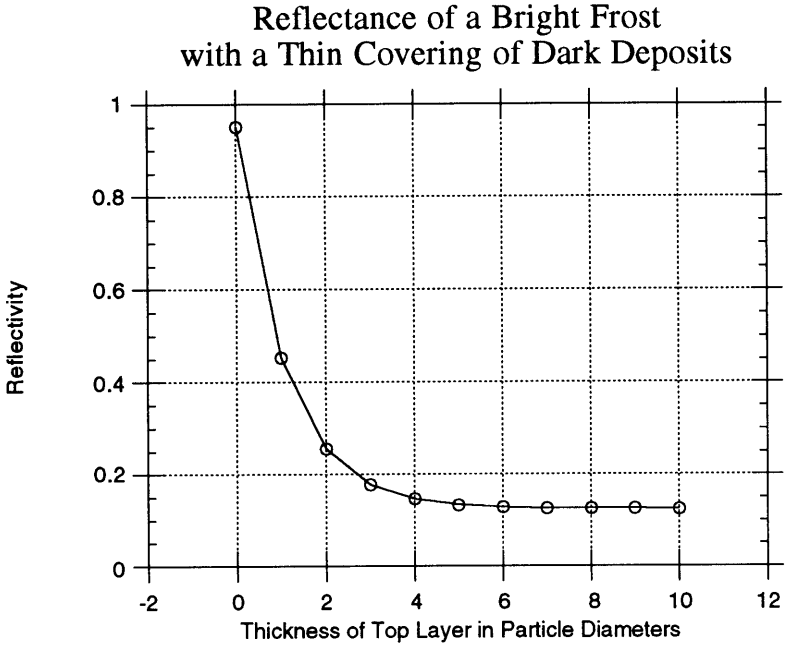

Figure D-5. Modeled reflectance of a two-component surface. R = 0.075 for both surfaces, T = 0.63 for the top component, 0.9249 for the bottom component. The overall reflectance of the surface reaches its asymptotic value of 0.125 with a top component layer that is only four or five particle diameters in thickness.

The overall reflectance drops dramatically with only a thin covering of dark deposits. Keep in mind that only a small fraction of the underlying frost may be dark material, so a great deal of frost may have to sublimate before even a thin covering of dark material accumulates. For example, suppose five gm/cm^2 of 98% volatile material has sublimated from the surface. The residue would be 0.1 gm/cm^2, which corresponds to a thickness of 0.11 cm given a frost density of 0.91 g/cm^3. If a particle diameter is 200 μm, the top covering would only be 5.5 layers thick, even though five gm/cm^2 sublimated from the surface.

Appendix E.
The Relation between Hapke and Minnaert Parameters

While a discussion of Hapke parameters and Minnaert parameters is not new, it seemed worthwhile to include this appendix on the relation between various quantities, if only to serve as a reference for the next time we encounter a photometric problem. We will ignore wavelength dependencies throughout this appendix.

We begin the geometric albedo, since it is usually the first thing one calculates after observing an object's magnitude. The geometric albedo is defined as a ratio:

$$A_p = \frac{\text{Light received from an object}}{\text{Light received from an isotropically scattering disk of the same angular size and at the same distance}} \qquad \text{(E-1)}$$

By definition, a Lambert disk has a geometric albedo of 1. A Lambert *sphere* has a geometric albedo of 2/3, because some of the incident light is scattered from the limb away from the source, whereas the light from a disk is isotropically scattered over a single hemisphere only.

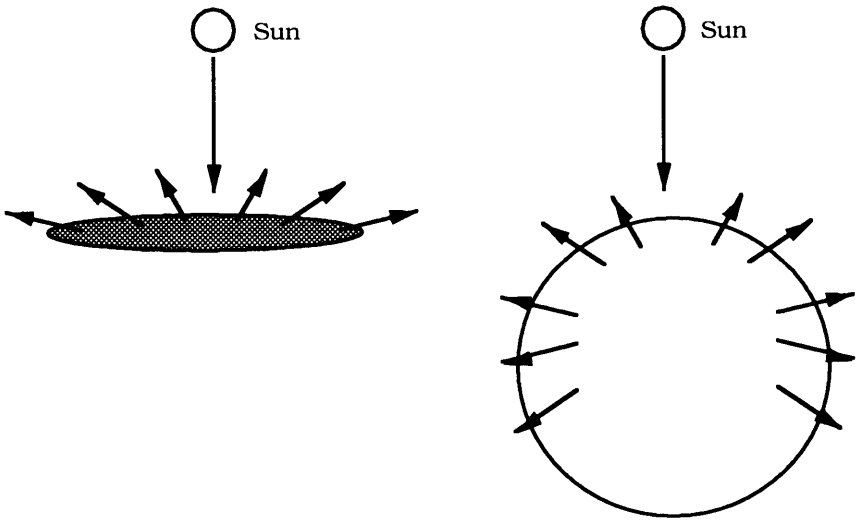

Figure E-1. A Lambert sphere reflects less light than a Lambert disk of the same diameter because some of the light from the sphere escapes past the limb.

The Bond albedo is the ratio of total light received to total light reflected. It is useful in calculating the energy absorbed from the sun or other source.

A_b = Total light received/total light reflected (E-2)

The ratio of the Bond albedo over the geometric albedo is called the *phase integral.* The phase integral, *q*, describes an object's propensity for reflecting light nonisotropically. A surface of tiny corner cubes, for example, would reflect preferentially back toward the direction of illumination. Its geometric albedo would be *greater than one*, since it would appear brighter than an isotropic disk of the same size, and the phase integral would be less than one. Even though A_p may exceed unity (and does for a few bright objects in the solar system), A_b may not. Voyager estimates of Triton's phase integral ranged from q = 1.2 to 1.5, depending on the filter color, so Triton's Bond albedo is *greater* than its geometric albedo.

Now we come to the definitions of bidirectional reflectance, the bihemispherical reflectance, etc. These definitions are taken from Hapke's paper of 1981, "Bidirectional Reflectance Spectroscopy, 1. Theory."

Consider a surface with a normal vector, z, illuminated by the sun (a collimated source) and observed from the Earth.

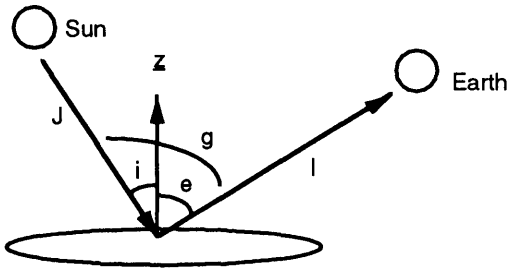

Figure E-2. Definition of angles i, e, and g.

i = angle of incidence, between the incident ray and the surface normal.

e = angle of emergence, between the normal and the ray to the observer.

g = phase angle, the angle between the incident and emergent rays.

Also define $\mu_0 = \cos i$ and $\mu = \cos e$. The collimated beam from the sun has an intensity J, while the cone of light observed on the Earth has a *specific intensity* or *spectral radiance* of I. The specific intensity, I(r, Ω) is defined as the radiant energy at point *r* passing per unit time through a unit area perpendicular to the direction of travel per unit solid angle about the axis on which the radiation is moving.

Next define *w*, the single scattering albedo. This parameter describes the ratio of an average particle's scattering efficiency to its extinction efficiency. The single particle scattering function, *P(g)*, can accomodate the particle's nonisotropic scattering. It is normalized to be unity for isotropic scatterers, but is some function of g that is less than one for forward scattering, greater than one for back scattering. Note that a particle can be predominately forward scattering for some phase angles and backward scattering for others. B(g) is a backscatter function which can be used to implement an opposition effect.

For notational convenience we define $\gamma = \sqrt{1 - w}$. The *bihemispherical reflectance* , r_0, is defined as

$$r_0 = \frac{(1 - \gamma)}{(1 + \gamma)} \tag{E-3}$$

The bihemispherical reflectance is the ratio of the total light scattered in all directions from a surface to the uncollimated light incident on the surface. Hapke points out that r_0 is never measured in practice, but is useful in its relation to other quantities. For example, an expansion for the geometric albedo in the isotropic scattering case is

$$A_p = r_0/2 + r_0^2/6 \tag{E-4}$$

Thus, in the isotropic case (where P(g) = 1 for all g) A_p is a function of w alone.

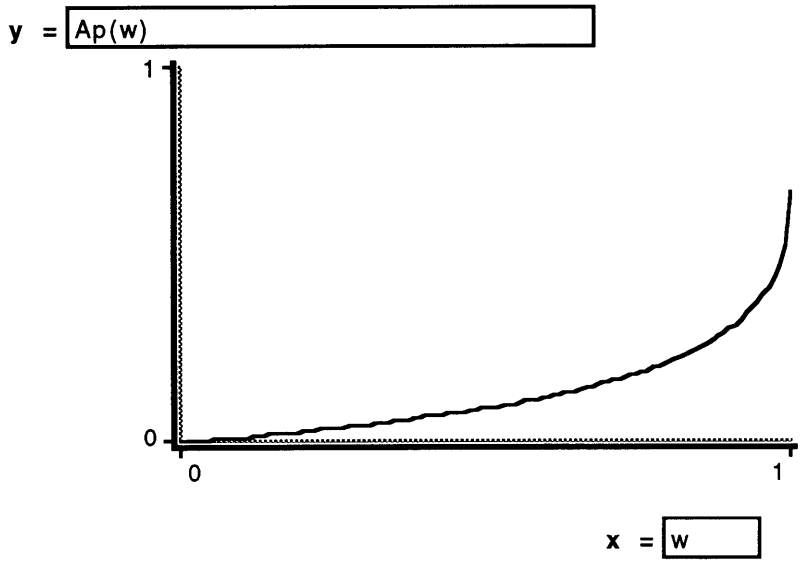

Figure E-3. Geometric albedo as a function of single scattering albedo for an isotropically scattering surface.

Notice that the case of the Lambert sphere, with w = 1, has a geometric albedo of 2/3 as it should. If there is some nonisotropic scattering, the geometric albedo has an additional term,

$$A_p = r_0(1/2 + r_0/6) + (w/8)[(1 + B_0)P(0) - 1] \quad \text{(E-5)}$$

If the opposition magnitude, B_0 is zero and P(0) is nearly one, this third term cancels out. If P(0) is known *a priori*, then this equation (E-5) determines the average single scattering albedo from the geometric albedo.

The bidirection reflectance is equal to I/J, the ratio of the radiant power received per unit area per solid angle viewing the surface at an angle *e* from the normal (and the collimated illumination coming from an angle *i*) to the radiant power per unit area of the source. The bidirectional reflectance is equal to

$$r(\mu_0, \mu, g) = \frac{w}{4}\frac{\mu_0}{\mu_0 + \mu}[(1 + B(g))P(g) + H(\mu_0)H(\mu) - 1]$$

or (E-6)

$$\bar{I}(\mu_0, \mu, g) = J\frac{w}{4}\frac{\mu_0}{\mu_0 + \mu}[(1 + B(g))P(g) + H(\mu_0)H(\mu) - 1]$$

$H(\mu)$ is Hapke's approximation to Chandrasekhar's H-function,

$$H(\mu) = \frac{1 + 2\mu}{1 + 2\mu\gamma} \quad \text{(E-7)}$$

We consider the special case where g = 0 (and therefore $\mu_0 = \mu$) and the scattering is isotropic, so B(g) = 0 amd P(g) = 1. In this case the relation between $r(\mu, w = 0.9)$ and μ is nearly linear.

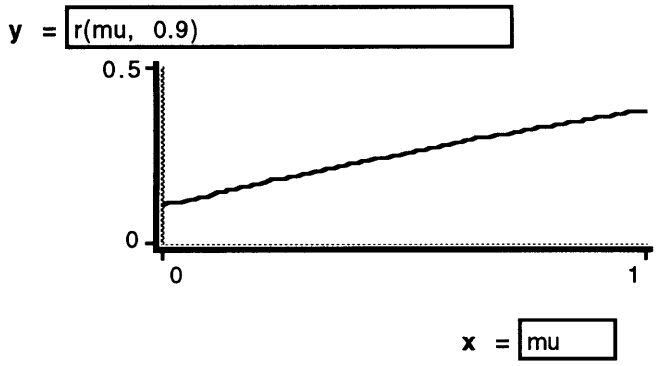

Figure E-4. Limb darkening automatically described by the bidirectional reflectance.

The bidirectional reflectance automatically generates a limb-darkened intensity profile, depending on the orientation of the viewer and the source. When the phase angle is zero, the phase function P(0) can rasie or lower the bidirectional reflectance over the entire hemisphere.

An altenative way of describing the brightness of a planet's surface is by the *Minnaert function* , an empirical function of the form

$$\bar{I} = \bar{I}_0 \, \mu_0^{k} \, \mu^{k-1} \tag{E-8}$$

Where $\bar{I}$ is the relative brightness of the surface and $\bar{I}_0$ and k are empirical parameters. If the phase angle is zero (E-8) reduces to

$$\bar{I} = \bar{I}_0 \, \mu^{2k-1} \tag{E-9}$$

Thus we see that a value for the k-parameter of 0.5 is equivalent to a non-limb darkened disk. If we assume $\bar{I}_0 = 1$ and k = 0.7, we get the following intensity profile.

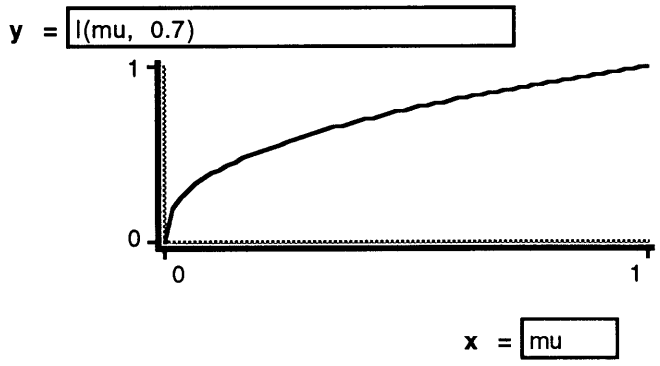

Figure E-5. Intensity profile of a Minnaert disk with k = 0.7. This profile is a contrast to Fig. E-4 near the limb, but similar in slope near the center of the disk.

Notice that the slope of the intensity profile is similar to the bidirectional reflectance case except near the limb (where $\mu = 0$). Thus there is hope that two parameters, $\bar{I}_0$ and k, can be chosen to match a particular set of Hapke parameters, w and P(0). We will need two equations to determine the two unknown Minnaert parameters.

The first equation can be obtained by relating both sets of parameters to the geometric albedo. Equation (E-5) gives A_p in terms of the Hapke parameters. In the Minnaert case we define the *normal reflectance* as having this relationship to the geometric albedo:

$$r_n = (0.5 + k)\, A_p \qquad \text{(E-10)}$$

The normal reflectance is presumably defined for an observer aligned with the source (zero phase angle), and defined as the ratio of the radiant power per unit area of the reflected light along the line of sight to the observer over the radiant power per unit area of the collimated source. If we let the normal reflectance equal the area-weighted average of $\bar{I}$ in Eq. (E-9), we get

$$r_n = 2\bar{I}_0/(2k + 1)$$

or $\qquad \text{(E-11)}$

$$(0.5 + k)\, A_p = 2\bar{I}_0/(2k + 1)$$

The factors of (2k + 1) cancel out, leaving the relation $A_p = 4\,\bar{I}_0$. Thus $\bar{I}_0$ is uniquely determined by any pair of w and P(0).

$$A_p = 4\bar{I}_0 = r_0(1/2 + r_0/6) + (w/8)[(1 + B_0)P(0) - 1] \qquad \text{(E-12)}$$

Now we need to find the value of k that best matches the intensity profile of the Hapke model. Since this match is only approximate, we must choose the match critierion - over what part of the disk do we want the best match? The extreme limb region is poorly described by the Minnaert model, so we'll try to match the intensity profiles near the center of the disk. The slope of the bidirectional reflectance with respect to μ is a function of w and P(0). To get a rough match of limb profiles for the Hapke and the Minnaert models, we decided to set the linear slopes of the bidirectional reflectance and the Minnaert intensity equal to each other. We decided to approximate the slopes over the interval from $\mu = 0.5$ to $\mu = 1.0$, the center of the disk.

We evaluate Eq. (E-9) at zero phase angle and at $\mu = 1$ and $\mu = 0.5$.

$$I(\mu = 1) = I_0,$$

and (E-13)

$$I(\mu = 0.5) = I_0/2^{2k-1}$$

An approximation for the slope of the intensity with respect to μ is thus

$$\Delta I/\Delta\mu \approx I_0(2 - (/2)^{2k-2}) \quad \text{(E-14)}$$

Similarly we evaluate the bidirectional reflectance at zero phase angle (and assume no opposition effect) at $\mu = 1$ and $\mu = 0.5$

$$r(\mu = 1) = (w/8)\,(P(0) - 1 + 3/(1 + 2\gamma)$$

and (E-15)

$$r(\mu = 0.5) = (w/8)\,(P(0) - 1 + 2/(1 + \gamma)$$

So an approximation for $\Delta r/\Delta\mu$ is

$$\Delta r/\Delta\mu \approx (w/16)\,((1 - \gamma)/(1 + 3\gamma + 2\gamma^2)) \quad \text{(E-16)}$$

Setting the two slopes equal to each other lets us solve for k in terms of w and P(0). Remember that to solve for k we will have to use Eq. (E-12) to substitute for I_0.

$$\frac{\Delta I}{\Delta\mu} \approx \frac{\Delta r}{\Delta\mu} \approx I_0\left(2 - \left(\frac{1}{2}\right)^{2k-2}\right) \approx \frac{w}{16}\left[\frac{1 - \gamma}{1 + 3\gamma + 2\gamma^2}\right] \quad \text{(E-17)}$$

or

$$k = \frac{\log_2\left[\frac{16I_0}{w}\left(\frac{1 + 3\gamma + 2\gamma^2}{1 - \gamma}\right)\right]}{2} + 1$$

One final question: how do the normal reflectance and bidirectional reflectance compare? If we describe the same object in terms of bidirectional reflectances and normal reflectances, the two reflectances will have different scales. The bidirectional reflectance differs from the normal reflectance at the center of the disk by a factor of $(1/\pi)$. Near the edge of the disk the definition of the bidirectional reflectance automatically incorporates limb darkening, while the normal reflectance description of a planet may or may not

include a Minnaert limb parameter. The bidirectional reflectance is "too small" by a factor of π because it is defined as an irradiance per solid angle.

References

Andersson, L.E. 1978. Eclipse Phenomena of Pluto and its Satellite. *Bull. Amer. Astron. Soc.* **10**, 586.

Aumann, H.H., and Walker, R.G. 1987. *IRAS* Observations of the Pluto-Charon System. *Astron. J.* **94** (4), 1088-1091.

Battin, R.H. 1987. An Introduction to the Mathematics and Methods of Astrodynamics. American Institute of Aeronautics and Astronautics, Inc., 1633 Broadway, New York, NY 10019

Beatty, J.K. and Chaikin, A. 1990. The New Solar System. Cambridge Unverstiy Press, Cambridge, England.

Beletic, J.W., Goody, R.M., and Tholen, D.J. 1989. Orbital Elements of Charon from Speckle Interferometry. *Icarus* **79**, 38-46.

Binzel, R.P. 1988. Hemispherical Color Differences on Pluto and Charon. *Science* **241**, 1070-1072.

Binzel, R.P. and Mulholland, J.D., 1984. Photometry of Pluto During the 1983 Opposition: A New Determination of the Phase Coefficient. *Astron. J.* **89**, 1759-1761.

Binzel, R.P., Tholen, D.J., Tedesco, E.F., Buratti, B.J., and Nelson, R.M., 1985. The Detection of Eclipses in the Pluto-Charon System. *Science* **228**, 1193-1195.

Bosh, A.S., Young, L.A., Elliot, J.L., Hammel, H.B., and Baron, R.L., 1992. Photometric Variability of Charon at 2.2 μm. *Icarus* **95**, 319-324.

Brown, G,N. and Zeigler, W.T., 1980. Vapor Pressure and Heats of Vaporization and Sublimation of Liquids and Solids of Interest in Cryogenics below 1-Atm Pressure, in *Advances in Cryogenic Engineering* **25** (New York, Plenum Press).

Buie, M.W. and Tholen, D.J. 1988. The Surface Albedo Distribution of Pluto. *Icarus* **79** 23-37.

Buie, M.W., Tholen, D.J. and Horne, K., 1992. The Surface Albedo Distribution of Pluto. *Icarus* **97**, 211-227.

Buie, M.W., Lebofsky, L.A., Tedesco, E.F. and Cruikshank, D.P. 1989. Methane Map of Pluto from Mutual Event Observations. *Bull. Amer. Astron. Soc.* **21**, No. 3, 985.

Burwitz, V., Reinsch, K., Pakull, M.W., and Bouchet, P., 1991. New Aspects of the Binary Planet Pluto-Charon. *ESO Messenger* **Dec. 1991** 23-26.

Chamberlain, J.W., and Hunten, D.M. 1987. Theory of Planetary Atmospheres, 2nd Ed. Academic Press, San Diego.

Christie, J.W., and Harrington, R.S. 1978. The Satellite of Pluto. *Astron. J.* **83** 1005.

Clarke, R.N., Fanale, F.P., and Gaffey, M.J., 1986. Surface Composition of Natural Satellites. Chapter 10 in *Satellites*, Burns, J. and Matthews, M.S., Editors. The University of Arizona Press, Tuscon.

Cruikshank, D.P., Broen, R.H., and Clark, R.N., 1989. Triton: Do We See the Surface? *Science* **245**, 283-286.

Cruikshank, D.P., 1992. *Personal Communication* .

Dobrovolskis, A.R., and Harris, A.W. 1983. The Obliquity of Pluto. *Icarus* **55**, 231-235.

Drish, W.F., Wild, W.J., and Marcialis, R.L. 1991. Images of Pluto Generated by Matrix Lightcurve Inversion. *In Press*.

Dunbar, R.S. and Tedesco, E.F. 1986. Modeling Pluto-Charon Mutual Events. I. First Order Models. Submitted to the Astron J.

Elliot, J.L., Dunham, E.W., Bosh, A.S., Slivan, S.M., Young, L.A., Wasserman, L.H., and Millis, R.L. 1989. Pluto's Atmosphere. *Icarus* **77**, 148-170.

Elliot, J.L. and Young, L.A., 1991. Limits on the Radius and a Possible Atmosphere of Charon from Its 1980 Stellar Occultation. *Icarus.* **89**, 244-254.

Elliot, J.L. and Young, L.A., 1992. Analysis of Stellar Occultation Data for Planetary Atmospheres. I. Model Fitting with Application to Pluto. *Astron. J.* **103**, No. 3, 990-1015.

Eluszkiewicz, J., 1991. On the Microphysical State of the Surface of Triton. *J. Geophys. Res.*. **96** (Supplement), 19217-19229.

Green, R.M. 1985. Spherical Astronomy. Cambridge Unversity Press, Cambridge, England.

Hapke, B. W., and Wells, E. 1981. Bidirectional reflectance spectroscopy. 2. Experiments and observations. *J. Geophys. Res.* **86**, 3055-3060.

Holton, J.R. 1979. An Introduction to Dynamic Meteorology, 2nd Ed. Academic Press, San Diego.

Horne, K., Buie, M.W. and Tholen, D.J. 1988. Maximum Entropy Maps of Pluto and Charon from Mutual Event Light Curves. *Bull. Amer. Astron. Soc.* **20**, 1089.

Hoyt, W.G. 1980. Planets X and Pluto. The University of Arizona Press, Tuscon, AZ.

Ingersoll, A.P., 1990. Dynamics of Triton's Atmosphere. *Nature* **344**, 315-317.

Ingersoll, A.P., Summers, M.E., and Schlipf, S.G. 1985. Supersonic Meteorology of Io: Sublimation-Driven Flow of SO_2. *Icarus* **64**, 375-390.

Leighton, R.B. and Murray, B.C., 1966. Behavior of Carbon Dioxide and Other Volatiles on Mars. *Science* **153**, 136-144.

Lunine, J., 1992. COSPAR paper on nitrogen surfaces (complete reference to be added).

Marcialis, R.L. 1983. Master's thesis, Vanderbilt University, Nashville, Tennessee.

Marcialis, R.L. 1988. A Two-Spot Model for the Surface of Pluto. *Astron. J.* **95**, 941-947.

McNutt, R.L. 1989. Models of Pluto's Upper Atmosphere. *Geophys. Res. Lett.* **16**, no. 11, 1225-1228.

Moore, J.M, and Spencer, J.R., 1990. Koyaanismuuyaw: The Hypothesis of a Perenially Dichotomous Triton. *G.R.L.* **17**, No. 10, 1757-1760.

Moore, W.J., 1962. Physical Chemistry. Prentice-Hall, Englewood Cliffs, N.J.

National Research Council. 1929. *International Critical Tables of Numerical Data, Physics, Chemistry, and Technology* **Vol. 63**, pages 82-87.

Owen, T., Geballe, T, de Bergh, C., Young, L.A., Elliot, J.L., and Cruikshank, D., 1992. IAU Circular No. 5532, May 30, reporting the detection of N_2 and CO on Pluto with the CGS4 spectrometer on UKIRT at Mauna Kea.

Press, W.H., Flannery, B.P., Teukolsky, S.A. and Vetterling, W.T. 1988. Numerical Recipes in C. Press Syndicate of the University of Cambridge.

Sawyer, S.R., Reflectance Spectroscopy of the Surface and Atmosphere of Pluto-Charon.

Bull. Amer. Astron. Soc. **21**, 986.

Scott, T.A., 1976. Solid and Liquid Nitrogen. *Physics Reports (Section C of Physics Letters).* **27**, No. 3, 89-157.

Skilling, J. and Bryan, R.K., Maximum Entropy Image Reconstruction: General Algorithm. *Mon. Not. R. Astr. Soc.* **211**, 111-124.

Smith, B.A., Soderblom, L.A., Banfield, D., Barnet, C., Basilevsky, A.T., Beebe, R.F., Bollinger, K., Boyce, J.M., Brahic, A., Briggs, G.A., Brown, R.H., Chyba, C., Collins, S.A., Colvin, T., Cook II, A.F., Crisp, D., Croft, S.K., Cruikshank, D., Cuzzi, J.N., Danielson, G.E., Davies, M.E., De Jong, E., Dones, L., Godfrey, D., Goguen, J., Grenier, I., Haemmerle, V.R., Hammel, H., Hansen, C.J., Helfenstein, C.P., Howell, C., Hunt, G.E., Ingersoll, A.P., Johnson, T.V., Kargel, J., Kirk, R., Kuehn, D.I., Limaye, S., Masursky, H., McEwen, A., Morrison, D., Owen, T., Owen, W., Pollack, J.B., Porco, C.C., Rages, K., Rogers, P., Rudy, D., Sagan, C., Schwartz, J., Shoemaker, E.M., Showalter, M., Sicardy, B., Simonelli, D., Spencer, J., Sromovsky, L.A., Stoker, C., Strom, R.G., Suomi, V.E., Synott, S.P., Terrile, R.J., Thomas, P., Thompson, W.R., Verbiscer, A., Veverka, J. 1989. Voyager 2 at Neptune: Imaging Science Results. *Science* **246**, 1422-1449.

Spencer, J.R., 1990. Nitrogen Frost Migration on Triton: A Historical Model. *Geophys. Res. Lett.* Neptune Special Issue.

Spencer, J.R. and Moore, J.M., 1990. The Influence of Thermal Inertia on Temperatures and Frost Stability on Triton. *Geophys. Res. Lett.* Neptune Special Issue.

Stansberry, J.A. 1989. Albedo Patterns on Triton. *Geophys. Res. Lett.* **16** (8), 961-964.

Stansberry, J.A., Lunine, J.I., and Porco, C.C. 1990. Zonally Averaged Thermal Balance and Stability Models for Nitrogen Polar Caps on Triton. *Geophys. Res. Lett.* **17** (10), 1773-1776.

Stern, S..A. 1989. Implications of the Stability and Radiative Time Constant of Triton's Atmosphere. *Geophys. Res. Lett.* **16** (8), 977-980.

Stern, S.A. and Trafton, L.M., 1984. Constraints on Bulk Composition, Seasonal Variation, and Global Dynamics of Pluto's Atmosphere. *Icarus* **57**, 231-240.

Stern, S.A., Trafton, L.M. and Gladstone, G.R. 1988. Why is Pluto Bright? Implications of the Albedo and Lightcurve Behavior of Pluto. *Icarus* **75**, 485-498.

Sykes, M.V., Cutri, R.M., Lebofsky, L.A. and Binzel, R.P. 1987. IRAS Serendipitous Survey Observations of Pluto and Charon. *Science* **237**, 1336-1340.

Tholen, D.J. and Buie, M.W., 1989. Circumstances for Pluto-Charon Mutual Events in 1990. *Astron. J.*

Tholen, D.J. and Buie, M.W., 1991. How Big is Pluto? *Bull. Amer. Astron. Soc.* **23**, 1216.

Trafton, L. and Stern, S.A., 1983. On the Global Distribution of Pluto's Atmosphere. *Ap. J.* **267**, 872-881.

Trafton, L., 1984. Large Seasonal Variations in Triton's Atmosphere. *Icarus* **58**, 312-324.

Veverka, J., Thomas, P., Johnson, T.V., and Matson, D., 1986. The Physical Characteristics of Satellite Surfaces. Chapter 8 in *Satellites*, Burns, J. and Matthews, M.S., Editors. The University of Arizona Press, Tuscon.

Wild, W.J. 1989. Matrix Formalism for Inferring Planetary Surface Albedo Distributions

from Light-Curve Measurements. *Pub. Astron. Soc. Pac.* **101**, 844-848.

Walker, M.F., and Hardie, R. 1955. A Photometric Determination of the Rotational Period of Pluto. *Pub. Astron. Soc. Pac.* **67**, 224-231.

Young, E.F. 1990. A Surface Albedo Map of Pluto Based on Photometry of Mutual Events. Master's Thesis, Massachusetts Institute of Technology, Cambridge, Massachusetts.

Young, E.F. and Binzel, R.P. 1991. Mapping Pluto's Surface from Mutual Event Lightcurves: A Comparison of Techniques and Physical Implications. *Bull. Amer. Astron. Soc.* **23**, 1216.

Zombeck, M.V.. 1990. Handbook of Space Astronomy and Astrophysics, 2nd Edition. Cambridge University Press.